Susana Ferreira de Oliveira Silva

FIBRE BRAGG GRATING BASED STRUCTURES FOR OPTICAL SENSING AND FILTERING

Departamento de Física

Faculdade de Ciências da Universidade do Porto

Junho de 2007

TA1815 SILs F 2007

TA1815 SILs F 2007

Susana Ferreira de Oliveira Silva

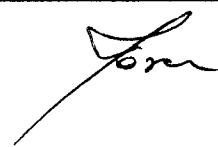# FIBRE BRAGG GRATING BASED STRUCTURES FOR OPTICAL SENSING AND FILTERING

Dissertação submetida à Faculdade de Ciências da Universidade do Porto
para obtenção do grau de Mestre em Optoelectrónica e Lasers

Departamento de Física

Faculdade de Ciências da Universidade do Porto

Junho de 2007
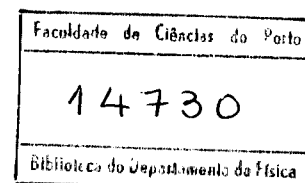
Dissertação realizada sob a supervisão de

Doutor José Luís Santos

Professor Associado do Departamento de Física

da Faculdade de Ciências da Universidade do Porto

"Nothing in life is to be feared, it is only to be understood."

Marie Curie
(1867-1934)

Acknowledgments

The work presented in this dissertation was developed in the Optoelectronics and Electronic Systems Unit of INESC Porto, coordinated by Professor José Luís Santos, to whom I would like to express my gratitude for opening to me the doors of this Unit, for the permanent trust in me and, most especially, for his friendship.

The acknowledgments also go to all my work colleges of the Optoelectronics Unit that in some way helped me during my work, in particular to Orlando Frazão and Paulo Caldas, for the interest demonstrated in the work developed and the helpful advices.

A special word goes to my dearest friend Luísa to whom words will never by enough to thank her for the patience with me and words of wisdom, and most especially for her friendship.

To my dearest friend Catarina, I which to thank for the constant sharing of experiences in the lab and also in life. Most of all, for her deepest friendship.

To my husband Paulo, for the patience with me, for all the comforting words in the toughest hours, for all the loving and support.

To my parents, for always supporting me in my decisions and my education. Most of all, for their loving and friendship.

Finally, I which to thank Francisco Araújo and Luís Alberto for giving me the opportunity to integrate de International ESA-One Project.

Sumário

Esta dissertação apresenta o estudo e desenvolvimento de dispositivos baseados em redes de Bragg em fibra óptica e sua aplicação na área dos sensores e dos filtros ópticos. Inicia com uma revisão sobre a tecnologia das redes de Bragg em fibra óptica, onde é focado particular interesse nas redes de Bragg com desvio de fase. O resultado de algumas simulações e as principais características espectrais destes dispositivos fabricados *in-house* são analisados.

A tecnologia de interferómetros Fabry-Perot baseados em redes de Bragg em fibra óptica como elementos sensores dinâmicos de deformação é apresentada. Duas configurações sensoras de deformação baseadas numa técnica de modulação de fase são propostas e o respectivo sistema de desmodulação é descrito. Também é proposto um sistema de interrogação para interferómetros de Fabry-Perot em fibra óptica baseado na modulação dinâmica de uma rede de Bragg com um desvio de fase de π por meio de um disco piezoeléctrico. Por fim, os aspectos teóricos e resultados experimentais são analisados.

Um tipo específico de sensores ópticos é apresentado: os *tapers* em fibra óptica. São descritas algumas configurações baseadas na combinação de redes de Bragg com *tapers* assim como o método de fabricação e as suas características espectrais. A sua sensibilidade à deformação e temperatura é também estudada. Os aspectos teóricos e resultados experimentais sobre a sensibilidade da fibra óptica à deformação quando submetida à acção mecânica de *tapers* é também analisada.

Os aspectos gerais de filtros ópticos aplicados a sistemas LIDAR são apresentados. Em particular, são descritas as características de alguns filtros ópticos, nomeadamente, de interferómetros Fabry-Perot, anéis em fibra óptica e redes de Bragg em fibra óptica. É também proposto um filtro óptico baseado numa rede de Bragg com um desvio de fase de π e os requerimentos necessários para ser implementado num sistema LIDAR são analisados. Finalmente, é feita uma exposição sobre a sua configuração assim como o resultado de algumas simulações.

Por último, no interesse de dar continuidade à investigação na tecnologia dos sensores e filtros baseados em redes de Bragg em fibra óptica, são apresentadas algumas sugestões para trabalho futuro.

Summary

This dissertation deals with applications of fibre Bragg grating based structures for optical sensing and filtering. It overviews the technology of Bragg gratings in optical fibres and is focused on a particular type of fibre Bragg grating: *the phase-shifted Bragg grating*. Some simulation results are discussed and reported the main spectral characteristics of the devices fabricated in-house.

It is presented the technology of grating based fibre Fabry-Perot (FFP) interferometers for dynamic strain sensing. Two strain sensing configurations based on a phase modulation technique and the sensing system demodulation is described. Also, an interrogation technique for a FFP interferometer based on the dynamic modulation of a π-shifted grating by means of a PZT disk is proposed as well as the theoretical aspects and experimental results.

A specific type of optical fibre sensors is presented: *the short fibre tapers*. Some configurations based on the combination of fibre Bragg gratings with short tapers and its sensing characteristics are described. Theoretical aspects and experimental results of fibre strain sensitivity under the mechanical action of short tapers are also discussed.

The general aspects of optical filtering in LIDAR systems are presented. In particular, the characteristics of some optical filters, namely, the Fabry-Perot interferometers, fibre ring resonators and fibre Bragg gratings are described. Then, the requirements of an optical filtering subsystem based on a π-shifted fibre Bragg grating to be implemented in a LIDAR configuration are analyzed and, finally, the design and simulations of the proposed optical fibre filter are addressed.

Finally, in order to give continuity with the work developed in the area of fibre Bragg grating sensors and filters it is presented some suggestions for future work.

Index

1

Introduction

Optical fibre sensors may be defined as devices through which a physical, chemical, biological, or other measurand interacts with light, either guided in an optical fibre (intrinsic sensor) or guided to an interaction region (extrinsic sensor) by an optical fibre, to produce an optical signal related to the parameter of interest. Fibre sensors can be designed so that the measurand interacts with one or several optical parameters of the guided light (intensity, phase, polarization, and wavelength). Independently of the sensor type, the light modulation must be processed into an optical intensity signal at the receiver, which subsequently performs a conversion into an electric signal. In general, the main interest in this type of sensors comes from the fact that the optical fibre itself offers numerous operational benefits. It is electromagnetically passive, so it can operate in high and variable electric field environments (like those typical of the electric power industry); it is chemically and biologically inert since the basic transduction material (silica) is resistant to by most chemical and biological agents; its packaging can be physically small and lightweight. Taking the advantage of the intrinsic low optical attenuation of the fibre, it is possible to attain distributed sensing, where the measurand can be determined as a function of the position along the length of the fibre simply by interrogating the fibre from one end. Also, the optical fibre can be operated over very long transmission lengths, so that the sensor can easily be placed kilometers away from the monitoring local and data can be reliable transmitted between the two. Adding to this, it is also possible to perform multiplexed measurements using large arrays of remote sensors, operated from a single optical source and detection unit, with no active optoelectronic components located in the measurement area, thereby retaining electromagnetic passiveness and environmental resistance [1, 2].

Due to all these favorable characteristics, fibre sensing has been the focus of substantial R&D along the years and many solutions for field applications came out

from this effort [3]. However, it is nowadays recognized that a clear breakthrough occurred with the development of in-fibre Bragg gratings. Indeed, these devices, besides the conceptually novel developments they triggered, allowed also a range of applications that by its dimension and diversification has no parallel in the fibre sensing field. The reasons for that are diverse but, in short, they are related to their small size and intrinsic nature, as well as to the fact that a given measurand acting on these structures modulates an absolute parameter, namely the wavelength of the reflected light [4, 5].

Fibre Bragg gratings (FBGs) are important devices far behind the optical fibre sensing field. Actually, it is in the optical fibre communication domain where these fibre structures found core relevance. The reasons for that overlap those mentioned in the fibre sensing context, with the addition of a new one of crucial importance, namely the tuneable bandpass filtering characteristics (amplitude and phase) of these devices. The full exploitation of this potential allowed the conception and implementation of novel fibre optic communication systems with far better performance comparatively to what was possible to achieve before the FBGs out came [6].

It is also worthwhile to notice that these FBG filtering properties are important outside the communication (and sensing) fields. They can be used with advantage in the conception and implementation of solutions in other areas of optics, such as in spectroscopy [7].

This dissertation deals with applications of fibre Bragg grating based structures for optical sensing and filtering. In Chapter 2 it is presented the technology of Bragg gratings in optical fibres. It starts with Bragg gratings historic background and reviews the fabrication techniques most frequently used. The general properties of Bragg gratings are presented and the coupled mode theory is described. Finally, some simulation results of specific grating structures are analyzed and some sensing properties are reviewed. Chapter 3 is focused on a particular type of fibre Bragg grating: *the phase-shifted Bragg grating*. First, the general properties of phase-shifted gratings is presented; then, two other types of transmitting filters based on Bragg gratings, namely, Moiré Bragg gratings and chirped Bragg gratings with a discontinuity, are briefly described. Also, the fabrication techniques of phase-shifted Bragg gratings are overviewed as well as the theoretical aspects that ground them. Finally, some simulation results are discussed and reported the main characteristics of the devices fabricated in-

house. In Chapter 4 it is presented the technology of grating based fibre Fabry-Perot interferometers for dynamic strain sensing. Introduces with general aspects of Fabry-Perot interferometers (FPI) and in particular describes the properties and different types of FPI based on fibre Bragg gratings. Two sensing configurations are proposed as applications as strain sensing structures. The sensing system demodulation is described and the respective strain measurement results are analyzed. Finally, a dynamic demodulation scheme of a grating based fibre Fabry-Perot sensor is proposed and the theoretical aspects and experimental results are presented and discussed. In Chapter 5 it is presented a specific type of optical fibre sensors: *the short fibre tapers*. It starts with general properties of fibre tapers and overviews some fabrication techniques. Then it is described some configurations based on the combination of fibre Bragg gratings with short tapers and its sensing characteristics are analyzed. Theoretical aspects and experimental results of fibre strain sensitivity under the mechanical action of short tapers are also discussed. Chapter 6 deals with the general aspects of optical filtering in LIDAR systems. In particular, describes the characteristics of some optical filters, namely, the Fabry-Perot interferometers, fibre ring resonators and fibre Bragg gratings. It focuses the attention to the requirements of an optical filtering subsystem to be implemented in a LIDAR system and, finally, it is presented and discussed the design and simulations of the proposed optical fibre filter. Chapter 7 ends with the conclusions, final remarks and future work to be developed.

2

Fibre Bragg Gratings

Since the discovery of photosensitivity in optical fibres there has been great interest in the fabrication of Bragg gratings within the core of a fibre. The ability to inscribe intracore Bragg gratings in these photosensitive fibres has revolutionized the field of telecommunications and optical fibre based sensor technology. Over the last decade, the number of researchers investigating fundamental, as well as application aspects of these gratings has increased dramatically. This section presents the technology of Bragg gratings in optical fibres. It starts with Bragg gratings historic background and then proceeds to review some of the most common fabrication techniques (interferometric, phase mask, point by point and mask displacement/beam scanning). The general properties of Bragg gratings are presented and the coupled mode theory is described. Finally, simulation results of specific grating structures are discussed and some sensing properties are reviewed.

.

2.1   Historic Introduction

The first observations of refractive index changes were noticed in germanium-doped silica fibre and were reported by Hill *et al.* in 1978 [8, 9]. During an experiment that was carried out to study the nonlinear effects in a specially designed optical fibre, visible light from an argon ion laser was launched into the core of the fibre. Under prolonged exposure, an increase in the attenuation of the fibre was observed. Following that observation, it was determined that the intensity of the light back reflected from the fibre increased significantly with time during the exposure. This increase in reflectivity was the result of a permanent refractive-index grating being photoinduced in the fibre. This new nonlinear photorefractive effect in optical fibres was called photosensitivity. In this experiment, an argon ion laser line at 488nm was launched into the core of a

specially designed fibre (small core diameter and heavily doped with germanium). The laser light interfered with the Fresnel reflected beam and initially formed a weak standing-wave intensity pattern. The high intensity points altered the index of refraction in the photosensitive fibre core permanently, forming a refractive index perturbation that had the same spatial periodicity as the interference pattern, with a length only limited by the coherence length of the writing radiation. This refractive index grating – Hill's grating – acted as a distributed reflector that coupled the forward propagating to the counter-propagating light beams. The coupling of the beams provided positive feedback, which enhanced the strength of the back-reflected light, and thereby increased the intensity of the interference pattern, which in turn increased the index of refraction at the high intensity point. This process was continued until the reflectivity of the grating reached a saturation level. This particular grating had a very weak index modulation, which was estimated to be of the order of 10^{-6}, resulting in a narrow-band reflection filter at the writing wavelength.

Photosensitivity in optical fibres remained dormant for several years after its discovery, mainly due to limitations of the writing technique. During that time, two significant results were attained. The first one was demonstrated in 1981, by Lam & Garside [10], where it was demonstrated that the magnitude of the photoinduced refractive index modulation depended on the square of the writing power at the argon ion wavelength. This suggested a two-photon process as the possible mechanism of refractive index change. The second result was reported in 1985 by Parent *et al.* [11] that the photoinduced change in the refractive index was anisotropic, despite the significance of the result was not appreciated immediately. Anisotropy is an unusual property of photosensitivity in optical fibres. It was demonstrated that the reflectivity of internally written gratings is found to depend on the polarization of the reading light beam, – i.e., the refractive index measured with light polarized parallel to the writing beam's direction of polarization is slightly different than that measured for light polarized perpendicular to the writing beam polarization –. This photoinduced refractive index change is called birefringence.

Despite the potentialities of this new technology, few advances were made because photosensibility was found in a limited number of optical fibres highly doped with germanium. Besides, the spectral response of Hill's gratings was limited to the writing beam wavelength as well as the writing fabrication technique.

In 1989, *Meltz et al.* [12] presented a new fabrication technology of Bragg gratings in the core of a germanium doped optical fibre by exposing the fibre externally from the side to an interference pattern in the UV spectral region. To form the interference pattern within the core of the fibre, an UV light beam from a laser was split into two beams that were intersected in the fibre core. The UV writing wavelength range was chosen to be 240-250nm (nearly half de wavelength at 488nm in argon laser). This wavelength was close to the absorption peak at ~240nm of an oxygen deficiency in atomic structure of the optical fibre. This oxygen-deficient germanium defect is though to be responsible for the photosensitivity in germanium doped silica. The choice of UV wavelength was based on the fact that photosensitivity is a two photon absorption process in the visible region, and thus should be a one photon absorption process in the UV region. The interaction of two beams in the core of the optical fibre resulted in an interference pattern that would be converted, by photosensitivity, in core's refractive index spatial modulation, giving rise to diffraction gratings. The new external fabrication technique depends not only on the wavelength of the light used for writing, but also on the angle between the two interfering light beams. Thus, gratings can be written at any wavelength by simply adjusting the incidence angle.

Using the process of one photon absorption resulted in the increase of the photosensitivity mechanism efficiency, essentially due to the direct excitation of the absorption line at 244nm characteristic of germanium doped silica. This was an important step towards the development of different UV writing techniques, making possible flexible fabrication of fibre Bragg gratings.

2.2   Fabrication Techniques of Optical Fibre Bragg Gratings

Photosensitivity permits the fabrication of a variety of different types of refractive index gratings in the core of optical waveguides. Fabrication techniques have been subject of much research owing to the driving force arising from communications and sensing applications. A number of schemes have been demonstrated to reach requirements such as flexibility, good repeatability and low cost mass production capability, which as led to successful commercialization of FBGs.

In this sub-section, it will be described some of the most common fabrication techniques, namely, the interferometric technique, the phase mask technique, the point-by-point technique and the moving fibre/phase mask scanning technique.

2.2.1   Interferometric Fabrication Technique

The interferometric fabrication method was the first external writing technique to enable the fabrication of Bragg gratings in photosensitive optical fibre [12]. This method uses an amplitude splitting interferometer that splits the incoming UV light into two beams that are recombined to form an interference pattern (see Figure 2.1). When the photosensitive fibre is exposed to the fringe pattern, a refractive index modulation is induced in the core. Bragg gratings in optical fibres have been fabricated using both amplitude splitting and wavefront splitting interferometers.

In the amplitude splitting interferometer – holographic method – the UV writing laser light is split into two equal intensity beams that are recombined after traveling through different optical paths. Normally cylindrical lenses are used to focus the two interfering beams in the core of the fibre, building in this way the interference pattern.
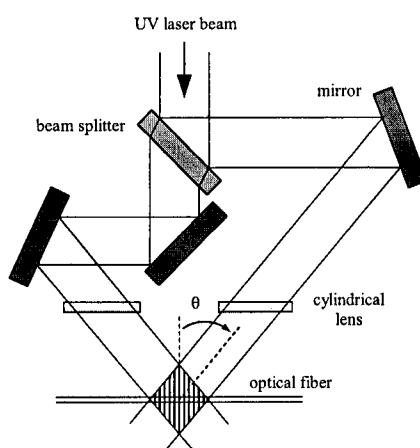
Figure 2.1 – Experimental setup for the fabrication of Bragg gratings in optical fibre by UV irradiation interferometer method. [22]

The Bragg grating period (Λ), which is identical to the period of the interference fringe pattern, depends on both the irradiation wavelength (λ_{UV}) and the half-angle (θ) between the intersecting UV beams:

$$\Lambda = \frac{\lambda_{UV}}{2\sin\theta}. \qquad\qquad (2.1)$$

The choice of λ_{UV} is limited to the UV photosensitivity region of the fibre, however, there is no restriction set on the choice of the angle.

The most important advantage offered by the holographic method is the ability to inscribe Bragg gratings at any wavelength. This is accomplished by simply changing the intersecting angle between the two beams. The main disadvantage is its susceptibility to mechanical vibrations. Displacements as small as submicrons in the position of mirrors, beam splitters as well as different optical paths, might cause problems in forming stable fringe pattern.

In the wavefront splitting interferometer a prism interferometer made from high homogeneity ultraviolet-grade fused silica is used. In this setup, the UV beam is expanded laterally by refraction at the input face of the prism. The expanded beam is spatially bisected by the prism edge, and half of the beam is spatially reversed by total internal reflection from the prism face. The two half-beams are then recombined at the output face of the prism, giving a fringe pattern parallel to the photosensitive fibre core. A cylindrical lens placed just before the setup helps in forming the interference pattern on a line along the fibre core.

The main advantage of this fabrication technique is that less optical components are used, reducing the sensitivity to mechanical vibrations. Furthermore, this assembly can be rotated easily to vary the intersection angle of the two beams for wavelength tuning. However, this is a complex operation because it demands continuous corrections of the intersection beam position in order to maximize the interference pattern length.

2.2.2 Phase Mask Technique

The phase mask technique is an external and noninterferometric fabrication technique and one of the most effective methods for inscribing Bragg gratings in photosensitive optical fibre, due to its simplicity and good reproducibility [13].

The phase mask is a high quality fused silica substrate transparent to the UV beam. In its flat surface, of extreme perfection, is formed a diffraction grating by lithography. Hence, the phase mask becomes an optical element with the capability to diffract the

UV beam in transmission. The interference of the transmitted beams corresponds to different diffraction orders in the proximity of the surface, originating a fringe pattern, and leading to Bragg gratings fabrication by modulation of the refractive index in the core of the optical fibre.

The profile of the phase grating is chosen such that the zero-order diffracted beam is suppressed to less than 1% of the transmitted power. In addition, the principal beams diffracted by the phase mask correspond to plus and minus first orders, containing each one, typically, more than 35% of the transmitted power. As it will be shown in the next section, a near-field fringe pattern is produced by the interference of these two orders whose period, Λ, is one-half of the phase mask period:

$$\Lambda = \frac{1}{2}\Lambda_{mask} \,.$$

(2.2)

Figure 2.2 illustrates the experimental setup used in fibre Bragg gratings fabrication using phase mask technique. The interference pattern photoimprints a refractive index modulation in the core of a photosensitive optical fibre placed in contact, or in close proximity, immediately behind the phase mask. The fringe pattern is focused along the fibre core with the help of a cylindrical lens.
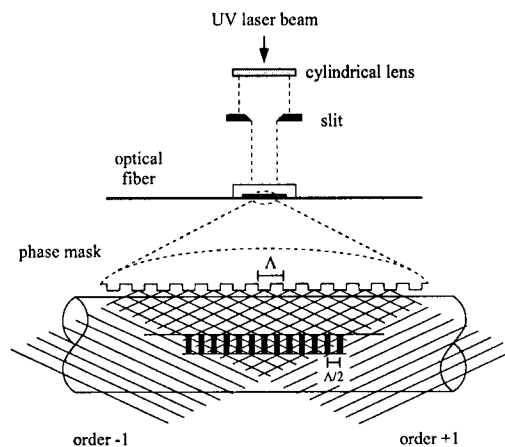
Figure 2.2 – Experimental setup for fibre Bragg gratings fabrication by phase mask technique. The detail shows that the fringe pattern period is always half the period of the phase mask. [12]

The phase mask greatly reduces the complexity of the fibre grating fabrication system. The simplicity of this technique provides a robust and inherently stable method for reproducing fibre Bragg gratings. Since the fibre is usually placed behind the phase mask, sensitivity to mechanical vibrations and, therefore, stability problems are minimized. One of the main advantages of this method is that it allows using laser beams with low spatial and temporal coherence to form interference.

In face of the importance of phase masks in the context of fibre grating fabrication, it is justifiable a more close look on the theory behind its operation, which is detailed next section.

2.2.2.1   Theory of Phase Mask Operation

Diffraction gratings have found many applications as optical filters, beam splitters, and lenses and also have special applications in holography, astronomy, electron microscopy, laser tuning, fibre grating fabrication and other fields [14, 15]. Several researchers have obtained rigorous solutions for the exact electromagnetic boundary value problem that apply to gratings with rectangular or triangular grooves [16, 17]. Others have obtained approximate results by applying perturbation techniques [18]. For gratings with arbitrary profiles, the integral method [19] was first used and later the differential method was developed [20]. This section presents the diffraction analysis of gratings with rectangular grooves and, in particular, the *grating equation* is derived [21].

A diffraction grating is a repetitive array of diffracting elements, either apertures or obstacles, which has the effect of producing periodic alterations in the phase, amplitude or both, of an emergent wave. A common form of diffraction grating is made by etching parallel grooves into the surface of a flat, clear glass plate. Each groove serves as a source of scattered light and together they form a regular array of parallel lines sources. When the grating is totally transparent, so that there is negligible amplitude modulation, the regular variations in the optical thickness across the grating yield a modulation in *phase* that is defined as a *transmission phase grating*. The analysis of this type of gratings is essentially the same as that used when considering diffraction by many slits.

Consider the case of N long, parallel, narrow slits each of width b, and center to center separation a, as illustrated in Figure 2.3.
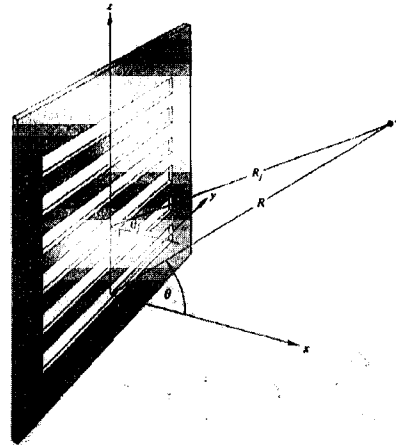
Figure 2.3 – Definition of multi-slit geometry. [21]

If the origin of the coordinate system is at the center of the first slit, the total optical disturbance at a point on the observation screen is given by

$$E = C \int_{-b/2}^{b/2} F(z)dz + C \int_{a-b/2}^{a+b/2} F(z)dz + C \int_{2a-b/2}^{2a+b/2} F(z)dz + ... + C \int_{(N-1)a-b/2}^{(N-1)a+b/2} F(z)dz \qquad (2.3)$$

where $F(z) = \sin[\omega t - k(R - z\sin\theta)]$. This applies to the Fraunhofer condition, so that all of the slits are considered to be close to the origin and the approximation

$$r = R - z\sin\theta \qquad (2.4)$$

applies over the entire array. To obtain the contribution from the jth slit (where the first one is numbered zero), one evaluate the integral in equation (2.3),

$$E_j = \frac{C}{k\sin\theta}[\sin(\omega t - kR)\sin(kz\sin\theta) - \cos(\omega t - kR)\cos(kz\sin\theta)]_{ja-b/a}^{ja+b/2} \qquad (2.5)$$

requiring that $\theta_j \approx \theta$. According with equation (2.4) and Figure 2.3, $R_j = R - ja\sin\theta$ so that $2\alpha j - kR = -kR_j$. After some manipulation equation (2.5) becomes

$$E_j = bC\left(\frac{\sin\beta}{\beta}\right)\sin(\omega t - kR + 2\alpha j) \qquad (2.6)$$

where $\beta = (kb/2)\sin\theta$ and $\alpha = (ka/2)\sin\theta$. The total optical disturbance as given by equation (2.3) is simply the sum of the contributions from each of the slits:

$$E = \sum_{j=0}^{N-1} E_j \qquad (2.7)$$

or

$$E = \sum_{j=0}^{N-1} bC\left(\frac{\sin\beta}{\beta}\right)\sin(\omega t - kR + 2\alpha j) \qquad (2.8)$$

Since $e^{i\theta} = \cos\theta + i\sin\theta$, equation (2.8) can be written as the imaginary part of a complex exponential:

$$E = \text{Im}\left[bC\left(\frac{\sin\beta}{\beta}\right)e^{i(\omega t - kR)}\sum_{j=0}^{N-1} e^{(i2\alpha)^j} \right]. \qquad (2.9)$$

Simplifying this geometric series, one obtain

$$E = bC\left(\frac{\sin\beta}{\beta}\right)\left(\frac{\sin N\alpha}{\sin\alpha}\right)\sin[\omega t - kR + (N-1)\alpha] \qquad (2.10)$$

The distance from the center of the array to the point P is equal to $[R - (N-1)(a/2)\sin\theta]$ and, therefore, the phase of E at P corresponds to that of a wave emitted from the midpoint of the source. The flux-density distribution function is

$$I(\theta) = I_o\left(\frac{\sin\beta}{\beta}\right)^2\left(\frac{\sin N\alpha}{\sin\alpha}\right)^2. \qquad (2.11)$$

Note that I_o is the flux density in the $\theta = 0$ direction emitted by any one of the slits and that $I(0) = N^2 I_o$. In other words, the waves arriving at P are all in phase and their fields add constructively. Each slit by itself would generate precisely the same flux – density distribution. *Principal maxima* occur when

$$\frac{\sin(N\alpha)}{\sin\alpha} = N \Rightarrow \alpha = 0, \pm\pi, \pm2\pi,... \qquad (2.12)$$

or, since $\alpha = (ka/2)\sin\theta$, equation (2.12) will be equivalent to

$$a\sin\theta_m = m\lambda \qquad (2.13)$$

with $m = 0, \pm1, \pm2,...$ specifying the *order* of the various *principal maxima*. This result is known as the *grating equation* for normal incidence. It is quite general and is the first step for diffraction analysis of phase masks.

As indicated before, a major step toward easier inscription of optical fibre gratings was made possible by the application of the phase mask as a component of the system fabrication. Used in transmission, a phase mask is a relief grating etched in a silica plate. The significant features of the phase mask are the grooves etched into a UV-transmitting silica mask plate, with a carefully controlled mark-space ratio as well as etch depth. The principle of operation is based on the diffraction of an incident UV beam into several orders, $m = 0, \pm1, \pm2,....$ This is shown in Figure 2.4 and corresponds to the general situation of oblique incidence.
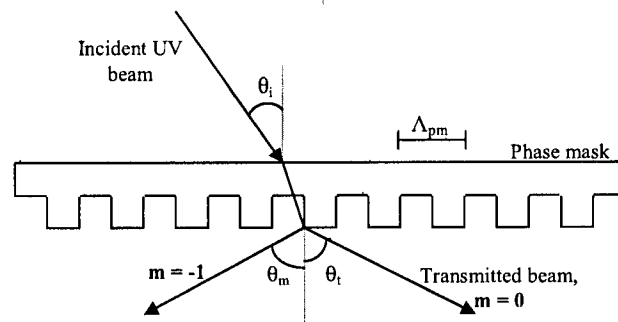
Figure 2.4 – A schematic of the diffraction of an incident beam from a phase mask.

The incident and diffracted orders satisfy the general grating equation, which becomes

$$a(\sin\theta_m - \sin\theta_i) = m\lambda. \qquad (2.14)$$

In this case, $a = \Lambda_{pm}$ is the period of the phase mask and equation (2.14) reduces to the form

$$\Lambda_{pm} = \frac{m\lambda}{\sin\theta_m - \sin\theta_i} \tag{2.15}$$

where θ_m is the angle of the diffracted order, λ is the wavelength and θ_i the angle of the incident UV beam. When the period of the grating lies between λ and $\lambda/2$, the incident wave is diffracted into only a single order $(m = 1)$ with the rest of the power remaining in the transmitted wave $(m = 0)$.

As the UV radiation is at normal incidence, $\theta_i = 0$, the diffracted radiation is split into $m = 0$ and $m = \pm 1$ orders, as shown in Figure 2.5.
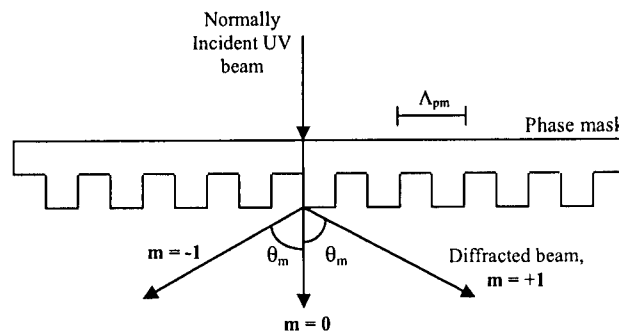
Figure 2.5 – Normally incident UV beam diffracted into ± 1 orders. The remnant radiation exits the phase-mask in the zero order $m = 0$.

In this case, the interference pattern at the optical fibre of two such beams of orders ± 1 has a period Λ related to the diffraction angle by

$$\Lambda = \frac{\lambda}{2\sin\theta_m} = \frac{\Lambda_{pm}}{2}. \tag{2.16}$$

The period Λ_{pm} of the grating etched in the mask is determined by the Bragg wavelength λ_B required for the grating in the fibre (see section 2.3); using equation (2.16) it is obtained

$$\Lambda = \frac{\lambda_B}{2n_{eff}} = \frac{\Lambda_{pm}}{2}.$$ (2.17)

2.2.3   Point-by-point Technique

The point-by-point technique for fabricating Bragg gratings is accomplished by inducing at a time each individual modulation period of the refractive index along the core of the fibre [13]. Figure 2.6 illustrates the experimental setup. A single pulse of UV light from an excimer laser passes through a mask containing a slit. A focusing lens images the slit onto the core of the optical fibre from the side, inducing an individual modulation in the refractive index. Using a translational system, the fibre is translated in a direction parallel to its axis and the process is repeated to form the grating structure. Hence, each grating period is produced independently.
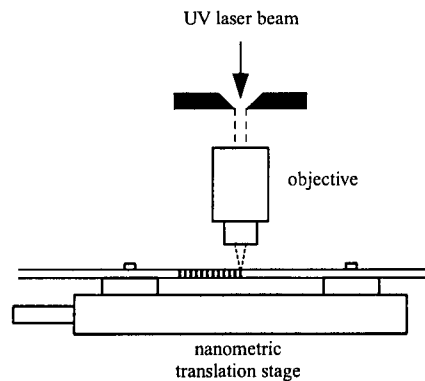
Figure 2.6 – Experimental setup for fibre Bragg gratings fabrication by point-by-point technique. [22]

The main advantage of this writing technique lies in its flexibility to vary Bragg grating parameters such as grating length, grating pitch and spectral response. However, it is also a very demanding method in terms of precision and stability of the translation of the beam and of the focusing quality, while offering low flexibility in the definition of the modulation period.

2.2.4   Moving Phase Mask/Scanning Beam Technique

In many applications it is needed complex Bragg grating structures such as apodized, phase-shifted or chirped gratings that require different methods other than the simple phase mask technique. One of the several methods proposed to fabricate such complex structures is the moving phase mask/scanning beam technique.

The optical source used for the photoinscription is typically a frequency doubled CW Argon laser at 244 nm. The UV laser beam is directed to an acousto-optical modulator by a mirror. The modulator controls the power passing through by deflecting the incident beam from zero-order to first-order according to the voltage applied to the cell. A mirror, a cylindrical lens and a slit are mounted on a translation stage in order to have the ability to scan the beam over the defined grating length. The cylindrical lens is used to focus the beam on the photosensitive optical fibre, and the slit controls the lateral dimension of the beam incident on the fibre.

A standard uniform phase mask is held on a proper machined aluminum holder with the ability of being dithered and/or displaced by a piezotranslator (PZT). The phase mask is slowly moved during the UV beam scanning, overcoming the limitations associated with the use of uniform phase masks. The optical fibre is then placed after the phase mask, in the focal plane of the lens.

For apodized Bragg gratings, the phase mask is dithered according to a predefined profile defined for each position along the grating, resulting in high refractive index modulation amplitude (for low dithering amplitude) or low modulation amplitude (for high dithering amplitude) while maintaining a constant mean refraction index along the total grating length. For chirped gratings, the phase mask is displaced with a non-uniform velocity along the grating length, resulting in a variable relative ratio between the phase mask and the beam scanning velocities. Phase shifted Bragg gratings are achieved by a very well quantified and controlled displacement of the phase mask in the correct position or positions of the grating during its photoinscription. This allows structuring the grating spatial profile, in order to obtain gratings with variable phase steps, or more complex structures like sampled Bragg gratings.

This technique has the major advantage of inducing a constant average refractive index change, since the average UV fluency is constant along the grating length. It also enables the creation of more complex structures, like chirped and phase shifted gratings,

by executing a proper movement of the phase mask while beam scanning is being performed.

2.3   Properties of Fibre Bragg Gratings

In its simplest form, a fibre Bragg grating consists of a periodic modulation of the index of refraction in the core of a single-mode optical fibre and is considered the fundamental building block for most Bragg grating structures [13]. Each grating plane has constant period Λ ($K = 2\pi / \Lambda$ is the wave vector of the grating) and acts as a localized mirror which reflects the light guided along the core of the fibre. The refractive index profile along the fibre axis z can be represented as

$$n(z) = n_{co} + \Delta n \cos\left(\frac{2\pi z}{\Lambda}\right), \tag{2.18}$$

where n_{co} and Δn are the core's refractive index and its amplitude modulation, respectively. Figure 2.7 shows a simple scheme about the behavior of light guided in the core of the optical fibre when the refractive index is periodically modulated.
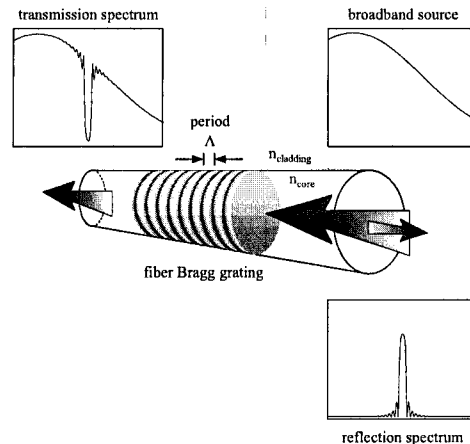
Figure 2.7 – Schematic representation of fibre Bragg gratings principle of operation, with reflection and transmission spectral response.[22]

The Bragg grating condition is simply the requirement that satisfies momentum conservation. When Bragg condition is satisfied, the contributions of reflected light

from each plane add constructively in the backward direction to form a back-reflected peak with a center wavelength defined by the grating parameters. The resonant of this back-reflected peak is the so-called Bragg wavelength (λ_B) and is defined by the following Bragg grating condition:

$$\lambda_B = 2n_{eff}\Lambda.$$ (2.19)

Using the coupled-mode theory, an analytical description of the reflection properties of Bragg gratings may be obtained. The reflectivity of a grating with constant modulation amplitude and period is given by the following expression:

$$R = \frac{\kappa^2 \sinh^2(SL)}{\Delta\beta^2 \sinh^2(SL) + S^2 \cosh^2(SL)},$$ (2.20)

where L is the grating length and $S = \sqrt{\kappa^2 - \Delta\beta^2}$, where the detuning parameter is given by $\Delta\beta = \beta - \pi/\Lambda$ and $\beta = 2\pi n_{co}/\lambda$ is the propagation constant. The coupling coefficient, κ, for the sinusoidal variation of index perturbation along the fibre axis is given by:

$$\kappa = \frac{\pi\Delta n}{\lambda}\eta,$$ (2.21)

where η is the confinement factor of the guided mode. At the Bragg grating resonance wavelength there is no detuning, $\Delta\beta = 0$, which corresponds to maximum reflectivity. Therefore, the expression for the reflectivity becomes:

$$R = \tanh^2(\kappa L).$$ (2.22)

Depending on some parameters variation, such as grating length and magnitude of induced index change, it is possible to obtain narrow-band transmission as well as high reflectivity of the Bragg resonance. Optimization of these parameters is fundamental when the objective is to use fibre Bragg gratings in band-pass filtering applications such

as wavelength multiplexing, add/drop operations and discrimination of gas emission lines.

2.3.1   Transmission Filtering Using Bragg Gratings

Bragg gratings photoinscribed in single-mode optical fibres act as rejection band filters, once it reflects all the wavelengths around Bragg's resonance [22]. Although Bragg gratings appear to be specially indicated for band-pass filtering, due to its narrow spectral response with low losses, the inherently reflection operation doesn't allow its direct integration in most applications where, in general, transmission filtering operation is required. Thus, Bragg gratings are associated to other optical components that give access to band-pass filtering, despite being an additional degree of complexity.

One of the simplest schemes to achieve transmission Bragg grating spectral filtering is to associate the Bragg grating to a 3dB directional coupler. However, this arrangement has inherent high losses that limit its use in many applications, in particular optical communications.

A more efficient system is based on the use of an optical circulator instead of a directional coupler. The optical circulator is an inherently non-reciprocal component with multiple in and out ports. The high isolation level between ports allows filtering implementation with excellent isolation level in transmission and high background losses.

More complex structures make use, for example, of two Bragg gratings placed in the arms of a 3dB directional coupler, forming a Michelson interferometer configuration. Integrating a second directional coupler to combine the signals out of the selection band, then a Mach-Zehnder interferometer configuration is formed. The fabrication of these structures is in practice quite difficult, since filtering performance may be compromised by variations of the coupling relation between directional couplers, the spectral response of Bragg gratings and the relative phase of the transmitted and reflected signals. The spectral response stabilization is the main disadvantage of interferometric filters, which are extremely affected by phase variations that are caused by temperature and/or strain variations.

Furthermore, other resonant band-pass filters based on multiple Bragg gratings association should be considered, in particular Fabry-Perot filters based on uniform or chirped Bragg gratings.

2.3.2   Apodization of the Spectral Response of Bragg Gratings

The reflection spectrum of a finite-length Bragg grating with uniform modulation of the refractive index is always accompanied by a series of side lobes at adjacent wavelengths [22]. These side lobes are originated by refractive index discontinuity in the extremities of the Bragg grating basically acting as a Fabry-Perot cavity.

In many applications it becomes very important to minimize and, if possible, eliminate the reflectivity of the side lobes. In wavelength division multiplexed techniques (WDM), the use of multiple Bragg gratings with adjacent frequencies implies excellent isolation level between ports; thus, the presence of side lobes decreases the performance operation of WDM systems. Side lobes also affect the efficiency of chirped gratings when used for dispersion compensation. In these situations it is necessary to use apodization techniques in order to suppress the side lobes present in the spectral response of the Bragg gratings.

In practice, apodization is accomplished by varying the amplitude of the coupling coefficient along the length of the grating – i.e., decreasing gradually the modulation amplitude of the refractive index in the extremities of the grating, in order to minimize the discontinuity –.

Apodization can be achieved by simply varying the intensity of the UV writing beam along the grating length; however, the corresponding variation in the average refractive index induces an undesired chirp that needs to be compensated by another exposure through an amplitude mask [23]. Besides this method of achieving simple apodization, there are also methods that allow the fabrication of Bragg gratings with pure apodization, i.e., varying the modulation amplitude keeping constant the effective index. One example is the use of a complex phase mask with variable diffraction efficiency [24]. Another approach is the moving fibre/scanning beam, where pure apodization is achieved by the application of a variable dither to the fibre during the photoinscription process [25, 26]. This technique can be applied directly to the phase mask, instead of the fibre, as already discussed in the section dealing with fibre Bragg

grating fabrication techniques. In short, the phase mask is dithered according to the profile defined for each position along the grating, resulting in high refractive index modulation amplitude (for low dithering amplitude) or low modulation amplitude (for high dithering amplitude), while maintaining a constant mean refraction index change along the total length of the grating.

2.4   Coupled Mode Theory

This section will be focused on the general understanding of the theory of a fibre Bragg grating structure, developing further the basic concepts presented previously. Before developing the quantitative analysis using couple-mode theory, it will be considered a qualitative picture of the interactions of interest in a diffraction grating.

2.4.1   Resonant Wavelength for Diffraction Gratings

Fibre gratings can be broadly classified according to coupling characteristics into the following three types:

- Bragg gratings (FBG) or reflection gratings, in which coupling occurs between modes traveling in opposite directions (Figure 2.8a);
- Transmission gratings or long-period gratings, in which the coupling is between modes traveling in the same direction (Figure 2.8b);
- Slanted or tilted grating, in which most of the guided radiation is coupled into backward radiation or cladding modes (Figure 2.8c).

Here only Bragg gratings will be considerer. These structures are simply an optical diffraction grating, which means that its effect upon a light wave incident on the grating at an angle θ_1 can be described by the familiar grating equation [27]

$$n\sin\theta_2 = n\sin_1 + m\frac{\lambda}{\Lambda},$$ (2.23)

where θ_2 is the angle of the diffracted wave and the integer m determines the diffraction order. Figure 2.9 illustrates a simple scheme of a light wave being diffracted by a grating.

(a)

(b)

(c)
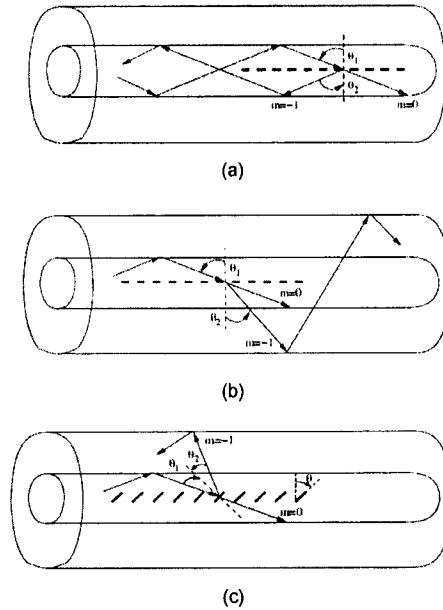
Figure 2.8 – Different types of fibre gatings: (a) Bragg grating; (b) long-period grating; (c) tilted grating. [27]
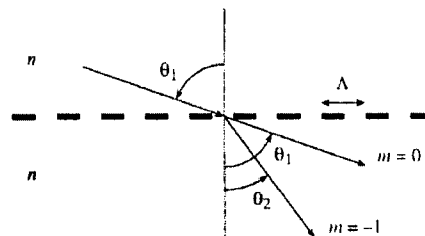
Figure 2.9 – Diffraction of a light wave by a grating. [27]

Equation (2.23) predicts only the direction θ_2 into which constructive interference occurs, but it is nevertheless capable of determining the wavelength at which a fibre grating most efficiently couples light between two modes. In a fibre Bragg grating, a mode with bounce angle of θ_1 is reflected into the same mode travelling in the opposite direction with a bounce angle of $\theta_2 = -\theta_1$. Since the mode propagation constant β is

simply $\beta = \dfrac{2\pi}{\lambda} n_{eff}$, where $n_{eff} = n_{co} \sin\theta$ and n_{co} is the core's refractive index of the

optical fibre, equation (2.23) can be rewritten for guided modes as

$$\beta_2 = \beta_1 + m\frac{2\pi}{\Lambda}. \qquad (2.24)$$

First order diffraction usually dominates in a fibre grating which corresponds to $m = -1$ in the above equation. Negative β values describe modes that propagate in the $-z$ *(backwards)* direction. Recognizing $\beta_2 < 0$, it can be shown that the resonant wavelength for reflection of a mode of index $n_{eff,1}$ into a mode of index $n_{eff,2}$ is

$$\lambda = \left(n_{eff,1} + n_{eff,2} \right)\Lambda. \qquad (2.25)$$

When the two modes are identical, $\beta_2 = -\beta_1$, a resonance condition is obtained at a particular wavelength, known as Bragg reflection wavelength, which is given by

$$\lambda_B = 2n_{eff}\Lambda. \qquad (2.26)$$

This is called Bragg condition and it gives the central wavelength for which the optical grating is going to reflect the guided light wave.

2.4.2 Fundamentals of Coupled-Mode Theory

A diffraction grating is an intrinsic structure which changes the spectrum of an incident signal by coupling energy to other fibre modes. As seen before, in the simplest case the incident wave is coupled to a counterpropagating like mode and thus reflected. Coupled-mode theory is a good tool for obtaining quantitative information about the diffraction efficiency and spectral dependence of fibre gratings. Only a brief overview of this theory is presented here; detailed descriptions can be found in numerous articles and texts [28-30].

In the ideal mode approximation to coupled-mode theory, it will be assumed that the transverse component of the electric field can be written as a superposition of the ideal modes (j) in an ideal waveguide with no grating perturbation, such that

$$\vec{E}^T(x,y,z,t) = \sum_j \left[A_j(z)\exp(-i\beta_j z) + B_j(z)\exp(i\beta_j z) \right] \vec{e}_j^T(x,y)\exp(i\omega t), \qquad (2.27)$$

where $A_j(z)$ and $B_j(z)$ are slowly varying amplitudes of the jth mode with propagation in +z and –z directions, respectively. The transverse mode fields $\vec{e}_j^T(x,y)$ describe LP radiation modes. In ideal conditions, these modes are orthogonal and, hence, do not change energy.

The presence of a periodic perturbation $\Delta\varepsilon(x,y,z)$ in the dielectric constant causes, in general, the modes to be coupled such that the amplitudes $A_j(z)$ and $B_j(z)$ of the jth mode evolve along the z axis according to

$$\frac{dA_j}{dz} = -i\sum_k A_k \left(K_{kj}^T - K_{kj}^z \right)\exp\left[i\left(\beta_j - \beta_k\right)z \right] - i\sum_k B_k \left(K_{kj}^T + K_{kj}^z \right)\exp\left[i\left(\beta_j + \beta_k\right)z \right]$$

$$(2.28)$$

and

$$\frac{dB_j}{dz} = i\sum_k A_k \left(K_{kj}^T - K_{kj}^z \right)\exp\left[-i\left(\beta_j + \beta_k\right)z \right] + i\sum_k B_k \left(K_{kj}^T + K_{kj}^z \right)\exp\left[-i\left(\beta_j - \beta_k\right)z \right],$$

$$(2.29)$$

where $K_{kj}^T(z)$ is the transverse coupling coefficient between modes j and k, and $K_{kj}^z(z)$ is the longitudinal coupling coefficient. These are analogous coefficients but, in the particular case of guided modes in optical fibres, $K_{kj}^z(z) \ll K_{kj}^T(z)$. Thus, longitudinal coefficient is usually neglected. The transverse coefficient is given by

$$K_{kj}^T(z) = \frac{\omega}{4} \iint_\infty \Delta\varepsilon(x,y,z)\vec{e}_k^T(x,y)\vec{e}_j^{T*}(x,y)\,dxdy. \qquad (2.30)$$

Hence, equations (2.28) and (2.29) can be simplified as follows

$$\frac{dA_j}{dz} = -i\sum_k \left\{ A_k \exp\left[i\left(\beta_j - \beta_k\right)z\right] + B_k \exp\left[i\left(\beta_j + \beta_k\right)z\right] \right\} K_{kj}^T(z) \qquad (2.31)$$

and

$$\frac{dB_j}{dz} = i\sum_k \left\{ A_k \exp\left[-i\left(\beta_j + \beta_k\right)z\right] + B_k \exp\left[-i\left(\beta_j - \beta_k\right)z\right] \right\} K_{kj}^T(z) \qquad (2.32)$$

These equations are the differential coupled-mode equations that will be used to obtain the Bragg grating reflection spectrum.

2.4.3   Fibre Bragg Gratings

As already mentioned, fibre Bragg gratings are a spatial modulation of the fibre core refractive index amplitude. As seen in section 2.2, most of its writing techniques are based on the exposure of an optical fibre to a spatially varying pattern of ultraviolet intensity. The result is a perturbation to the effective refractive index n_{eff} of the guided mode of the optical fibre along the longitudinal axis. This variation, $n_{eff}(z)$, can be approximately described by a sinusoidal modulation profile which is a generalization of the dependence given by equation (2.18):

$$n_{eff}(z) = \overline{n_{eff}(z)}\left\{1 + V(z)\cos\left[\frac{2\pi}{\Lambda}z + \phi(z)\right]\right\}, \qquad (2.33)$$

where $\overline{n_{eff}(z)}$ is the *dc* index change spatially averaged over a grating period, $V(z)$ is the fringe visibility of the index modulation, Λ is the nominal grating period and $\phi(z)$ describes the grating chirp.

In Bragg gratings, the propagating modes $A(z)$ and counter-propagating modes $B(z)$ are identical, thus, coupling between these two guided modes originates a resonance wavelength. In wavelengths near such resonance peak, it is assumed that the

interactions which involve $\dfrac{dA_j}{dz}$ and $\dfrac{dB_j}{dz}$ may be simplified, by retaining only terms significant to the *synchronous approximation* [29]. Hence, neglecting terms that contain a rapidly oscillating z dependence (since these have a weak contribution in the growth and decay of the amplitudes), coupled-mode equations (2.31) and (2.32) can be written as follows:

$$\frac{dA_{01}}{dz} = -i\kappa B_{01}\exp\left(i2\Delta\beta z\right) \qquad (2.34)$$

and

$$\frac{dB_{01}}{dz} = i\kappa A_{01}\exp\left(-i2\Delta\beta z\right). \qquad (2.35)$$

The equation for dA_{01}/dz defines coupling between the LP_{01} mode in the propagation direction with amplitude A_{01} and the LP_{01} mode in the counter-propagation direction with amplitude B_{01}; equation dB_{01}/dz defines coupling between the LP_{01} mode in the counter-propagation direction with the mode in the propagation direction. The transverse coupling coefficient for the LP_{01} mode is defined as

$$\kappa(z) = \frac{\omega}{4}\iint\limits_{\infty}\Delta\varepsilon\left(x,y,z\right)\vec{e}_{01}^{\,T}\left(x,y\right)\vec{e}_{01}^{\,T*}\left(x,y\right)dxdy, \qquad (2.36)$$

where $\vec{e}_{01}^{\,T}\left(x,y\right)$ is the normalized transverse distribution for the LP_{01} mode and the parameter $\Delta\beta$ is given by

$$\Delta\beta = \frac{2\pi n_{eff}}{\lambda} - \frac{\pi}{\Lambda}. \qquad (2.37)$$

The resonance condition of fibre Bragg gratings occurs for a specific wavelength, called Bragg wavelength λ_B, when $\Delta\beta = 0$. The result is the familiar Bragg condition, $\lambda_B = 2n_{eff}\Lambda$, already predicted by the qualitative grating picture presented before. The parameter $\Delta\beta$ defines the mismatch between the propagating wavelength and the Bragg wavelength.

The physical problem of coupling between propagating and counter-propagating guided modes is, therefore, described by equations (2.34) and (2.35), and the respective coupling coefficient κ (equation 2.36).

Uniform Bragg gratings are diffraction gratings based on refractive index modulation in the core of an optical fibre with constant modulation period (Λ), which means that, from equation (2.33), $\phi(z) = 0$. This modulation is represented as a sinusoidal variation of constant amplitude, $V(z) = V$, along the core of the optical fibre (z direction), i.e.

$$n(z) = n_{co} + \Delta n \cos\left(\frac{2\pi}{\Lambda} z\right), \tag{2.38}$$

where $\Delta n = V n_{co}$ is the amplitude modulation of the refractive index of the core. In uniform Bragg gratings it is valid that $\Delta \varepsilon \approx 2n\Delta n_{eff}$ because, in general, $\Delta n_{eff} << n$. Furthermore, if the fibre has a step-index profile, it is found that $\Delta n_{eff} \approx \eta \Delta n$, where η is the confinement factor of the guided mode of interest – i.e., ratio of the optical power that propagates in the core with the total propagated power –. Thus, the coupling coefficient given by equation (2.36) will have the form

$$\kappa = \frac{\pi \Delta n}{\lambda} \eta. \tag{2.39}$$

The confinement factor η is the fraction of optical power guided in the core of the fibre. For LP_{01} mode, η can be determined from

$$\eta = \frac{b^2}{V^2}\left[1 - \frac{J_l^2\left(V\sqrt{1-b}\right)}{J_{l+1}\left(V\sqrt{1-b}\right)J_{l-1}\left(V\sqrt{1-b}\right)}\right], \tag{2.40}$$

with $l = 0$ (l is the azimuthal order of the mode). The effective index parameter b is defined as $b = \left(n_{eff}^2 - n_{cl}^2\right)/\left(n_{co}^2 - n_{cl}^2\right)$ with n_{cl} being the refractive index of the cladding. The b parameter is a solution to the dispersion relation [31]

$$V\sqrt{1-b}\,\frac{J_{l-1}\left(V\sqrt{1-b}\right)}{J_l\left(V\sqrt{1-b}\right)}=-V\sqrt{b}\,\frac{K_{l-1}\left(V\sqrt{b}\right)}{K_l\left(V\sqrt{b}\right)},\qquad(2.41)$$

where $V=\dfrac{2\pi}{\lambda}a\sqrt{n_{co}^2-n_{cl}^2}$ is the normalized frequency (a the core radius).

Equations (2.34) and (2.35) are, in this case, coupled first-order differential equations with constant coefficients, for which closed-form solutions can be found when appropriate boundary conditions are specified. In a uniform Bragg grating with length L it is assumed that the radiation amplitude of the forward-going wave incident from $z=0$ is $A_{01}(0)=1$ and that no backward-going wave exists for $z\geq L$ and so $B_{01}(L)=0$. The solution of the coupled first-order differential equations with these boundary conditions will be

$$A_{01}(z)=\frac{-\exp(i\Delta\beta z)}{\left[\Delta\beta\sinh(SL)-iS\cosh(SL)\right]}\left\{\Delta\beta\sinh\left[S(z-L)\right]+iS\Delta\beta conh\left[S(z-L)\right]\right\}$$

$$(2.42)$$

and

$$B_{01}(z)=\frac{k\exp(i\Delta\beta z)}{\left[\Delta\beta\sinh(SL)-iS\cosh(SL)\right]}\sinh\left[S(z-L)\right],\qquad(2.43)$$

where $S=\sqrt{k^2-\Delta\beta^2}$.

The amplitude reflection coefficient (ρ) of the Bragg grating and its reflectivity (R) can be easily determined from equations (2.42) and (2.43), being the result the following

$$\rho=\frac{B_{01}(z)}{A_{01}(z)}\bigg|_{z=0}=\frac{k\sinh(SL)}{\left[\Delta\beta\sinh(SL)-iS\cosh(SL)\right]}\qquad(2.44)$$

and

$$R=|\rho|^2=\frac{k^2\sinh^2(SL)}{\left[\Delta\beta^2\sinh^2(SL)+S^2\cosh^2(SL)\right]}.\qquad(2.45)$$

Maximum reflectivity occurs for the resonance condition when $\Delta\beta = 0$ and is given by

$$R_{\max} = \tanh^2(kL).$$ (2.46)

The reflection bandwidth, $\Delta\lambda$, for a uniform Bragg grating can be defined as that between the first zeros on either side of the maximum reflectivity position. From equation (2.20) it turns out that

$$\frac{\Delta\lambda}{\lambda_B} = \frac{2\Lambda}{\pi L}\sqrt{(kL)^2 + \pi^2}.$$ (2.47)

The spectral width of Bragg gratings depends essentially on the number of interaction planes in the grating, $N = \dfrac{L}{\Lambda}$. If N is larger or smaller, the reflection bandwidth will by narrower or broader, respectively, for a given value of κL.

There is also a general expression for the approximate full width at half-maximum (FWHM) of a grating [32] and is defined as

$$\Delta\lambda_{FWHM} \approx \lambda_B s \sqrt{\left(\frac{\Delta n}{2n_{co}}\right)^2 + \left(\frac{\Lambda}{L}\right)^2},$$ (2.48)

where the parameter s is associated with the efficiency of Bragg gratings. Strong gratings have $s \sim 1$ (maximum reflectivity around 100%) and weak gratings have $s \sim 0.5$. Once the amplitude modulation Δn of the refractive index is very small, the biggest contribution for $\Delta\lambda_{FWHM}$ is in the number of interaction planes, N.
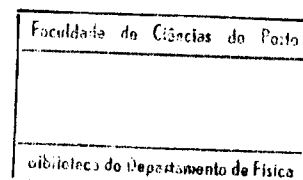
2.5   Apollo Simulation Software

To evaluate the effect of the several grating parameters on the characteristics of its spectral transfer function, the commercial software *Fibre Optical Grating Simulator* from *Apollo Photonics* was used.

Fibre Optical Grating Simulator for Bragg Grating (FOGS-BG) is a user-friendly computer-aided simulation and optimization tool for design and analysis of optical fibre devices based on Bragg grating. It can perform four types of tasks: simulation, parameter scanning, parameter extraction, and design optimization. Given grating structures, simulation gives the spectral properties of grating devices. Parameter scanning enables the optimization of grating performance by varying a parameter in a defined range. The design optimization further allows the variation of multiple parameters simultaneously to achieve the targeting performance that is initially defined. Parameter extraction can extract the grating information if the amplitude and the phase of the reflection spectrum have been specified.

FOGS serves the purpose of designing the gratings based in optical fibre, though it also can be used to design the gratings based on other waveguide. For that purpose, this software includes a fibre mode calculation module named *fibre optical mode solver (FOMS)* that calculates mode characteristics and then is read by *FOGS* in modal parameters. *FOMS* also simulates common fibre characteristics such as cut-off wavelength, dispersion curves and optical field distribution. It also provides the data processing of the overlap integral between fibre optical field and photosensitivity profile.

The key features of *FOGS* are the following:

- Calculation of fibre performance based on arbitrary radial index profile and material dispersion described by pre-defined functions, user-defined functions, tables and data files;

- Key fibre characteristics such as cut-off wavelength, dispersion curves and modal size parameters;

- Simulation and parameter scanning of grating structures with arbitrary chirp and apodization, and phase shift;

- Parameter extraction for grating structure given the amplitude and phase of the reflection spectrum;

- Simultaneously optimization of multiple grating parameters ti achieve the target spectrum performance;

- Multiple mode coupling and tilted grating.

This software also provides several examples of fibre grating design that can be adapted to a specific application. The next section presents the simulations of several grating structures obtained from *FOGS*.

2.5.1   Simulations of Specific Grating Structures

As already mentioned, *FOGS* is exclusively used for grating calculations including grating simulations, optimizations and parameter extraction while *FOMS* is the fibre mode calculator that can be used as a fibre design tool and as a part of fibre grating simulation. The results presented in this section are based on data imported from *FOMS*, namely the *SMF 28 Standard Fibre* example.

Uniform Fibre Bragg Gratings

For the uniform Bragg gratings simulation it was defined the parameters presented in the following tables:

Chirp Input	
Grating length (mm)	10
Grating shape	Sinusoidal
Predefined analytic function	Uniform
Grating period (nm)	535

Table 2.1 – Chirp input parameters.

Apodization Input		
Coefficient for DC index change due to apodization		0
AC index change:	*Predefined analytic function*	Uniform
	AC index change	10^{-5}

Table 2.2 – Apodization input parameters.

The DC index change specifies a constant responsible for the additional average index change caused by UV writing and the AC index change defines the amplitude of the photo-induced periodical refractive index change along the fibre. The phase-shift input was not used. The grating spectral profile was calculated for grating lengths of 10,

20 and 30 mm length, together with AC index changes (10^{-5} to 10^{-4}). Figure 2.10 shows the results.
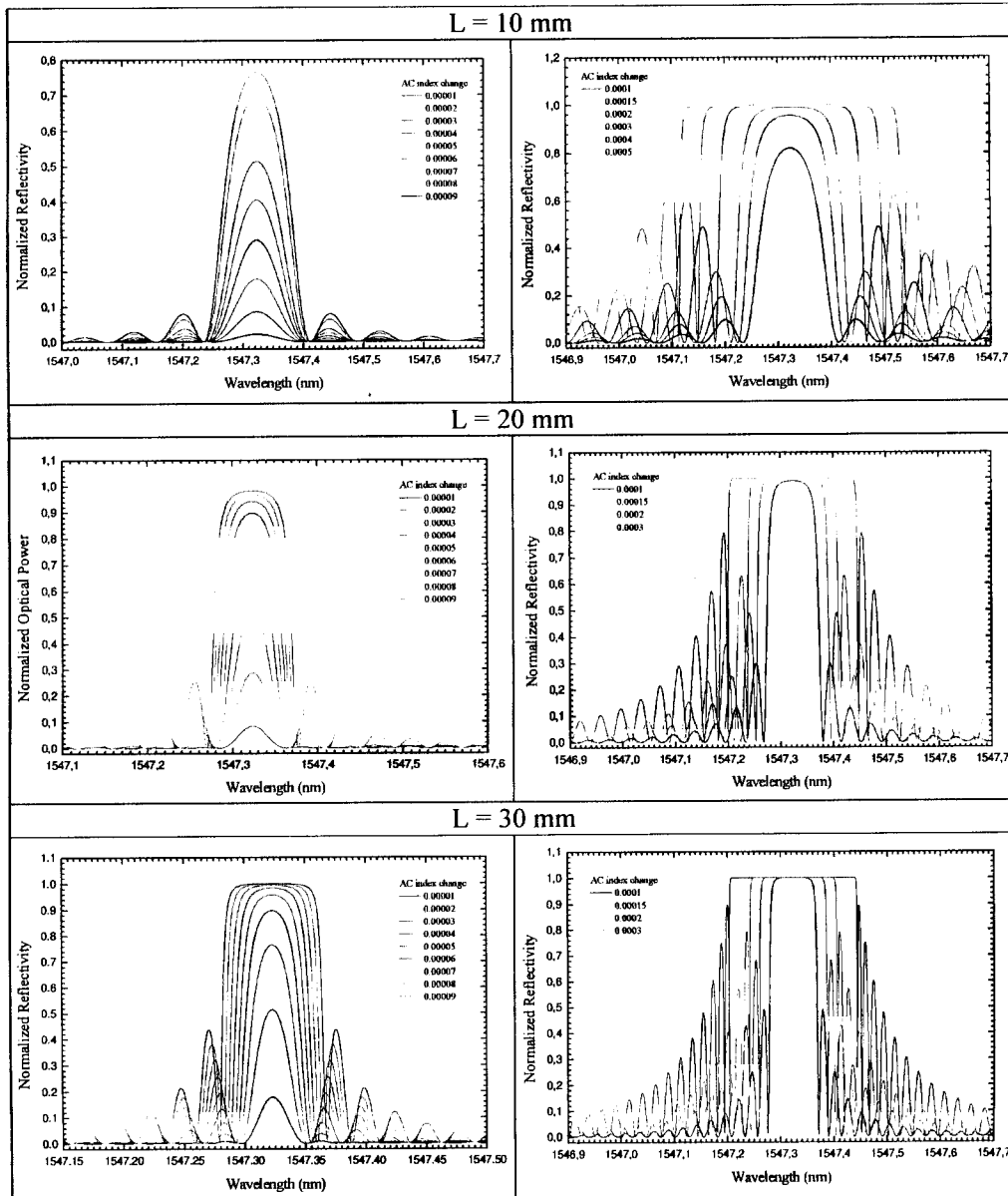
Figure 2.10 – Reflection spectrum of uniform Bragg gratings with lengths of 10mm, 20 mm and 30 mm, for different refractive index modulation indices.

These results show that refractive index changes around 10^{-4} allow spectral responses with widths lower than 100 pm and 100% reflectivity to be obtainable. It can be observed that, for the same grating length, both reflectivity and FWHM increase with

the increase of the modulation index. As expected, these results agree with equations (2.46) and (2.48). Figure 2.11 shows that, for the same modulation index, the FWHM width decreases with the increase of the grating length.
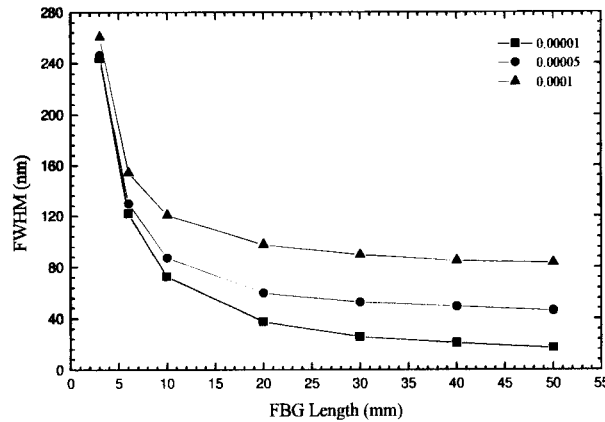

Figure 2.11 – FWHM dependence on FBG length.

These basic simulation results support the feasibility of using fibre Bragg gratings to develop narrow bandpass filters with characteristics adequate for sensing and in fibre filtering applications.

2.6   Equivalent Circuit of Bragg Gratings

The spectral behavior of fibre Bragg gratings is normally derived from an electromagnetic analysis based on the coupled-mode theory [33]. Bragg gratings imprinted on many optical waveguides are more complex to treat, and numerical methods such as the beam-propagation method [34], the finite-difference time-domain method [35, 36], and the mode-matching method [37] are usually employed. These techniques can be highly accurate but also extremely time and memory consuming, especially if three-dimensional structures are considered. In any case, an electromagnetic approach is rarely useful for the synthesis of the grating and of more complex circuits containing Bragg gratings. Nevertheless, the matrix approach model permits the calculation of the spectral transmission of more realistic grating structures. A simple and exact analysis was proposed by Melloni *et al.* [38] that uses a coupled-mode theory combined with a matrix method in order to derive the equivalent circuit of symmetrical Bragg gratings. This model transforms the complex physical behavior of

the electromagnetic field into a simple equivalent circuit described by port-based parameters. The considered equivalent circuit is exact, is valid at every wavelength, and presents several advantages with respect to other possible equivalent circuits. It is very simple, being composed of an ideal partially reflecting mirror placed between two sections of dispersive propagating regions, especially with use of a simple and practical first-order approximation that is valid around the Bragg wavelength. In other hand, with this model, it becomes clear that the apparent reflection starts from the center of the grating structure.

In this model, it is considered a symmetrical uniform Bragg grating with a constant period Λ, a physical length L, and a refractive-index modulation $\delta n(z)$ symmetrical with respect to the center of the structure. The index modulation is superimposed on the effective refractive index $n_{eff}(\lambda)$ of the guiding medium, which can be an optical fibre, a dielectric waveguide, or even a bulk material. The effective refractive index is assumed wavelength dependent with the simple law

$$n_{eff}(z) = \overline{n_{eff}}\left(1 + a\frac{\lambda - \lambda_B}{\lambda_B}\right) \qquad (2.49)$$

where $\overline{n_{eff}}$ is the mean refractive index at the Bragg wavelength λ_B and a is the linear coefficient of dispersion. In general, the wavelength linear dependence is sufficient, but higher-order terms can be easily included.

A Bragg grating is symmetrical if $n_{eff}(z) = n_{eff}(L-z)$, where z is the abscissa defined as in Figure 2.12(a).
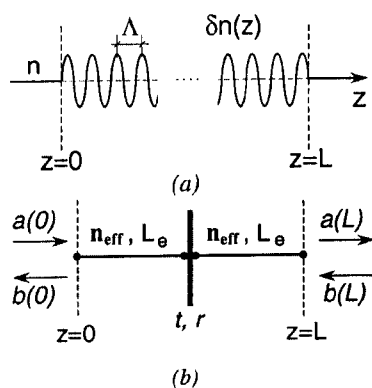

Figure 2.12 – (a) Symmetrical Bragg grating and (b) its equivalent circuit. [38]

The modulation of the refractive index is given by the following expression

$$\partial n(z) = \partial n_o \sin\left(\frac{2\pi}{\Lambda} z\right)$$
(2.50)

where it is assumed that $\partial n(z = 0) = 0$. However, there are situations in the fabrication process that originate an initial phase ϕ at the beginning of the modulation index such that $\partial n(z = 0) = \partial n_o \sin \phi$. This phase is conventionally defined [39] as the phase of the grating in $z = 0$, as shown in Figure 2.13, where $\phi = 2\pi s / \Lambda$.
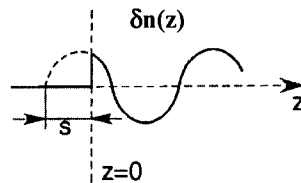

Figure 2.13 – Definition of the initial phase of the grating.[38]

Due to that, equation (2.50) gets the form

$$\partial n(z) = \partial n_o \sin\left(\frac{2\pi}{\Lambda} z + \phi\right)$$
(2.51)

The physical length L and the period Λ are related by

$$L = \left(m + \frac{1}{2} - \frac{\phi}{\pi}\right)\Lambda$$
(2.52)

where m is the integer number of periods contained in the grating with $\phi = 0$ (first diffraction order).

In the following it is demonstrated that the uniform symmetrical gratings are equivalent to the circuit shown in Figure 2.12(b). This is not the only possible equivalent circuit, but it is very simple and is suitable for the synthesis of more complex circuits. The equivalent circuit is composed of a partially reflecting mirror placed between two uniform sections of length L_e and refractive index n_{eff}. The equivalent

length L_e and the reflectivity r are wavelength dependent and may be determined by equating the transmission matrix $\mathbf{T_e}$ of the equivalent circuit to the transmission matrix $\mathbf{T_g}$ of the grating. The transmission matrix $\mathbf{T_e}$ of the equivalent circuit is obtained by cascading the transmission matrices of the two sections L_e to that of the partial reflector. To this end it is assumed, without loss of generality [40], that the field reflectivity r of the mirror is real positive. In this hypothesis, the field transmissivity, *it*, is pure imaginary, since a dephasing of $\pm \pi / 2$ between the transmitted and the reflected fields is required for a lossless symmetrical reflector. The matrix $\mathbf{T_e}$ relates the complex amplitude of the waves at the right of the circuit to those at the left as

$$\begin{pmatrix} a(0) \\ b(0) \end{pmatrix} = \begin{bmatrix} \mathbf{T_e}(1,1) & \mathbf{T_e}(1,2) \\ \mathbf{T_e}(2,1) & \mathbf{T_e}(2,2) \end{bmatrix} \begin{bmatrix} a(\mathbf{L}) \\ b(\mathbf{L}) \end{bmatrix} = \mathbf{T_e} \begin{pmatrix} a(\mathbf{L}) \\ b(\mathbf{L}) \end{pmatrix} \tag{2.53}$$

whose coefficients are

$$\mathbf{T_e}(1,1) = \mathbf{T_e^*}(2,2) = -\frac{i}{t} e^{-i2\varphi_e} \tag{2.54}$$

$$\mathbf{T_e}(1,2) = \mathbf{T_e^*}(2,1) = \frac{i}{t} r \tag{2.55}$$

and the phase term φ_e is defined as

$$\varphi_e = \frac{2\pi}{\lambda} n_{eff} \mathbf{L_e} \tag{2.56}$$

The transmission matrix $\mathbf{T_g}$ of a uniform grating is obtained from the coupled-wave equations. With the use of the same convention as in Figure 2.12(a) and equation (2.53), the complex amplitude of the waves at the input and the output of the grating are related by the transmission matrix $\mathbf{T_g}$ as

$$\begin{pmatrix} a(0) \\ b(0) \end{pmatrix} = \begin{bmatrix} \mathbf{T_g}(1,1) & \mathbf{T_g}(1,2) \\ \mathbf{T_g}(2,1) & \mathbf{T_g}(2,2) \end{bmatrix} \begin{bmatrix} a(\mathbf{L}) \\ b(\mathbf{L}) \end{bmatrix} = \mathbf{T_g} \begin{pmatrix} a(\mathbf{L}) \\ b(\mathbf{L}) \end{pmatrix} \tag{2.57}$$

whose coefficients are

$$\mathbf{T_g}(1,1) = \mathbf{T_g^*}(2,2) = \left[\cosh(SL) + i\frac{\Delta\beta}{S}\sinh(SL)\right]e^{i\frac{\pi L}{\Lambda}} \qquad (2.58)$$

$$\mathbf{T_g}(1,2) = \mathbf{T_g^*}(2,1) = -\frac{k}{S}\sinh(SL)e^{-i\left(\frac{\pi L}{\Lambda}+\phi\right)} \qquad (2.59)$$

where the coupling coefficient k of grating, the detuning $\Delta\beta$, and S are defined as

$$k = \frac{\delta n\pi}{\lambda} \qquad (2.60)$$

$$\Delta\beta = \frac{2\pi}{\lambda}n - \frac{\pi}{\Lambda} \qquad (2.61)$$

$$S^2 = k^2 - \Delta\beta^2 \qquad (2.62)$$

The expressions of r and t of the equivalent circuit partial reflector are obtained by equating the modulus of the elements of the matrix $\mathbf{T_e}$

$$\left|\mathbf{T_e}(1,1)\right| = \left|\mathbf{T_e}(2,2)\right| = \frac{1}{|t|} \qquad (2.63)$$

$$\left|\mathbf{T_e}(1,2)\right| = \left|\mathbf{T_e}(2,1)\right| = \frac{r}{|t|} \qquad (2.64)$$

to those of the matrix $\mathbf{T_g}$ and, clearly, correspond to the modulus of the field reflectivity and transmissivity of the grating. In the case of uniform gratings, the following analytical expressions are found,

$$r = \frac{\left|\mathbf{T_e}(1,2)\right|}{\left|\mathbf{T_e}(1,1)\right|} = \frac{\left|\mathbf{T_g}(1,2)\right|}{\left|\mathbf{T_g}(1,1)\right|} = \frac{k\sinh(SL)}{\left[S^2\cosh^2(SL) + \Delta\beta^2\sinh^2(SL)\right]^{1/2}} \qquad (2.65)$$

$$|t| = \frac{1}{|T_e(1,1)|} = \frac{1}{|T_g(1,1)|} = \frac{S}{\left[S^2 \cosh^2(SL) + \Delta\beta^2 \sinh^2(SL) \right]^{1/2}} \qquad (2.66)$$

The sign of t must be chosen according to the grating length. By equating the phase of the element $T_e(2,1)$ to the phase of $T_g(2,1)$ and taking into account the symmetry condition given by equation (2.52), it is found that when the integer number of grating periods m is even, t is positive and when m is odd, t is negative. Finally, by equating the phase of $T_e(1,1)$ to the phase of $T_g(1,1)$, one obtains the equivalent length L_e,

$$L_e = \frac{\lambda}{\lambda_B} \left[\frac{L}{2} \pm \frac{\Lambda}{4} + \frac{\Lambda}{2\pi} \tan^{-1}\left(\frac{\Delta\beta}{S} \tanh(SL) \right) \right] \qquad (2.67)$$

where the sign to consider is the sign of t. Note that the two wavelength-dependent sections L_e introduce a dispersion even if $a = 0$. In equation (2.67), $\tan^{-1}$ means the four quadrant inverse tangent, defined between $-\pi$ and π.

The equivalent circuit proposed in Figure 2.12(b), with the reflectivity given by the equation (2.65) and L_e given by equation (2.67), is rigorous and is identical to the corresponding grating at *every wavelength*. However, in both the analysis and the design of optical circuits containing Bragg gratings it is more practical to consider a first-order approximation of L_e around the Bragg wavelength λ_B,

$$L_e = L_{eB} + \Delta L_e \frac{\lambda - \lambda_B}{\lambda_B} \qquad (2.68)$$

where, from equation (2.67),

$$L_{eB} = \frac{L}{2} \pm \frac{\Lambda}{4} \qquad (2.69)$$

is the equivalent length at the Bragg wavelength and ΔL_e is the slope of the equivalent length at λ_B. In the simple case of a uniform grating, ΔL_e is given by

$$\Delta L_e = L_{eB} - \frac{r_M}{2k}(1-a) \qquad (2.70)$$

where k is the grating coupling coefficient evaluated at λ_B, and $r_M = \tanh(kL)$ is the maximum field reflectivity.

In this analysis, the length of the sections L_e increases indefinitely with the physical length of the grating; this may sound like a paradox because it seems that the reflection takes place always in the middle of the grating. However, the length L_e is the phase length, whereas the penetration depth – that is, the space the light propagates in the grating before being reflected – is the group length L_p. The group length at λ_B, obtained from equation (2.67), defines the real reflection point of the light, and, for a uniform grating, it is equal to

$$L_p = \frac{r_M}{2k}(1-a)\qquad\qquad(2.71)$$

where for strong gratings, L_p is independent of the physical length of the grating itself.

In conclusion, the equivalent length L_e increases with the wavelength and at λ_B is equal to one half the physical length of the grating except for a $\pm \Lambda/4$ term. The dispersive nature of L_e and the additional $\Lambda/4$ term are ineffective if the grating is used as a simple reflector, but they play a fundamental role in optical circuits and devices that use, for example, Bragg gratings based Fabry-Perot cavities [38].

2.7   Sensing Properties of Fibre Bragg Gratings

Most of the work on fibre Bragg grating sensors has focused on the use of these devices for providing quasi-distributed point sensing of strain or temperature. Any change in fibre properties, such as strain, temperature or polarization which varies the effective index or the grating period, will change the Bragg wavelength.

The thermal response of a fibre Bragg grating arises due to the inherent thermal expansion of the fibre material and the temperature dependence of the refractive index. For a temperature change of ΔT, the corresponding wavelength shift, $\Delta\lambda_B$, is:

$$\Delta\lambda_B = \lambda_B(\alpha + \xi)\Delta T\qquad\qquad(2.72)$$

where $\alpha = \dfrac{1}{\Lambda} \dfrac{\partial \Lambda}{\partial T}$ is the thermal expansion coefficient and $\xi = \dfrac{1}{n_{ef}} \dfrac{\partial n_{ef}}{\partial T}$ is the fibre

thermo-optic coefficient. For the case of silica fibre doped with germanium, $\alpha \approx 0.55 \times 10^{-6} K^{-1}$ and $\xi \approx 8.6 \times 10^{-6} K^{-1}$. This means that, for temperature variations, the Bragg wavelength shift is essentially caused by the change of the effective index. Experimental results of a fibre Bragg grating around 1550 nm submitted to temperature are shown in Figure 2.14.
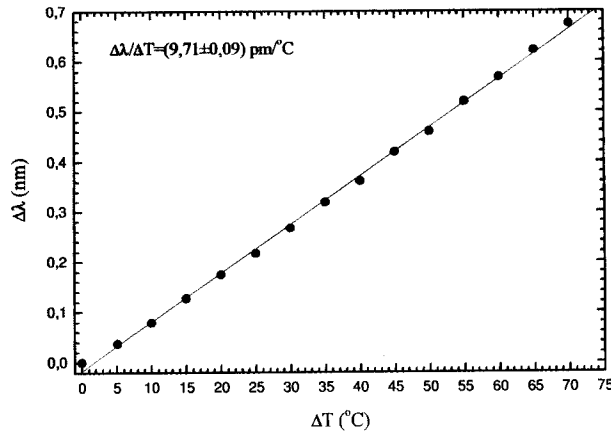

Figure 2.14 – Bragg wavelength shift versus temperature variation.

According to equation (2.71), $\Delta \lambda_B$ varies linearly with ΔT and increases with increasing values of temperature. The sensitivity to this physical parameter at this wavelength is $(9.71 \pm 0.09) pm /^{\circ} C$.

The strain response of a fibre Bragg grating arises due to both the physical elongation of the fibre (and corresponding fractional change in grating pitch), and the change in fibre refractive index due to photoelastic effects. The wavelength shift, $\Delta \lambda_B$, for an applied longitudinal strain, $\Delta \varepsilon = \dfrac{\Delta L}{L}$, is given by

$$\Delta \lambda_B = \lambda_B (1 - p_e) \Delta \varepsilon \qquad (2.73)$$

where p_e is the photoelastic coefficient of the fibre, given by

$$p_e = \frac{1}{n}\frac{\partial n}{\partial \varepsilon} = \frac{n_{ef}^2}{2}\left[p_{12} - v(p_{11} + p_{12})\right] \qquad (2.74)$$

where p_{11} and p_{12} are the components of the fibre-optic strain tensor and v is Poisson's ration. Typical values for silica fibres doped with germanium are $p_{11} \approx 0.113$, $p_{12} \approx 0.252$, $v \approx 0.16$ and $n_{ef} \approx 1.482$. Experimental results of a fibre Bragg grating around 1550 nm submitted to longitudinal strain are shown in Figure 2.15.
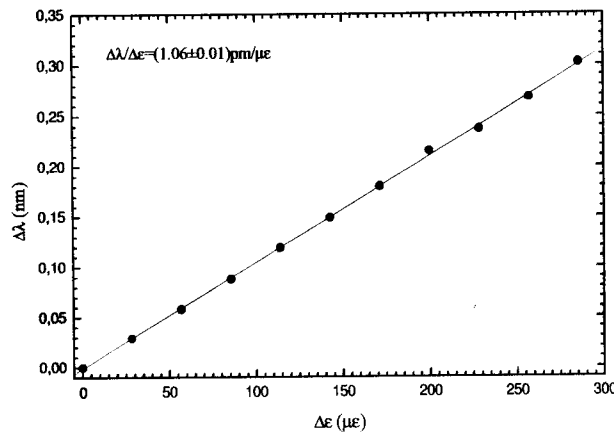

Figure 2.15 – Bragg wavelength shift versus longitudinal strain.

According to equation (2.72), $\Delta\lambda_B$ varies linearly with $\Delta\varepsilon$, and increases with increasing values of strain. The sensitivity to this physical parameter at this wavelength is $(1.06 \pm 0.01)pm/\mu\varepsilon$.

Fibre Bragg gratings are inherently sensitive to strain and temperature. However, by proper interfacing these devices can be tailored to measure virtually all physical parameters and even others (with particular emphasis in the biochemical field).

3

Phase-Shifted Fibre Bragg Gratings

Fibre Bragg gratings are very good optical filters and they exhibit many different spectral responses depending on their refractive index modulation profile. Fibre Bragg gratings can be classified according to this modulation of the induced index change along the fibre axis: apodized, chirped, phase-shifted and sampled structures are some examples of the different types of Bragg gratings. This section will be focused on a particular type of fibre Bragg grating: *the phase-shifted Bragg grating*. First, the general properties of phase-shifted gratings will be presented; then, two other types of transmitting filters based on Bragg gratings, namely, Moiré Bragg gratings and chirped Bragg gratings with a discontinuity, are briefly described. Also, an overview of the fabrication techniques of phase-shifted Bragg gratings will be presented and reported the main characteristics of the devices fabricated in-house.

3.1   Introduction

Most fibre gratings designed for practical applications are nonuniform gratings. Often the main reason for choosing a nonuniform design is to reduce the undesirable side lobes prevalent in uniform-grating spectra. To achieve that, several apodization techniques can be used, as already addressed in section 2.3.2. Besides spectral response apodization, there are many other reasons to adjust the optical properties of fibre gratings by tailoring the grating parameters along the fibre axis. Sharp, well defined filter shapes are rapidly becoming critical characteristics for passive components in dense wavelength division multiplexed (DWDM) communications systems. On the other hand, chirping the period of a grating enables the dispersive properties of the scattered light to be tailored [41]. Sometimes it is desirable to create discrete, localized phase shifts in an otherwise periodic grating. Discrete phase shifts can be used to open

an extremely narrow transmission resonance in a reflection grating or to tailor the passive filter shape.

The principle of the phase shift was demonstrated by Alfemess *et al.* [42] in periodic structures made from semiconductor materials, where a phase shift was introduced by etching a space at the center of the device. This forms the basis of the single-mode phase-shifted semiconductor DFB laser [43]. A similar device may be constructed in optical fibres using various techniques that will be described in the next section. Such processing produces two gratings out of phase with each other, which acts as a wavelength-selective Fabry-Perot resonator. The resonant wavelength corresponds to a transmitting filter over the rejection band of the Bragg grating and depends on the amplitude and location of the phase change.
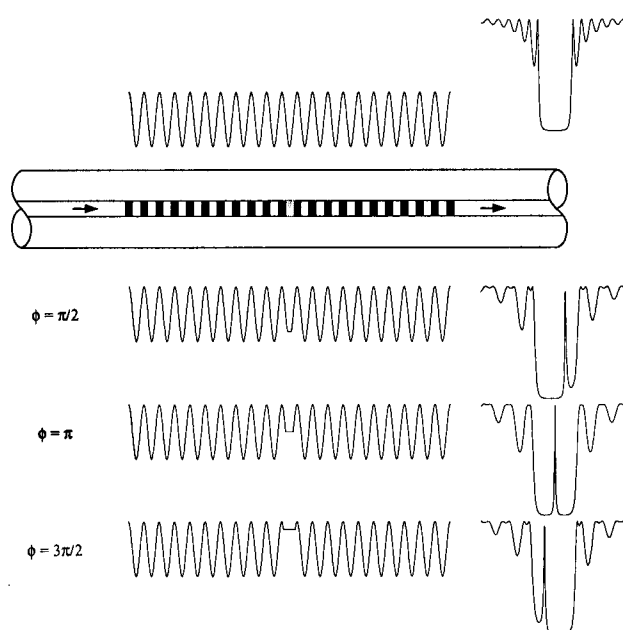
Figure 3.1 – Principle of operation of Bragg gratings with a phase shift in the middle of the grating length.[22]

The resonant wavelength of this filter can be tuned over the spectral response of the Bragg grating by introducing one or several phase shifts within the range [0-2π] in particular locations along the grating length [44]. This technique allows the exploitation of Bragg gratings spectral response in transmission that can be used for specific applications, namely, channel tuning in communication systems.

3.2   Bragg Gratings with Transmitting Spectral Windows

Fibre Bragg gratings with transmitting windows in the spectral response are of three types, namely: phase-shifted Bragg gratings, Moiré Bragg gratings and chirped Bragg gratings with a discontinuity.

As illustrated in Figure 3.1, phase-shifted Bragg gratings are characterized by a phase change in the refractive index modulation at a specific location in the length of the grating.

Moiré Bragg gratings are based on sequential UV exposure of the same section of optical fibre to interference patterns with slightly different periods, Λ_1 and Λ_2. The beating between these two similar frequencies produces a spatial modulation of the refractive index along the optical fibre, which varies quickly with short period $\Lambda_s = 2\Lambda_1\Lambda_2/(\Lambda_1 + \Lambda_2)$ and, at the top, has a sinusoidal envelope with longer period $\Lambda_l = 2\Lambda_1\Lambda_2/(\Lambda_1 - \Lambda_2)$. When the envelope goes through zero the phase of the short period sinusoidal modulation changes by π, originating a narrow transmitting pass-band in the spectral response of the grating with period Λ_s (Figure 3.2).
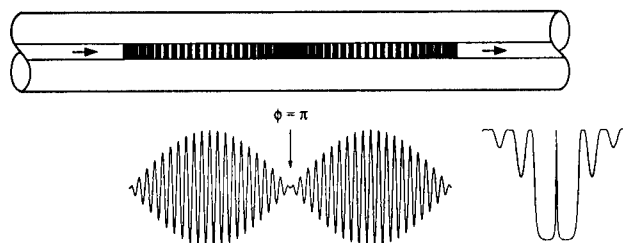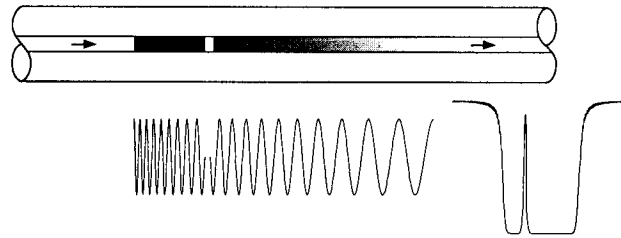

Figure 3.2 – Principle of operation of Moiré Bragg gratings. [22]

Transmition filters can also be fabricated in chirped gratings by inducing a discontinuity in the grating during its fabrication or by postprocessing. Similarly to what happens with standard phase-shifted Bragg gratings, the technique is based in a suppression of a particular section of the chirped grating and, thus, forming a discontinuity in the refractive index modulation. The principle of operation of this type of filters is illustrated in Figure 3.3.

Figure 3.3 – Principle of operation of chirped Bragg gratings with a discontinuity. [22]

3.3   Fabrication Techniques of Phase-Shifted Bragg Gratings

Phase-shifted Bragg gratings may be fabricated in optical fibres using various techniques, which are refinements of those utilized for the fabrication of standard FBGs. Some of the most common techniques are based on post-processing of gratings in a specific region of their length, on the utilization of phase masks with phase-shifted regions incorporated, and on application of the moving fibre/phase mask scanning beam procedure.

In the first reference to the post-processing technique [45], a uniform Bragg grating with 4 centimeters long and 99% reflectivity was initially fabricated. The filter was then formed by UV exposure of 1 millimeter in the central region of the grating, photoinducing an index change of $\sim 4\text{x}10^{-4}$, which corresponds to a deviation of $\sim \lambda/4$. In a similar way, phase-shifted gratings can be achieved by post-fabrication thermal processing using localized heat, either by using the Peltier effect [46] or an electric arc from a fusion splicer [47]. It is also possible to reproduce the phase-shift behavior with special supports that allow controlling the strain level along a uniform Bragg grating [48]. In what concerns the second mentioned technique, reflection grating devices with internal band-pass structures were obtained using a phase mask with a single $\pi/4$ phase shift in the middle of the field [49].

The third technique is eventually the most simple where no restriction to the grating structure is imposed by the use of a uniform phase mask. To put in a phase-shift at a certain position along the grating, the optical fibre is moved by the appropriate fraction of the grating pitch when the writing beam is being scanned along the uniform phase mask over that specific position [26]. The optical fibre is mounted on a computer-

controlled piezoelectric (PZT) stage to induce the movement that will produce the phase-shift. The same approach can be applied to the phase mask by dithering or simple displacement, thus creating the phase shift in the writing process of the grating [50].

Lloyd's mirrors [51] and holographic interferometers [52, 53] are examples of other fabrication techniques, different from the ones presented previously. An interesting one is based on polarization control of the UV radiation during the writing of phase-shifted Bragg gratings [54]. This method is based on a π phase shift between the refractive index modulation profiles induced by the two states of polarization of UV light. By changing the ratio of UV intensity in the two polarizations it is possible to control the modulation strength and to induce phase shifts, while keeping a constant effective refractive index throughout the Bragg grating.

Moreover, it can be considered the introduction of multiple phase shifts [55, 56] for complex filtering implementation with more uniform spectral responses.

3.4   Theoretical Analysis of Phase-Shifted Bragg Gratings

Several authors have proposed different solutions for determining the theoretical spectral characteristics of a phase-shifted Bragg grating. Following the general approach to study standard FBGs, the most common is based on the matrix approach and it was presented by Yamada and Sakuda [39]. In the case of a phase-shifted Bragg grating the calculus is simple, because it is considered merely the multiplication of the two matrices relative to the two phase-shifted parts of the grating.

Other authors have proposed methods to characterize phase-shifted Bragg gratings spectral characteristics. Those authors generally used the Jones matrix formalism by introducing a diagonal matrix with elements $\exp(\pm i\phi_j)$, where ϕ_j is the phase shift [44]. This approach considers the case of a cavity that has induced a total return phase-shift value of $2\phi_j$ in the wave propagation. Hence, the value of the phase shift for a π phase-shifted grating is presented as $\phi_j = \pi/2$.

Any of these approaches is able to provide an analytical expression for the transmission spectrum of phase-shifted Bragg gratings. This expression was first demonstrated by Martinez and Ferdinand [57], where coupling equations were developed with the parameters allowed by the phase mask, namely, the grating index

modulation Δn, the phase shift in the grating $\Delta\phi$, the lengths l_1 and l_2 of the two phase-shifted parts of the gratings, the total length L of the grating and its modulation period Λ. In what follows the notation used will closely match the one used by those authors.

Again, it is convenient to consider that the refractive index modulation of the grating can be represented as a sinusoidal variation of constant amplitude along the core of the optical fibre, i.e.

$$n(z) = n_{co} + \Delta n \cos\left(\frac{2\pi}{\Lambda}z + \phi(z)\right),$$ (3.1)

where the symbols have the meaning indicated in section 2.4: $\phi(z)$ describes the grating chirp, n_{co} and Δn are the core's refractive index and its amplitude modulation, respectively. For the phase change to occur, the refractive index modulation will obey the following conditions:

$$\begin{cases} \phi(z) = 0 & \text{if} \quad 0 \le z < z_1 \\ \phi(z) = \Delta\phi & \text{if} \quad z_1 \le z \le z_2 \end{cases}.$$ (3.2)

In the analysis it is considered an optical fibre with two counter-propagating waves, A_i and B_i, of wavelength λ propagating through the grating, where $i = 1,2$ depending on the part of the grating (Figure 3.4).
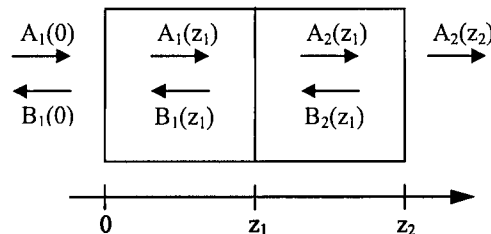

Figure 3.4 – Coupling between the two counter-propagating waves in the phase-shifted grating.

The refractive index modulation acts as a perturbation in the propagation such that coupling between the two waves occurs in the vicinity of the Bragg wavelength λ_B. As

already been seen in section 2.4, this phenomenon can be expressed by coupled differential equations (equations 2.34 and 2.35)

$$\frac{dA_i}{dz} = -i\kappa B_i \exp\left\{i\left[2\Delta\beta z + \phi(z)\right]\right\}, \tag{3.3}$$

and

$$\frac{dB_i}{dz} = i\kappa A_i \exp\left\{-i\left[2\Delta\beta z + \phi(z)\right]\right\}, \tag{3.4}$$

where in this case it is added the parameter $\phi(z)$ in order to introduce the phase change. Again, the coupling coefficient, κ, for the sinusoidal variation of the index perturbation along the fibre axis is given by $\kappa = \pi\Delta n\eta / \lambda$ (η is confinement factor of the guided mode) and the detuning parameter r $\Delta\beta = \beta - \pi / \lambda$ is the difference between the propagation constant $\beta = 2\pi n_{co} / \lambda$ and the wave vector $K = 2\pi / \Lambda$ of the grating.

Equations (3.3) and (3.4) yield the following equation which is valid in both parts of the grating

$$\frac{\partial^2 B_i}{\partial^2 z} - i\left[2\Delta\beta + \frac{d\phi(z)}{dz}\right]\frac{\partial B_i}{\partial z} - \kappa^2 B_i = 0 \tag{3.5}$$

Case 1: in part $1 \rightarrow \phi(z) = 0$

$$\frac{\partial^2 B_1}{\partial^2 z} - i2\Delta\beta\frac{\partial B_1}{\partial z} - \kappa^2 B_1 = 0 \tag{3.6}$$

and

$$A_1 = -\frac{i}{\kappa}\frac{\partial B_1}{\partial z}\exp\left[i(2\Delta\beta z)\right]. \tag{3.7}$$

Case 2: in part $2 \rightarrow \phi(z) = \Delta\phi$

$$\frac{\partial^2 B_2}{\partial^2 z} - i2\Delta\beta\frac{\partial B_2}{\partial z} - \kappa^2 B_2 = 0 \tag{3.8}$$

and

$$A_2 = -\frac{i}{\kappa}\frac{\partial B_2}{\partial z}\exp\left[i(2\Delta\beta z - \Delta\phi)\right]. \tag{3.9}$$

To solve these equations it has to be considered the following boundary conditions:

$$A_1(0) = 1, \qquad A_1(z_1) = A_2(z_1) \qquad\qquad (3.10)$$

and

$$B_2(z_2) = 0, \qquad B_1(z_1) = B_2(z_1), \qquad\qquad (3.11)$$

resulting into the following expressions

$$B_2(z) = C\exp(\Gamma_1 z) + D\exp(\Gamma_2 z) \qquad\qquad (3.12)$$

and

$$A_2(z) = \left| -\frac{C}{\kappa}\Gamma_1 \exp(\Gamma_1 z) - \frac{D}{\kappa}\Gamma_2 \exp(\Gamma_2 z) \right| \exp[i(2\Delta\beta z - \Delta\phi)], \qquad\qquad (3.13)$$

where $\Gamma_1 = i\Delta\beta - \gamma$, $\Gamma_2 = i\Delta\beta + \gamma$ and $\gamma^2 = \kappa^2 - \Delta\beta^2$. The constants C and D can be determined by taking into account the boundary conditions.

The purpose of this analysis is to determine the grating's total transmission T for a given wavelength:

$$T = \left| \frac{A_2(z_2)}{A_1(0)} \right|^2 = |A_2(z_2)|^2. \qquad\qquad (3.14)$$

Then, using equation (3.13), the transmission will be given by

$$T = \frac{1}{\kappa^2}|\Gamma_1 C\exp(\Gamma_1 z_2) + \Gamma_2 D\exp(\Gamma_2 z_2)|^2 \qquad\qquad (3.15)$$

Finally, after the determination of the constants C and D, the analytical expression for the grating transmission is:

$$T(\lambda) = \frac{\gamma^4}{\Gamma^2 + (E - \Gamma)\{E - \Gamma[1 - 2\cos(\Delta\phi)]\} + F[F - 2\Gamma\sin(\Delta\phi)]} \qquad\qquad (3.16)$$

with

$$\Gamma = \kappa^2 \sinh\left(\gamma l_1\right) \sinh\left(\gamma l_2\right), \qquad \gamma^2 = \kappa^2 - \Delta\beta^2$$

$$E = \gamma^2 \cosh\left(\gamma L\right), \qquad\qquad F = \Delta\beta\gamma \sinh\left(\gamma L\right) \qquad (3.17)$$

$$\Delta\beta = \beta - \pi / \lambda, \qquad\qquad \kappa = \pi\Delta n\eta / \lambda$$

Equation (3.16) permits a theoretical interpretation of various situations of interest in the context of phase-shifted Bragg gratings.

Situation 1: $\Delta\phi = 0$

It can be verified that, for $\Delta\phi = 0$, equation (3.16) gives the classical expression for the spectral transmission of a uniform Bragg grating [10]:
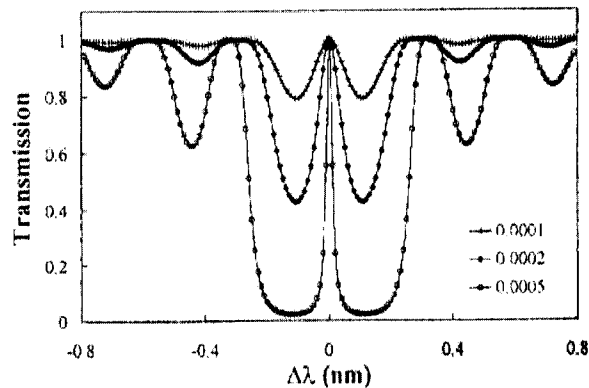
$$T(\lambda) = \frac{\kappa^2 - \Delta\beta^2}{\kappa^2 \cosh^2(\gamma L) - \Delta\beta^2}. \qquad (3.18)$$

Situation 2: $\Delta\phi = \pi$ and $l_1 = l_2$

In this case the transmission of the grating is given by:

$$T(\lambda) = \frac{\gamma^4}{\Delta\beta^2 \left[\Delta\beta^2 \cosh^2\left(\gamma L\right) + \gamma^2 \sinh^2\left(\gamma L\right) - 2\kappa^2 \cosh\left(\gamma L\right) + \kappa^4\right]}. \qquad (3.19)$$

The phase-shifted Bragg grating spectrum is plotted in Figure 3.5 for three values of the refractive index modulation depth, Δn [57].

Figure 3.5 – Spectral transmission of a π-shifted Bragg grating with $l_1 = l_2 =$ 2mm for three values of Δn. [57]

The transmission notch is centered on the Bragg wavelength. As Δn increases, the bandwidth of the reflected band increases and the bandwidth of the transmission notch decreases. This is an important practical feature considering that for a fixed phase mask, the major degree of freedom is precisely the refractive index modulation amplitude Δn, which can be adjusted between a certain interval by modifying the UV exposure time.

Situation 3: $\Delta\phi$ *undetermined and* $l_1 = l_2$

In this case the value of the transmission in the center of the notch is equal to 1 and its spectral position depends on the value of $\Delta\phi$.

Situation 4: $\Delta\phi = \pi$ *and* $l_1 \neq l_2$

Now the value of the transmission notch is not equal to 1, but it is centered at the Bragg wavelength and has the value (from equation 3.16)

$$T(\lambda_B) = \frac{1}{\cosh^2\left[\kappa(l_1 - l_2)\right]}.$$

$$(3.20)$$

For a specific Δn the bandwidths of the reflection band and the transmission notch change in the same direction – i.e., when one increases the same happens to the other and vice-versa –. However, the same does not happen when the variable parameter is Δn, as illustrated in Figure 3.5. In the context of optical filtering, it is important to have a bandwidth for the reflection band of several nanometers and to achieve it is necessary to consider chirped phase-shifted fibre Bragg gratings, situation in which the above theoretical results do not apply, being anyway valid the main concepts that grounds them. These concepts and numerical simulations that follows indicate that it is possible, with chirped phase-shifted fibre Bragg gratings with a relatively large Δn, to have devices with characteristics of ultra-narrow optical fibre filters. In chapter 6 this topic will be addressed further in detail.

3.5   Simulation Results

As already mentioned in previous chapter, to evaluate the effect of the several grating parameters on the characteristics of its spectral transfer function, the commercial

software *Fibre Optical Grating Simulator* from *Apollo Photonics* was used. The results presented in this section are based on data imported from *FOMS*, namely the *SMF 28 Standard Fibre* example.

Phase-Shift Fibre Bragg Gratings

For the Phase-shift Bragg gratings simulation it was defined the parameters presented in the following tables:

Chirp Input	
Grating length (mm)	10
Grating shape	Sinusoidal
Predefined analytic function	Uniform
Grating period (nm)	535

Table 3.1 – Chirp input parameters.

Apodization Input		
Coefficient for DC index change due to apodization		0
AC index change:	*Predefined analytic function*	Uniform
	AC index change	10^{-5}

Table 3.2 – Apodization input parameters.

Phase-shift Input	
Predefined analytic function	Uniform phase-shift
Phase-shift (degree)	90
Distance between phase-shift (mm)	5

Table 3.3 – Phase-shift input parameters.

Simulations of the grating spectral profile were made for phase-shifts of 30, 60 and 90 degrees. For each phase-shift value, the grating length was varied for 10, 20 and 30 mm, together with AC modulation index (10^{-5} to 10^{-4}). The distance between two neighboring phase-shifts was defined at the middle of the grating, i.e., for a 10 mm grating the phase-shift is at 5 mm. Figure 3.6 shows the simulations for Bragg gratings with a 30° phase-shift where the length and the AC modulation index were varied.
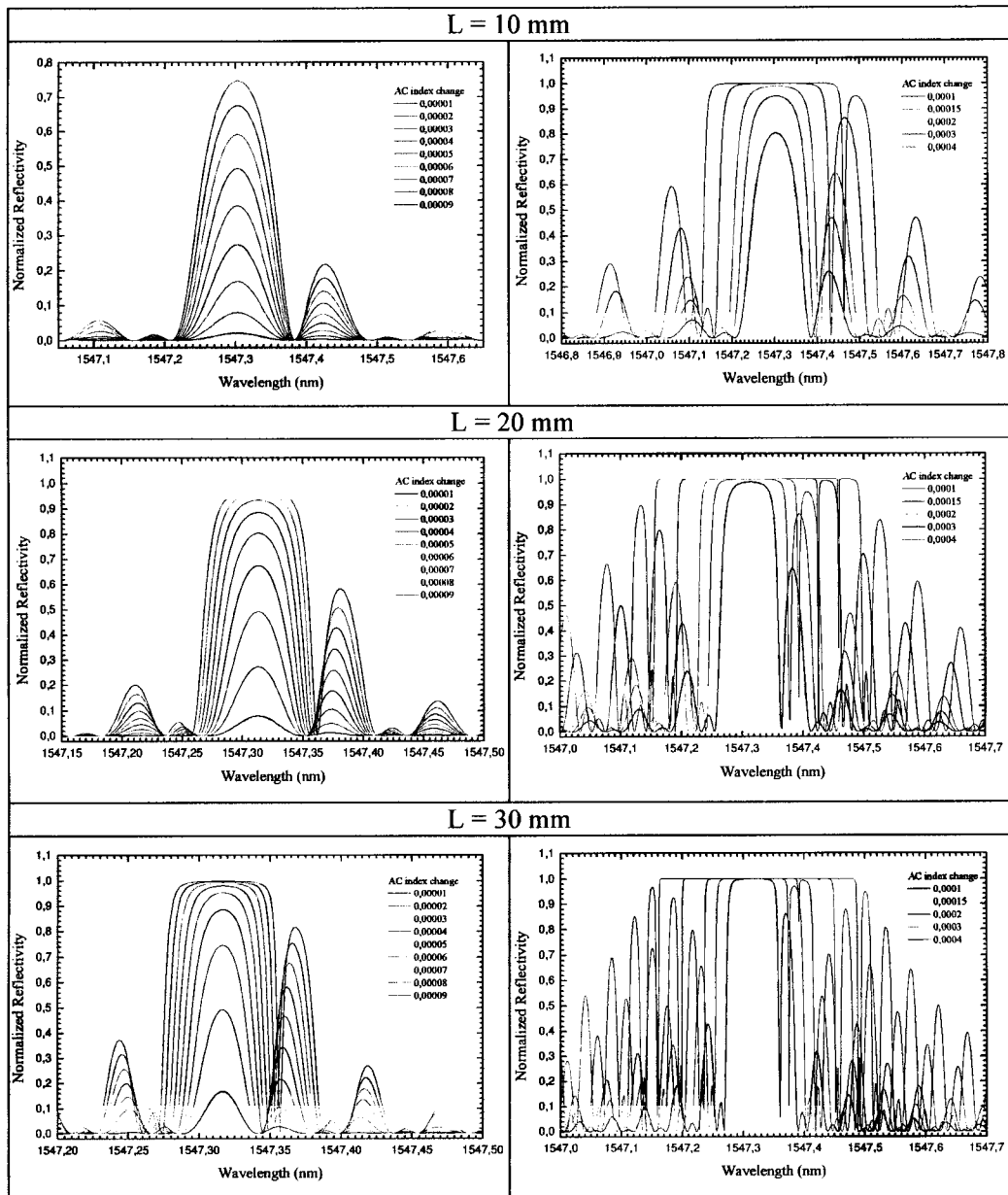
Figure 3.6 – Reflection spectrum of 30° phase-shift Bragg gratings with lengths of 10 mm, 20 mm and 30 mm, for different refractive index modulation indices.

As Figure 3.7 shows, the bandwidth of the transmission peak decreases with the increase of both grating length and AC modulation index.
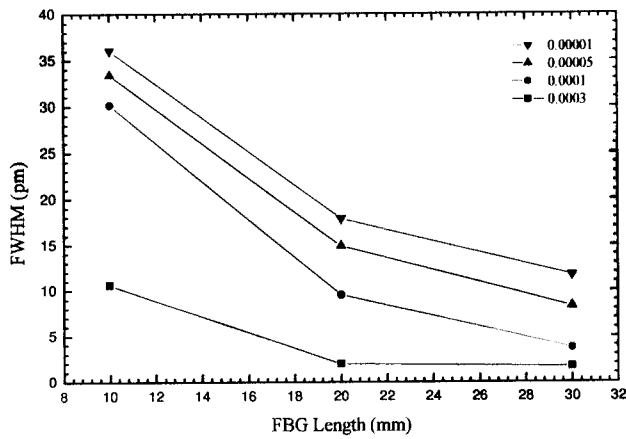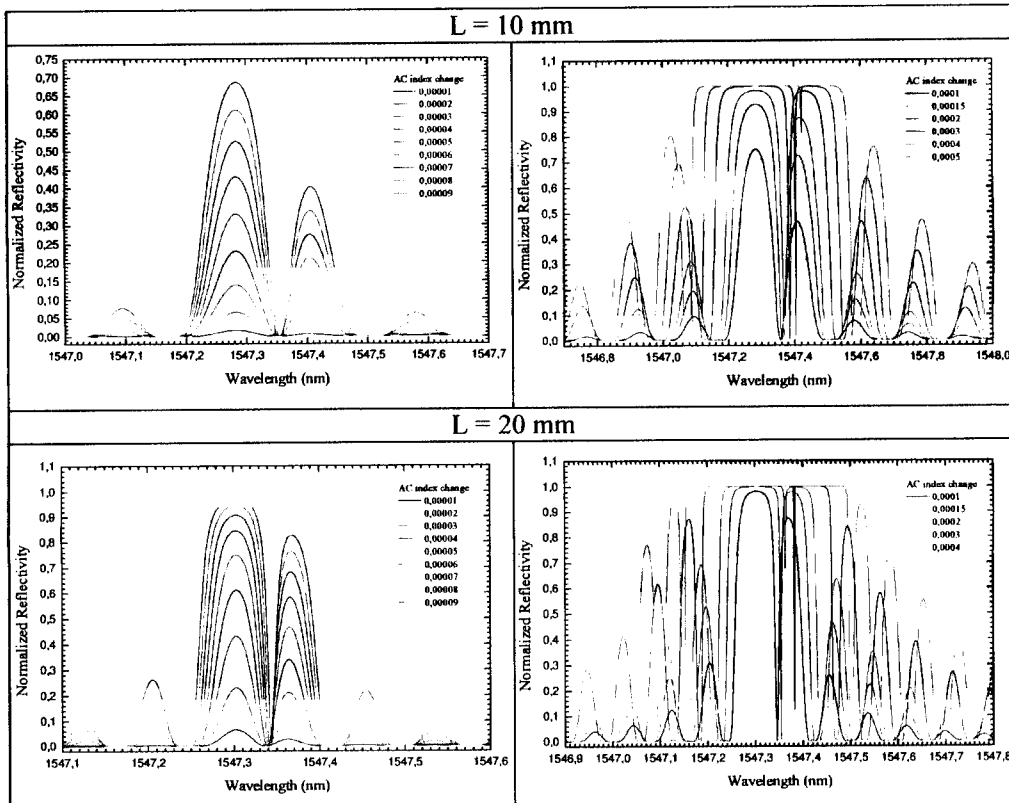
Figure 3.7 – Transmission peak bandwidth dependence on length and refractive index modulation index of a 30° phase-shift FBG.

Figure 3.8 shows the simulations for Bragg gratings with a 60° phase-shift where the length and the AC modulation index were varied.
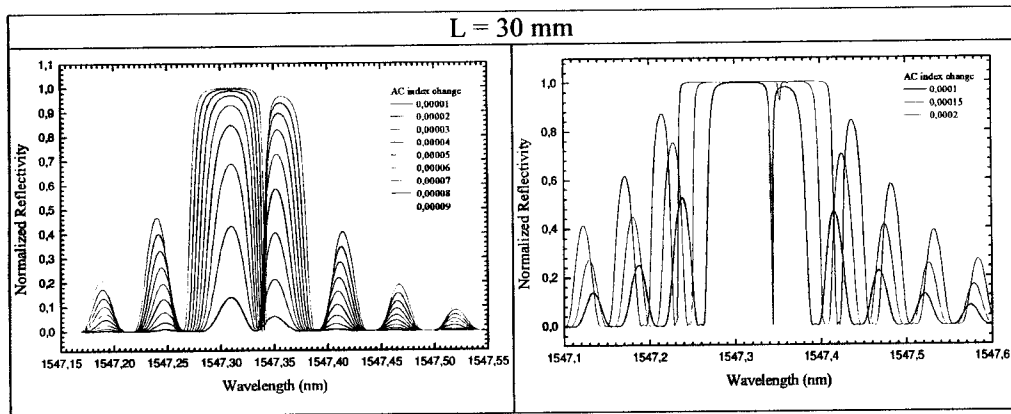
Figure 3.8 – Reflection spectrum of 60° phase-shift Bragg gratings with lengths of 10 mm, 20 mm and 30 mm, for different refractive index modulation indices.

The results are similar to the previous ones, except for the localization of the transmission band, which approaches the center of the spectral response. For this case, Figure 3.9 is the equivalent of Figure 3.7 for a 60° phase-shift.

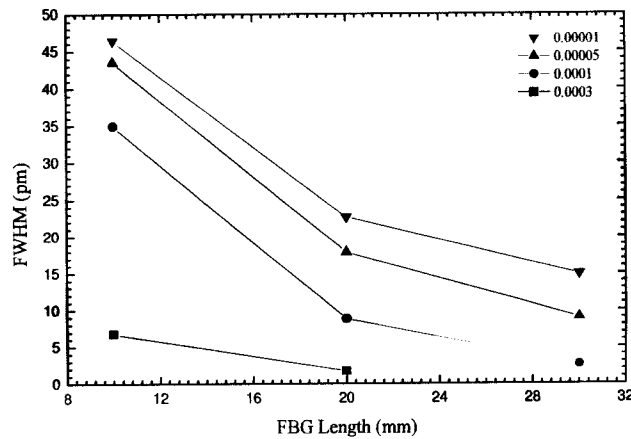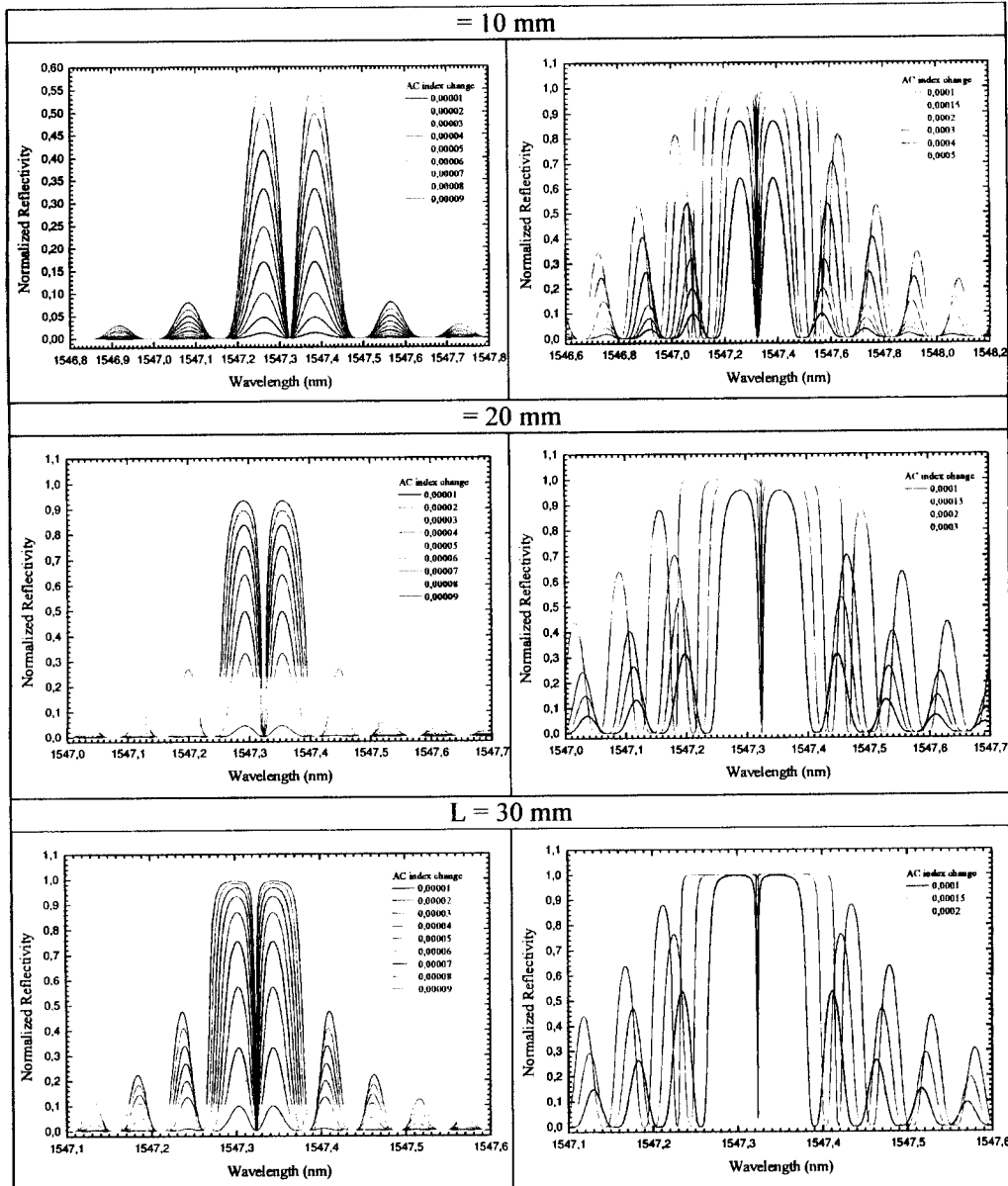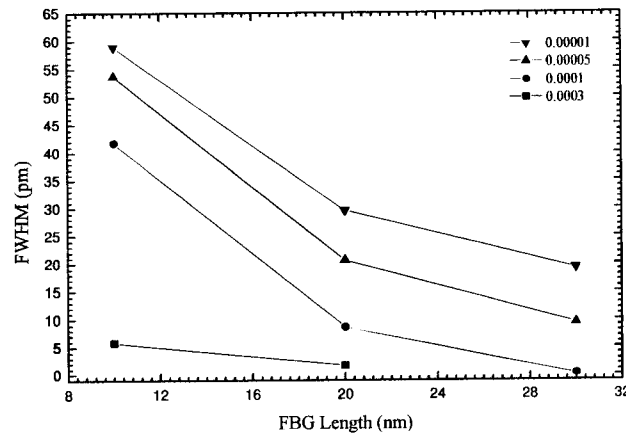**Figure 3.9** – Transmission peak bandwidth dependence on length and refractive index modulation index of a 60° phase-shift FBG.

Finally, Figure 3.10 and Figure 3.11 show the results for Bragg gratings with a 90° phase-shift. The most important feature observed is the localization of the transmission band on the center of the grating spectral response. Also, the transmission spectral width is slightly higher compared to the other cases because it is absence now the attenuation

effect associated with the edge of the grating spectral response (which also explains the smaller transmission spectral width of the 30° case compared with the 60° one).

Figure 3.10 – Reflection spectrum of 90° phase-shift Bragg gratings with lengths of 10 mm, 20 mm and 30 mm, for different refractive index modulation indices.

Figure 3.11 – Transmission peak bandwidth dependence on length and refractive index modulation index of a 90° phase-shift FBG.

One can observe that, for higher values of AC modulation index, the bandwidth of the transmission peak became so narrow that the simulation software has no resolution to display it. These results show that it is possible to gather the conditions to make from fibre Bragg gratings good optical filters. As will be shown in chapter 6, the introduction of chirp in phase-shifted fibre Bragg gratings will increase the rejection band, which combined with a sharp transmission peak can perform interesting spectroscopy functions.

3.6   Characteristics of Fabricated Phase-Shifted Fibre Bragg Gratings

The inscription of precise complex gratings, such as phase shifted structures, usually involves the translation of an interferogram by the desired phase-shift [52]. For the structure presented in this section, the shifting of the interference pattern is achieved by translating the phase mask, being the precision with which the phase shift is obtained determined by the precision of the induced spatial shift along the optical fibre, i.e., translation across the interferogram. Discrete phase shifts are normally used to open an extremely narrow transmission resonance in a reflection grating or to tailor the passive filter shape. The most well known application of discrete phase shifts is the use of a *quarter-wave* or π-shift in the center of a distributed-feedback laser. One way to obtain

a π round-trip phase shift in a Bragg grating is to move the phase mask at the mid-point of the grating by an appropriated distance l given by the relation

$$l = \frac{\Lambda_{pm}}{4\pi}\phi$$ (3.21)

where Λ_{pm} is the phase mask pitch and ϕ is the phase shift (l should be $\frac{\Lambda_{pm}}{4}$ for a π-shift).

Figure 3.12 shows a π-shift fibre Bragg grating fabricated at INESC Porto infrastructure by displacing the phase mask at the middle of the total grating length.
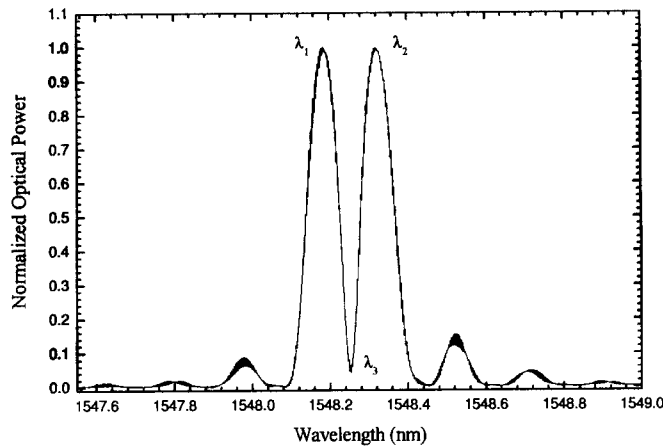
Figure 3.12 – Reflection spectrum of a π-shift fibre Bragg grating.

The grating, with 10 mm length, was fabricated in hydrogen loaded standard Single Mode Fibre and the UV beam was scanned behind the phase mask. During fabrication, the grating growth was directly monitored by a spectrum analyser, with a resolution of 0.1 nm. For grating characterization, the spectrum was measured with a resolution of 1 pm with the commercial interrogation system *BraggMeter* from *FiberSensing*. The width of reflection band is approximately 232 pm and the width of the central notch is about 52 pm.

The response of the π-shift Bragg grating was characterized to temperature variation, as shown in Figure 3.13. The structure was placed in a tube furnace and submitted to increasing values of temperature.
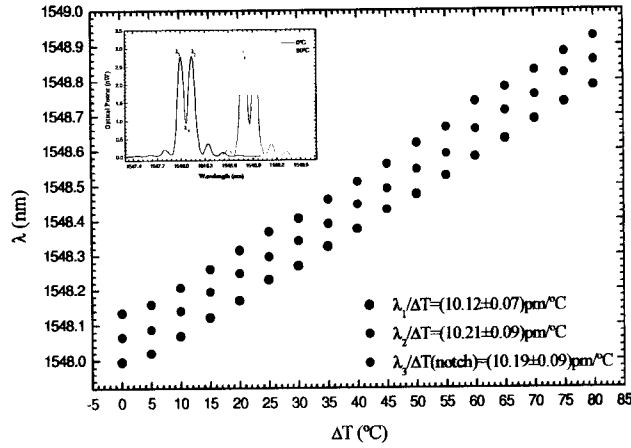
Figure 3.13 – Temperature response of the π-shift fibre Bragg grating.

The results show that the structure has linear variation with temperature and the optical power of each peak (λ_1, λ_2 and λ_3 - the central notch) is not affected by the physical parameter (inset of Figure 3.13). The wavelength temperature sensitivity is $(10.12 \pm 0.07) pm/^\circ C$ and $(10.21 \pm 0.09) pm/^\circ C$ for λ_1 and λ_2, respectively, and $(10.19 \pm 0.09) pm/^\circ C$ for the central notch, λ_3. As expected the values are similar in all cases.

The π-shifted Bragg grating was also characterized in strain. The grating was fixed at two points distanced by 60 cm and submitted to specific strain values (successive 10 μm displacements) by using a translation stage. The results are given in Figure 3.14.
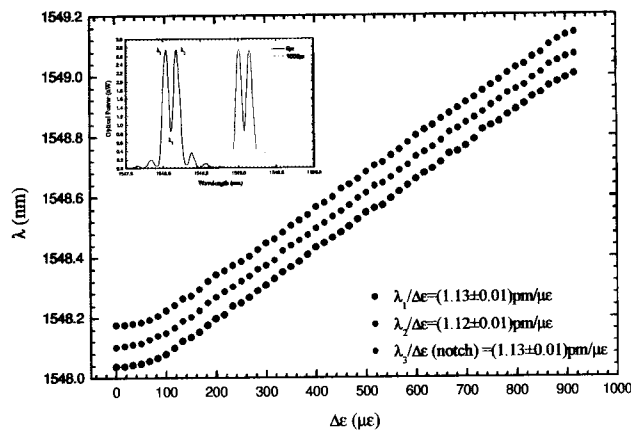

Figure 3.14 – Longitudinal strain response of the π-shift fibre Bragg grating.

Again, the peaks λ_1, λ_2 and λ_3 have linear response to strain variations and are not affected in power by the physical parameter (inset of Figure 3.14). The strain sensitivity is $(1.13 \pm 0.01) pm/\mu\varepsilon$ and $(1.12 \pm 0.01) pm/\mu\varepsilon$ for λ_1 and λ_2, respectively, and $(1.13 \pm 0.01) pm/\mu\varepsilon$ for the central notch, λ_3. Has it would be foreseen, the obtained sensitivities are similar to those associated with a uniform Bragg grating.

Although this structure is suited for optical filtering, in chapter 6 will be demonstrated that narrower widths for the central notch and larger widths for the reflection band will be needed for certain ultra-narrow optical filtering applications, as is the case of LIDAR spectroscopy. In such cases, it will be shown that the combination of phase shift and chirp permits to obtain fibre Bragg grating devices with characteristics that matches such requirements.

4

Fabry-Perot Interferometers Based on Fibre Bragg Gratings

4.1   Introduction to Fabry-Perot Interferometers

The Fabry-Perot interferometer is based on the interference of multiple reflected beams and is a key element of considerable importance in nowadays optics [21, 58]. Despite its simple configuration, it has been shown that it is a powerful tool in many applications. It is used in precise measurements of wavelength, analysis of ultra-narrow spectral lines, determination of the refractive index of glasses and metric calibrations. Besides playing an important role in spectroscopy with high spectral resolution, it is also the base configuration for various laser cavities.

In essence, the Fabry-Perot interferometer consists of a pair of identical plates, having plane-parallel internal faces of reflectivity R, separated by a uniform spacing d (see Figure 4.1).
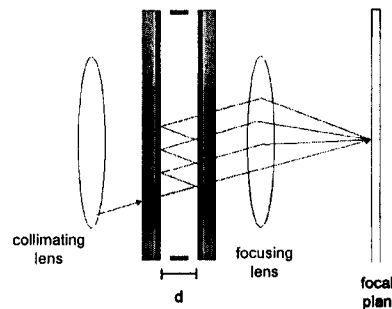

Figure 4.1 – Scheme of the Fabry-Perot interferometer. [58]

In practice, the surfaces are based in semi-transparent mirrors, quartz plates or even optical fibres with cuts perpendicular to the longitudinal direction of propagation – i.e., reflectivity defined by the Fresnel reflection of 4% –. The surfaces can also have high

reflecting coatings – with thickness of $\sim 10^{-8}$ m – which are normally fabricated by thin-film deposition processes.

When the system is used as an interferometer, the distance d between surfaces may vary some micrometers to some centimeters, but it can have several meters when used as a resonant cavity of a laser. If the reflecting surfaces are immovable, the system is referred as *etalon*. Normally, the medium between reflectors is air; however, in the general case, the medium will have a refractive index n. The internal faces of the reflectors are responsible for the interference of multiple beams inside the cavity, while the external faces are normally built with a very small angle relative to the internal parallel face. Thus, it is possible to eliminate interferences that might appear between reflected beams in both external and internal surfaces.

The transfer function – in transmission or reflection – of a Fabry-Perot cavity can be easily found. Figure 4.2 illustrates the multiple reflected and transmitted beams acting in the cavity, for an incident beam of amplitude E_i and incidence angle θ_i.
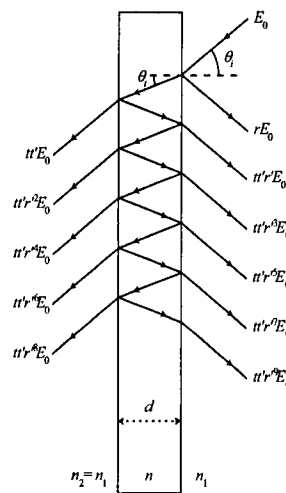

Figure 4.2 – Fabry-Perot cavity with multiple reflected and transmitted beams. [58]

The reflection and transmission coefficients, r and t respectively, in the first interface are related with the corresponding coefficients, r' and t', in the second interface, as follows:

$$tt' = 1 - r^2$$
$$r = -r' = e^{i\pi}r' .$$

$$(4.1)$$

These equations are valid when $n_2 = n_1$, as it is illustrated in Figure 4.2. The optical path difference between adjacent beams is given by

$$\Lambda = 2nd\cos\theta_t \qquad (4.2)$$

and the corresponding phase difference is

$$\phi = k_0\Lambda = \frac{4\pi nd\cos\theta_t}{\lambda_0}, \qquad (4.3)$$

where λ_0 is the central wavelength of the incident radiation, d is the distance between reflection surfaces and n is the refractive index of the cavity.

The complex notation used to describe optical fields simplifies the following analysis. The amplitudes of the transmitted waves are given by

$$
\begin{aligned}
E_{1t} &= E_i tt'e^{i\omega t} \\
E_{2t} &= E_i tt'r'^2 e^{i(\omega t-\phi)} \\
E_{3t} &= E_i tt'r'^4 e^{i(\omega t-2\phi)} \\
&\vdots \\
E_{Nt} &= E_i tt'r'^{2(N-1)} e^{i[\omega t-(N-1)\phi]}
\end{aligned}
\qquad (4.4)
$$

The total transmitted wave will be the sum of all components described in equation (4.4), following that

$$E_t = E_{1t} + E_{2t} + E_{3t} + \ldots + E_{Nt} = E_i e^{i\omega t}\left[\frac{tt'}{1-r^2 e^{-i\phi}}\right]. \qquad (4.5)$$

The intensity of this wave is proportional to the square of the (complex) amplitude E_t. Thus, multiplying both terms of the expression by its complex conjugated, results

$$I_t = \frac{(tt')^2}{(1+r^4)-2r^2\cos\phi} I_i. \qquad (4.6)$$

Using the trigonometric relation $\cos\phi = 1 - 2\sin^2\left(\phi/2\right)$, the previous expression takes the form

$$I_t = \frac{I_i}{1 + F\sin^2\left(\dfrac{\phi}{2}\right)}, \tag{4.7}$$

where the *finesse* coefficient F is defined by the formula

$$F = \frac{4r^2}{\left(1-r^2\right)^2} = \frac{4\mathcal{R}}{\left(1-\mathcal{R}\right)^2}, \tag{4.8}$$

and $\mathcal{R}$ is the reflectivity of the surface. As it was referred before, in this case both surfaces have the same reflectivity. Equation (4.8) gives the *finesse* coefficient of an ideal interferometric system; however, in real situations, this coefficient is affected by parameters that will be considered in the following analysis.

The throughput of the interferometric system is limited by losses in the cavity, which are due to absorption or scattering. Without lack of generality, these effects can be combined into one number and treated as if losses were only due to absorption in the high reflective coating of the surfaces. In order to achieve high throughput through the entire system, one therefore has to minimize absorption and scattering in the cavity of the interferometer. This is usually not a strong limitation with dielectric coatings, where losses significantly below 1% can be routinely achieved (0.2% is a typical value).

In practice, the Fabry-Perot plates are neither flat nor perfectly parallel. Small deviations in both these quantities will broaden the interferometer passband and thus reduce the *finesse* coefficient of the filter. These so-called plate defects can be grouped into three different categories. These categories are deviations from flatness, surface irregularities/micro-defects, and departure from parallelism. Thus, defect *finesse* coefficient can be defined for each of these effects.

Assuming spherically bowed plates with a maximum excursion from the plane surface of δt_s, the flatness defect *finesse* coefficient, F_{DS}, is given by [59]

$$F_{DS} = \frac{\lambda}{2\delta t_s}. \tag{4.9}$$

Surface irregularities and micro-defects are modeled by a Gaussian distribution with a root-mean-square width of $\left(\delta r_G^2\right)^{1/2}$. The corresponding defect *finesse* coefficient is then given as

$$F_{DG} = \frac{\lambda}{4.7\left(\delta r_G^2\right)^{1/2}}.$$ (4.10)

Finally, with a departure from parallelism of δr_P, one obtains for the parallelism defect *finesse* coefficient

$$F_{DP} = \frac{\lambda}{\sqrt{3}\,\delta r_P}.$$ (4.11)

Usually, all three defects occur simultaneously and independently with an overall defect *finesse* coefficient, F_D, which can be obtained approximately by [59]

$$\frac{1}{F_D^2} = \frac{1}{F_{DS}^2} + \frac{1}{F_{DG}^2} + \frac{1}{F_{DP}^2}.$$ (4.12)

Using a capacitance stabilized servo system makes the parallelism defect negligible. Furthermore, the defect *finesse* coefficient due to the smoothness of the plates is typically negligible when compared to the flatness defect. Therefore, it is valid that $F_D \approx F_{DS}$.

Light passing through a Fabry-Perot will, in general, be spread over a finite range of angles. Again, this effect will broaden the transmission peak and result in a reduced effective *finesse* coefficient. In analogy to the above plate defects, a so-called aperture *finesse* coefficient F_A can be defined as

$$F_A = \frac{2\pi}{n\Omega},$$ (4.13)

with n being the order of the transmission peak and Ω the solid angle of the cone of rays passing through the cavity.

An effective *finesse* coefficient F_E can be defined, that directly indicates the bandwidth of a realistic Fabry-Perot filter. It depends on three quantities: the reflection *finesse* coefficient F given already by equation (4.8), which is the *finesse* coefficient of

an ideal Fabry-Perot, the defect *finesse* coefficient F_D, and the aperture *finesse* coefficient F_A. The effective *finesse* coefficient can then be found to be approximated by [59]

$$\frac{1}{F_E^2} = \frac{1}{F^2} + \frac{1}{F_D^2} + \frac{1}{F_A^2}.$$ (4.14)

The reflection *finesse* coefficient can be increased by increasing the reflectance of the high-reflection coating on the plates. As pointed out above, the maximum reflectivity is determined by the minimum required throughput. Therefore, it can be summarized that the main practical limitations for the effective *finesse* coefficient are the intra-cavity losses and the flatness of the plates. In contrast to the reflectance of the plates, their flatness is a significant cost driver. Therefore, if a certain resolution is desired it usually makes sense to chose F_D approximately equal to F.

The transmissivity of the cavity is defined as a transmission (normalized) transfer function; i.e.

$$\mathcal{T} \equiv \frac{I_t}{I_i} = \frac{1}{1 + F \sin^2\left(\dfrac{\phi}{2}\right)}.$$ (4.15)

The transfer function of a Fabry-Perot cavity for different values of $\mathcal{T}$ is illustrated in Figure 4.3, considering normal incidence ($\theta_i = 0$), $n = 1$ and $d = 200$ µm [60].
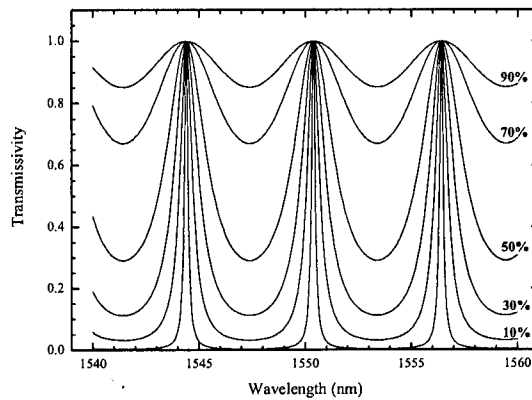
Figure 4.3 – Transmission transfer function of a Fabry-Perot cavity, for different values of T (4%, 10%, 30%, 50%, 70% e 90%), considering $\theta_i = 0$, $n = 1$ and $d = 200$ µm. [60]

The values of maximum transmission occur when $\phi = 2m\pi$ (m is an integer) which corresponds to the situation where the multiple waves are in phase. These maximum values are independent of the reflectivity in both surfaces, which means that, for surfaces with high reflectivity, it is possible in principle to have high transmission (even for $\mathcal{R} > 99\%$).

Several applications require that the interferometer has high sensitivity. The maximum sensitivity occurs for values of λ given by $\mathcal{T} = 1 - \frac{1}{4}(1 - \mathcal{T}_{min})$, corresponding to a high *finesse* coefficient, and for values of λ given by $\mathcal{T} = 1 - \frac{1}{2}(1 - \mathcal{T}_{min})$, corresponding to a low *finesse* coefficient.

Each period of the transfer function corresponds to $\Delta\phi = 2\pi$. If the cavity is illuminated by a broadband source at normal incidence, the wavelength range $\Delta\lambda$ between consecutive maxima is determined by the following expression

$$\Delta\lambda = \frac{\lambda_0^{\;2}}{2nd}.$$

(4.16)

This function varies with the dimensions of the cavity, as it is shown in Figure 4.4, for $\lambda_0 = 1550$ nm and $n=1$ [60].
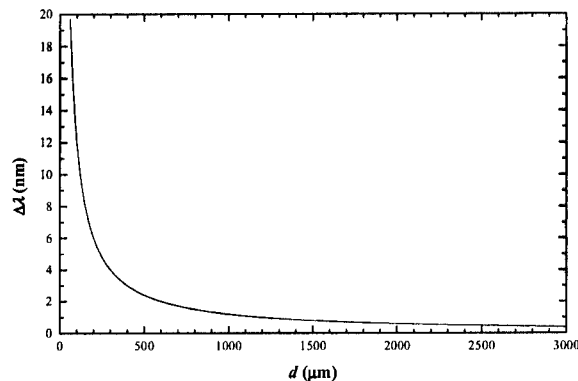
Figure 4.4 – Separation between consecutive maxima of the transfer function given by equation 4.16, for $\lambda_0 = 1550$ nm and $n = 1$. [60]

The complementary function of the transmissivity can be easily obtained when using the following relation

$$\mathcal{T} + \mathcal{R} = 1.$$

(4.17)

Thus, the reflectivity of the cavity is given by

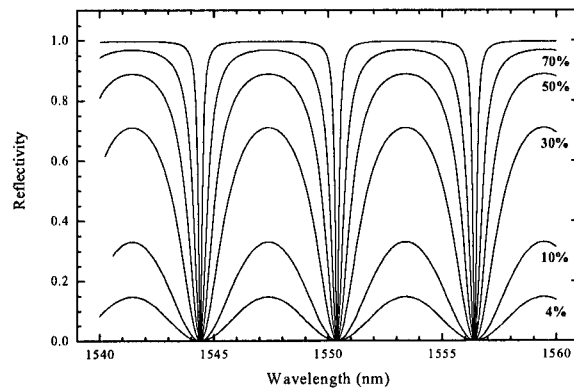$$\mathcal{R} = \frac{F \sin^2\left(\dfrac{\phi}{2}\right)}{1 + F \sin^2\left(\dfrac{\phi}{2}\right)} \, . \qquad\qquad (4.18)$$

This function is represented in Figure 4.5, considering $\theta_i = 0$, $n = 1$ and $d = 200$ μm [60].

In the general case $n_2 \neq n_1$, which means that the effective reflectivity of each surface is different. In this situation, the equations (4.15) and (4.18) have the most general form

$$\mathcal{T} = \frac{(1 - R_1)(1 - R_2)}{\left(1 - \sqrt{R_1 R_2}\right)^2 + 4\sqrt{R_1 R_2}\, \sin^2\left(\dfrac{\phi}{2}\right)} \qquad\qquad (4.19)$$

and

$$\mathcal{R} = \frac{\left(\sqrt{R_1} - \sqrt{R_2}\right)^2 + 4\sqrt{R_1 R_2}\, \sin^2\left(\dfrac{\phi}{2}\right)}{\left(1 - \sqrt{R_1 R_2}\right)^2 + 4\sqrt{R_1 R_2}\, \sin^2\left(\dfrac{\phi}{2}\right)} \, . \qquad\qquad (4.20)$$


Figure 4.5 – Reflectivity function of a Fabry-Perot cavity, for different values of $\mathcal{R}$(90%, 70%, 50%, 30%, 10% e 4%), considering $\theta_i = 0$, $n = 1$ and $d = 200$ μm.[60]

The Fabry-Perot interferometer operating in reflection is an interesting configuration as a sensor element. Moreover, enables remote operation and gives almost unitary visibility – defined by $\left(\mathcal{R}_{m\acute{a}x} - \mathcal{R}_{min}\right)/\left(\mathcal{R}_{m\acute{a}x} + \mathcal{R}_{min}\right)$ – even in situation of low *finesse*.

4.2   Fabry-Perot Interferometers Based on Fibre Bragg Gratings

The fibre Fabry-Perot (FFP) sensor has shown considerable potential for the measurement of parameters such as temperature and strain and is one of the preferred interferometric sensor configurations since it is simple to deploy, has high sensitivity, enables multiplexing operation, and is guide insensitive since light is transmitted to the sensor and back through the same fibre.

The first use of the fibre Fabry-Perot sensor was proposed by Kist and Sohler [61]; thereafter, extensive studies on the intrinsic and extrinsic type optical fibre sensors, whose interference mediums are optical fibre and air, have continued. Figure 4.6 illustrates an extrinsic fibre Fabry-Perot interferometer. The air-spaced Fabry-Perot cavity is formed by fixing two separated lengths of optical fibre into a suitable tube. The alignment is achieved with the capillary tube where the diameter is slightly superior to the cladding's diameter of the optical fibre. This cavity is of simple implementation and has several applications [62-64].
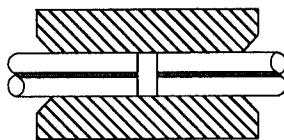
Figure 4.6 – Scheme of an extrinsic fibre Fabry-Perot interferometer. **[60]**

Many configurations of intrinsic fibre Fabry-Perot interferometers have been proposed. The most common technique to fabricate intrinsic FFP involves sputtering dielectric thin films on the cleaved ends of the fibre spacer and then fusing the cavity in-line with the lead fibres [65]. Another approach uses a short segment of silica hollow-core fibre spliced between two sections of single mode fibre to form a mechanically robust in-line optical cavity [66].

After the outcome of fibre Bragg gratings (FBGs) a natural approach to built up intrinsic FFP structures is using the reflection properties of the gratings, i.e, the FFP

mirrors are two fibre Bragg gratings with identical reflection properties, preferably with large spectral bandwidth [67]. These cavities are much easier to fabricate than other intrinsic FFP structures and comparatively to the extrinsic FFP show a considerably higher mechanical strength.

Figure 4.7 illustrates a FFP based on FBGs. As will be described in chapter 5, a simple way to fabricate such device is just by applying an electric arc at the middle of a fibre Bragg grating. In the present case, the fabrication process was based on a 10 mm fibre Bragg grating that is cut in half, forming two shorter gratings that are spliced to an optical fibre with 5 mm length.
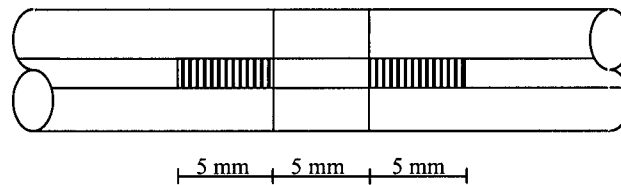
Figure 4.7 – Scheme of an intrinsic fibre Fabry-Perot interferometer.

The spectral response of this FFP is shown in Figure 4.8. The periodicity between fringes is 50 pm and the FWHM of the envelope is approximately 240 pm.

Figure 4.8 – Spectral response of a fibre Bragg grating based intrinsic Fabry-Perot interferometer.

The normalized reflection spectrum of the interferometer shown in Figure 4.8 can be written as (assuming unitary visibility) [68]

$$R(\lambda) = R_B(\lambda)\left[1+\cos(\phi)\right] \qquad (4.21)$$

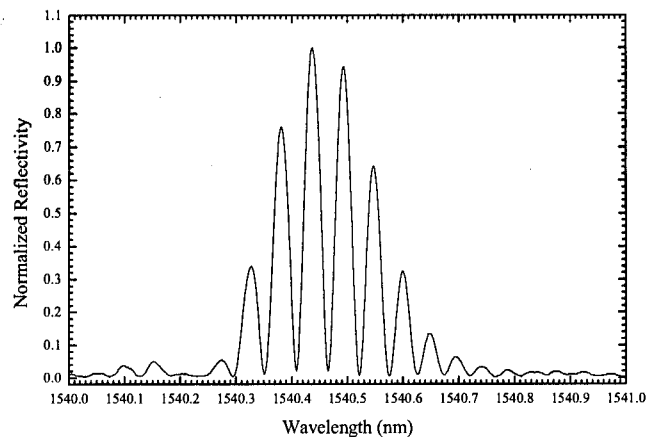where $R_B(\lambda)$ is the reflection spectrum of the single Bragg grating and ϕ is the phase difference between the two waves reflected by the FBG mirrors, given by

$$\phi = \frac{4\pi n L_{FP}}{\lambda}$$ (4.22)

where n is the effective index of the fibre core, λ is the wavelength of light and L_{cav} is the cavity length. As follows from equation (4.21), the reflection spectrum of the interferometer is a product of two components. The first component is the reflection spectrum of the gratings, which forms an envelope function. The second component is a cosinusoidal modulation due to the interference between the waves reflected from the gratings. Both components in the spectrum (equation 4.21) change due to the influence of the measurand. The relative shift of the Bragg wavelength, which determines the center position of the envelope function $R_B(\lambda)$ in the spectrum, is the same as in traditional Bragg grating sensors. If the measurand has an equal effect on the twin gratings and the fibre between them, the cosinusoidal modulation component shifts at the same rate as the envelope. Therefore, under the measurand influence, the reflection spectrum of the interferometer shifts while maintaining its shape. Following these statements, the FFP shown in Figure 4.8 was characterized in strain. The sensing structure was fixed at two points distanced by 50 cm and submitted to specific strain values (successive 20 μm displacements) by using a translation stage. The results are given in Figure 4.9.
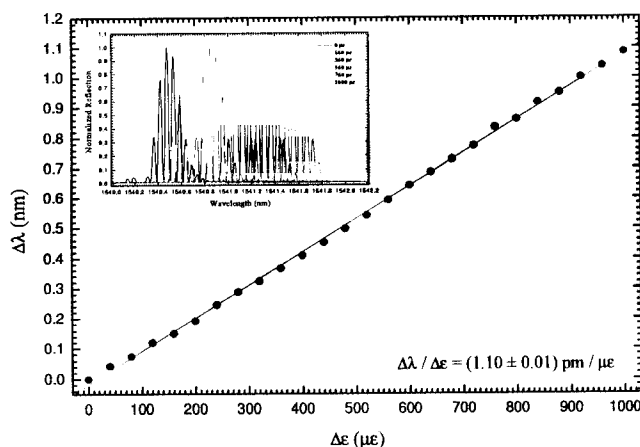

Figure 4.9 – Wavelength shift versus applied strain of the intrinsic Bragg grating FFP interferometer.

The strain sensitivity is $1.10\,pm/\mu\varepsilon$ and, as it would be expected, is the value predicted for a single fibre Bragg grating submitted to strain. The insight of Figure 4.9 shows that, under the measurand influence, the reflection spectrum of the interferometer shifts while maintaining its shape. This means that the fringes of the interferometer move at the same rate as the envelope.

Due to the influence of the measurand, the Bragg wavelength of the envelope spectrum shifts and consequently, by equation (4.22), the phase of the cosinusoidal interference pattern will change as well. Therefore, for pure interferometric operation it is desirable the envelope effect to be as small as possible, which is achieved combining the utilization of mirror Bragg gratings with large spectral bandwidth with a limited measurement range. In those conditions, the interferometer return power is given by the usual relation

$$P = P_o(1 + k\cos\phi) \qquad (4.23)$$

where P_o and k (the fringe visibility) are approximately constants. The interferometric phase variation with the strain change can be recovered using specific signal processing techniques, as it will be described later. For the moment, the phase variation was obtained in a rough way by monitoring one of the peaks of the channeled spectrum in Figure 4.8. The obtained result is shown in Figure 4.10.
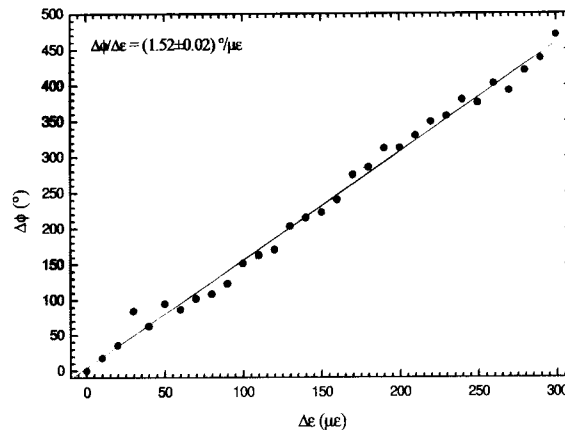
Figure 4.10 – Phase change of the intrinsic FFP interferometer versus applied strain.

As it would be expected, there is a linear response of the phase variation with the applied strain. The sensitivity is $1.52\ °/\mu\varepsilon$ and the resolution of the measurements is

approximately 4.2°, a coarse value as expected in face of the measurement technique utilized.

4.2.1   Cavity Length

In chapter 2 it was discussed and demonstrated theoretically that the apparent reflection of a fibre Bragg grating is at the middle of the structure. A simple form to demonstrate practically this statement is with fibre Fabry-Perot interferometers based on Bragg gratings.

Figure 4.11 shows the scheme of an intrinsic FFP based on a single fibre Bragg grating.

Figure 4.11 – Scheme of an intrinsic fibre Fabry-Perot interferometer.
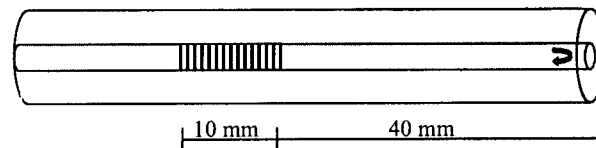
The FFP cavity is formed by a trench of optical fibre with 40 mm length. One of the mirrors is a Bragg grating with 10 mm length and the other mirror is the 4% Fresnel reflection at the end of the cleaved fibre. The spectral response of this structure is presented in Figure 4.12.
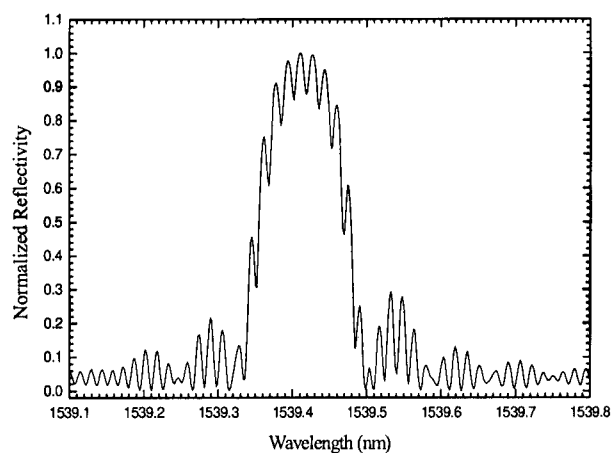

Figure 4.12 – Spectral response of an intrinsic Fabry-Perot interferometer.

The reduced fringe visibility is a consequence of the difference in the intensity of the interfering waves. The fringe periodicity, $\partial\lambda$, is 16.9 pm and the FWHM of the envelope is approximately 122.6 pm. Assuming that the apparent reflection is at the middle of the grating, the cavity length theoretical value will be 45 mm. The interferometric phase is given by equation (4.22), from where it can be obtained the cavity length, L_{FP} :

$$L_{FP} = \frac{\lambda_B^2}{2n\partial\lambda} \qquad (4.24)$$

For a Bragg wavelength of 1539.42 nm the cavity length will be approximately 48 mm. The difference to the expected value of 45 mm may be due to a not exact length of 10 mm and 40 mm for the FBG and the piece of fiber, respectively, and the grating not to be exactly uniform.

4.3   Application as Strain Sensing Structures

There has been a considerable interest in strain measurement using optical fibre sensors for structural health monitoring in smart structure systems. Among many different types of fibre optic interferometric techniques developed for this purpose, the most frequently used is the fibre optic Fabry-Perot interferometer [69].

Several configurations based of FFP interferometers have been proposed to measure strain [68-71]. However, the recovering of the interferometric phase, which contains the information about a particular measurand that acts on the optical path difference of the cavity, is not straightforward. One common technique uses two interferometric signals that change in quadrature [72-76]. In the following sections it is proposed two configurations based on this type of phase modulation technique. For measurement of strain, an intrinsic FFP based on the scheme presented in Figure 4.7 is used. In the first configuration is used a tunable laser to cause at the output of the FFP interferometer a phase difference of 90° and in the second one a π-shifted grating is used to modulate the phase.

4.3.1   Sensing Configuration

Figure 4.13 shows the two configurations implemented to test the quadrature phase modulation techniques applied to a fibre Fabry-Perot interferometer based on Bragg gratings.

(a)

(b)
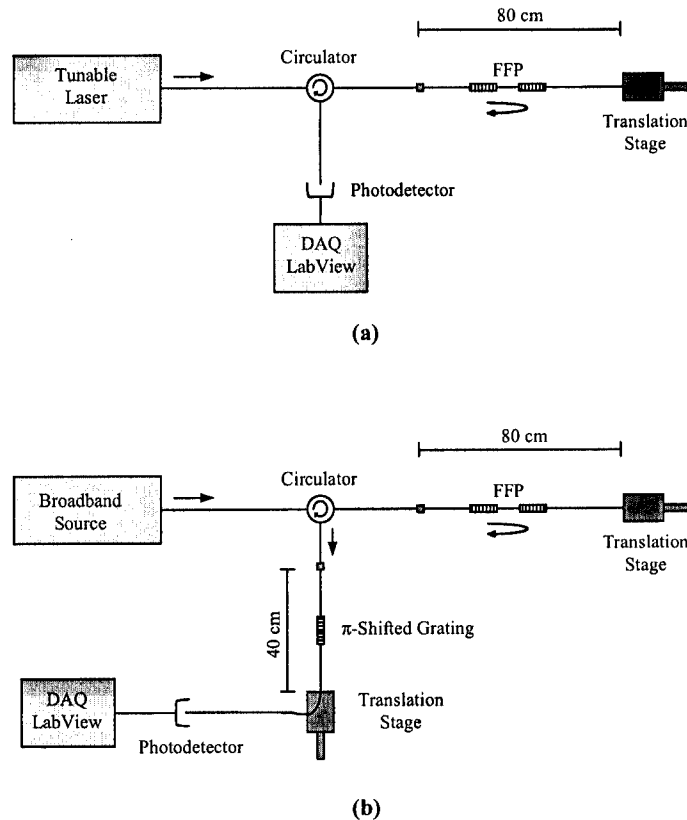
Figure 4.13 – Configurations for quadrature phase modulation techniques where is used a (a) tunable laser and (b) a π-shifted grating.

The configuration proposed in Figure 4.13(a) uses a tunable laser to modulate the phase of the FFP interferometer. This is achieved by emitting two specific wavelengths, $\lambda_{1,2}$, that will cause at the output of the interferometer a phase difference of 90°. Light reflected from the FFP is directed through the optical circulator to the photodetector, converted into a digital signal by means of a DAQ board and acquired by LabView[TM]. The strain is applied to the interferometer by means of a translation stage. For each displacement, two voltage values $(V_{1,2})$ are measured, corresponding to the respective wavelengths, $\lambda_{1,2}$.

In Figure 4.13(b) it is used a π-shifted grating to modulate the phase of the interferometer. This structure used in transmission will have the same functionality as the tunable laser. It will act as an ultranarrow tunable filter when submitted to strain. The phase modulation of the FFP is achieved by displacing the phase-shifted structure with a translation stage. Two specific strain values $\left(\varepsilon_{1,2}\right)$ are used in order to have at the output of the interferometer a phase difference of 90°. The output filtered signal is directed to the photodetector, converted into a digital signal by means of a DAQ board and acquired by LabView^{TM}. For each displacement of the interferometer, two voltage values $\left(v_{1,2}\right)$ are measured, corresponding to the respective values of strain $\left(\varepsilon_{1,2}\right)$ applied to the π-shifted grating. Using simple mathematical analysis, the acquired data can be easily demodulated, as it shows the next section.

4.3.2   Sensing System Demodulation

The phase of the reflected light from a fibre Fabry-Perot cavity is a function of wavelength (equation 4.22). Then, for each wavelength, the interferometric phase will have the following expression

$$\phi_j = \frac{4\pi n L_{FP}}{\lambda_j}, \qquad j = 1,2 \tag{4.25}$$

where $\lambda_{1,2}$ are the wavelengths considered. The relative phase between the interferometric signals is given by

$$\Delta\phi = 4\pi n L_{FP}\left(\frac{1}{\lambda_1} - \frac{1}{\lambda_2}\right). \tag{4.26}$$

These signals are in quadrature if the separation $\Delta\lambda$ between wavelengths is an odd multiple of $\lambda^2 / 8nL_{FP}$. For a specific cavity length is always possible to define two wavelengths that satisfy equation (4.26).

If the signals reflected by the two Bragg gratings are independently detected by photodiodes then the respective output voltages, v_1 and v_2, will be, for each wavelength, given by the following expressions

$$v_1 = V_1 \left(1 + k_1 \cos \phi_1 \right)$$

$$v_2 = V_2 \left[1 + k_2 \cos \left(\phi_2 + \Delta\phi \right) \right] = V_2 \left(1 + k_2 \sin \phi_1 \right)$$

(4.27)

where $V_{1,2}$ are constant voltage values associated to the signal amplitude and $k_{1,2}$ are the fringes visibility for each wavelength.

Adjusting the gain in such way that $k_1 V_1 = k_2 V_2$, the interferometric phase can be demodulated as follows

$$\phi \equiv \phi_1 = \tan^{-1} \left(\frac{v_2 - V_2}{v_1 - V_1} \right)$$

(4.28)

where the ambiguity of 2π is easily resolved with the use of simple processing algorithms.

4.3.3   Strain Measurement Results and Analysis

To perform the experiment shown in Figure 4.13 (a), it was used a FFP interferometer obtained by the method described in Figure 4.7. The respective optical spectrum is presented in Figure 4.14.
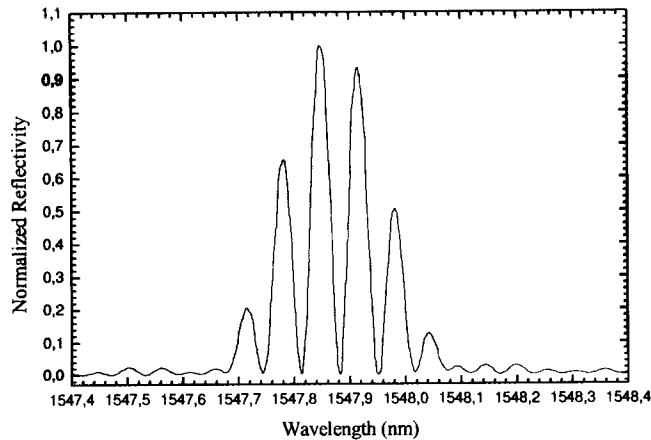
Figure 4.14 – Optical spectrum of a FFP interferometer based on the method described in **Figure 4.7**.

The periodicity between fringes is 60 pm and each one has a FWHM of approximately 33 pm. The FWHM of the envelope is approximately 245 pm.

The wavelength peak λ_1 of the tunable laser is centered on the wavelength peak of the envelope spectrum of the interferometer. For a minimum displacement of 2 μm, the wavelength of the selected fringe shifts approximately 5 pm, which results in a phase change of 30°. In order to have at the output of the interferometer a phase change of 90°, the laser is tuned into the second wavelength with an increment of 15 pm, i.e., $\lambda_2 = (\lambda_1 + 15)\,\mathrm{pm}$. Assuming that $V_1 = V_2 \equiv V_o$ and $k_1 = k_2 \equiv k$ then, equation (4.27) becomes

$$V_1 = V_o\left(1 + k\cos\phi_1\right)$$
$$V_2 = V_o\left(1 + k\sin\phi_1\right)$$

(4.29)

and the phase demodulation gets the following form

$$\phi \equiv \phi_1 = \tan^{-1}\left(\frac{V_2 - V_o}{V_1 - V_o}\right).$$

(4.30)

For each displacement of the FFP, two voltage values, V_1 and V_2, corresponding to λ_1 and λ_2, are acquired by LabView™. The results are shown in Figure 4.15.
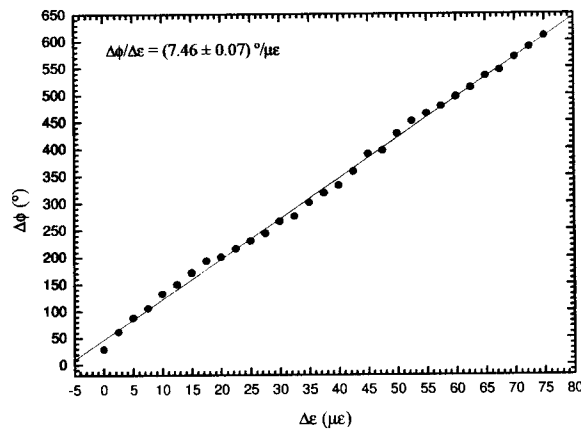

Figure 4.15 – Phase change of the interferometer versus applied strain.

As expected, a globally linear behavior is obtained, with a slope (strain phase sensitivity) of $7.46 \pm 0.07°/\mu\varepsilon$. The system resolution was also determined. For that a strain step of $10\,\mu\varepsilon$ was applied and the corresponding interferometric phase variation

registered, as shown in Figure 4.16. From the phase step obtained and the *rms* phase fluctuations it turns out a phase resolution of $2.8\mu\varepsilon$.
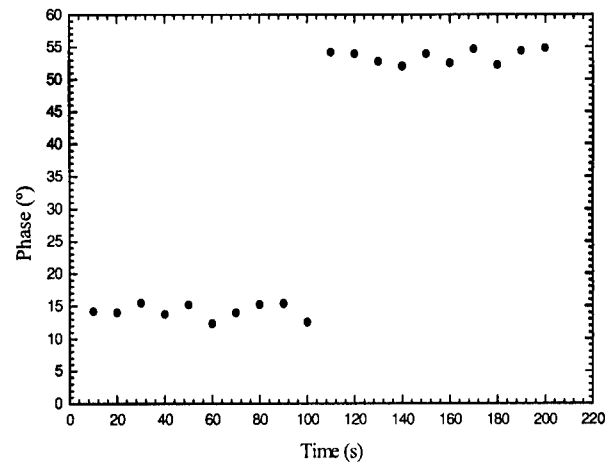
Figure 4.16 – Determination of system resolution for applied strain to the FFP interferometer.

To perform the experiment shown in Figure 4.13(b), it was necessary to fabricate a fibre Bragg grating based FFP with a fringe periodicity larger that the central notch of the demodulation π-shifted grating. Therefore, the FFP interferometer was obtained directly during the grating writing process placing a capillary tube at the middle of the phase mask. The respective optical spectrum is presented in Figure 4.17.
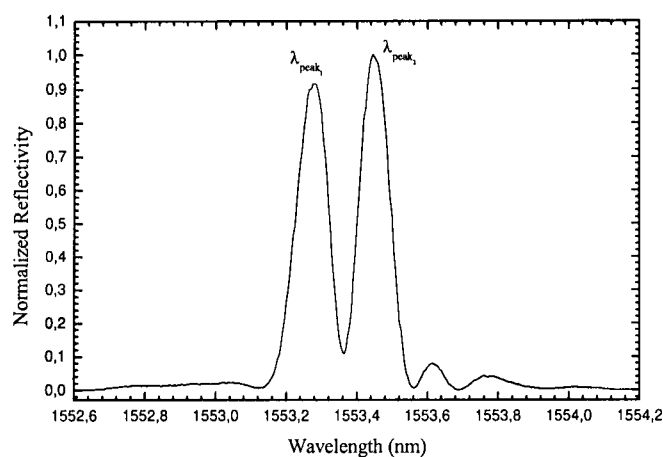
Figure 4.17 – Optical spectrum of a FFP interferometer based on a direct writing process where a capillary tube is placed at the middle of the phase mask to create the cavity.

The fringe periodicity is ≈ 170 pm. The FWHM of the fringes and of the envelope are ≈ 105 pm and ≈ 425 pm, respectively. In this experiment, the tunable laser is substituted by a broadband source to illuminate the system and the phase modulation of the FFP is achieved with a π-shifted grating. The optical spectrum of this fibre grating structure is presented in Figure 4.18.
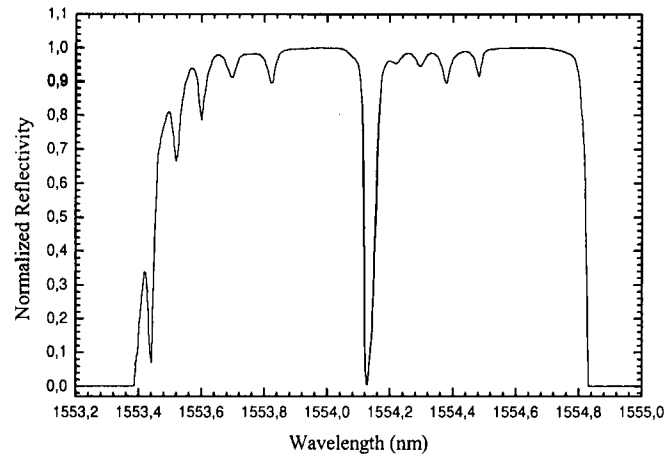
Figure 4.18 – Optical spectrum of a π-shifted Bragg grating.

The FWHM of the central notch is ~ 40 pm and the bandwidth of the rejection band is 1440 pm. The central notch acts as a tunable wavelength filter that, when scanned over the interferometer channeled spectrum, will change the output power in a way that is equivalent to a certain interferometric phase change. The scan is performed applying strain to the π-shifted grating with a translation stage. The notch is centered at the peak wavelength of the envelope spectrum of the FFP that corresponds to the strain value ε_1. For a peak-to-peak wavelength separation of 170 pm (360°) it is necessary to apply 42.5 $\mu\varepsilon$, which means that when $\varepsilon_2 = (\varepsilon_1 + 10.6)\mu\varepsilon$ a phase change of 90° is induced. For each displacement of the interferometer, two voltage values $(v_{1,2})$ are measured, corresponding to the respective values of strain$(\varepsilon_{1,2})$ applied to the π-shifted grating. The results are shown in Figure 4.19. The phase dependence with strain is linear, with a sensitivity of $(2.19 \pm 0.02)° / \mu\varepsilon$. This value is smaller than the one found in the context of Figure 4.15 because now the cavity length is smaller by a factor of ≈ 3.
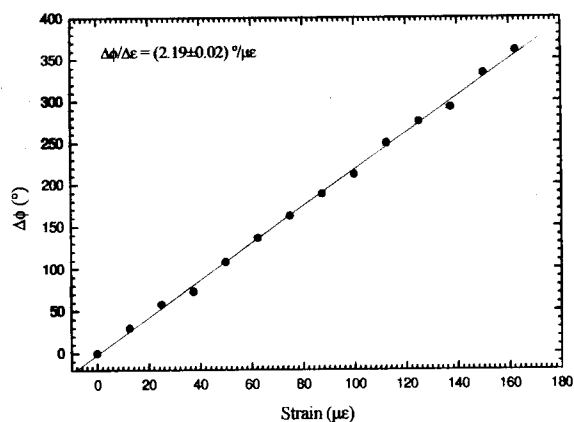
Figure 4.19 – Phase change of the interferometer versus applied strain.

In a way similar to what done in the context of Figure 4.16, the system performance was evaluated. For that a strain step of $50\mu\varepsilon$ was applied and the corresponding interferometer variation registered, as shown in Figure 4.20. It is clear now that the noise *rms* amplitude is smaller, which overcompensates the effect a smaller sensitivity, resulting into a resolution for the proposed configuration of $\approx 1.8\mu\varepsilon$.
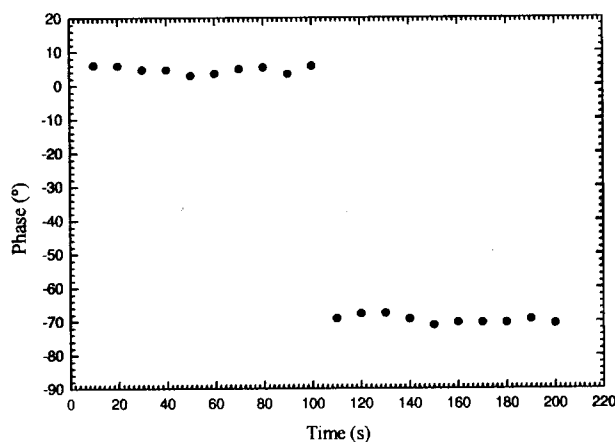
Figure 4.20 – System resolution for applied strain to the FFP interferometer when the demodulation is performed using the π-shift grating.

4.3.4   Dynamic Demodulation of Grating Based Fibre Fabry-Perot Sensors

In previous section, two phase interrogation approaches based on a phase modulation technique were proposed to measure strain, where two interferometric signals are

generated from the FFP cavity that change in quadrature. Another type of approach proposed to perform the phase recovery operation relies on the white light concept. In this case, the light returning from a low-finesse Fabry–Pérot cavity and emitted by an optical source with a coherence length larger than the cavity optical path difference is processed by a second interferometer located in the processing unit [77]. In a similar technique, the spectrum of the light arriving from the cavity is modulated by the spectral transfer function of a wavelength division multiplexer (WDM). This function is controlled by acting on the coupling length of the device [78]. In this section, it is proposed an interrogation technique for an FFP interferometer that is 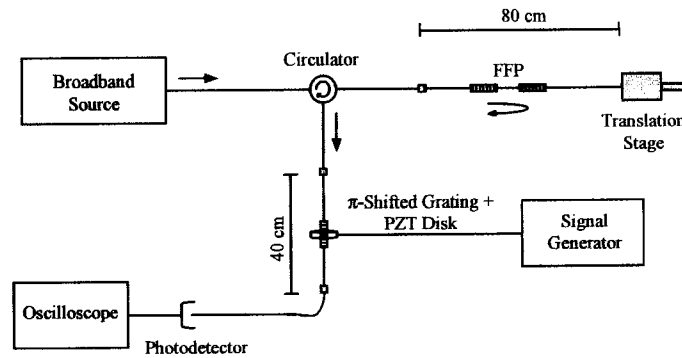based on the dynamic modulation of the spectrum of light arriving from the FFP cavity by the spectral transfer function of a π-shifted FBG. The setup is illustrated in Figure 4.21.

Figure 4.21 – Interrogation technique for a FFP interferometer based on the dynamic modulation of a π-shifted grating by means of a PZT disk.

The implementation of the demodulation scheme requires that a dynamic carrier signal be produced through the modulation of the phase-shifted grating. This can be achieved by a piezoelectric actuator or by modulating the emission frequency of a tunable laser [78, 79]. In this case, the π-shifted structure is modulated with a sinusoidal wave by means of a piezoelectric disk.

4.3.4.1   Phase-Shifted Bragg Gratings as Modulation Elements

In this technique it is used a π-shifted Bragg grating as a modulation element. This structure acts as an ultra narrow tunable filter when submitted to variable strain. The

key requirements are a central notch with a bandwidth much smaller than the wavelength separation between consecutive maxima of the interferometer and a rejection band larger than the FFP bandwidth.

4.3.4.2   Characteristics of PZT Modulation

As shown in

Figure 4.21, light returning from the FFP cavity goes through a π phase-shifted Bragg grating with a spectral transfer function that is modulated by applying tension to the structure with a piezoelectric actuator. In this interrogation system, a piezoelectric (PZT) disk was used and to perform the experiment the PZT was first calibrated. A uniform fibre Bragg grating was placed under tension in the PZT disk where constant voltage values were applied with steps of 5 V. The result is presented in Figure 4.22. An approximately linear dependence of $(3.4 \pm 0.2)\, pm / V$ was obtained.
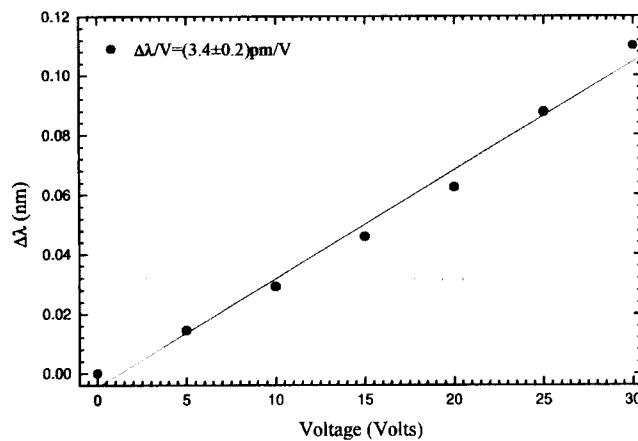
Figure 4.22 – Calibration of the PZT disk as a function of wavelength.

With the phase demodulation technique described in the next section, the π phase-shifted grating is modulated by means of a sinusoidal waveform that is applied to the PZT. To optimize the operation, it is convenient that the frequency of the sine wave to be equal to the resonance frequency of the PZT. In order to choose the right value, the frequency response of the PZT disk was analyzed. To achieve that, a uniform fibre Bragg grating, illuminated by a broadband source, was modulated with a strain sinusoidal waveform derived from the corresponding electric waveform applied to the

PZT. The Bragg wavelength modulation was converted into an optical intensity modulation when the return spectrum from the grating goes through an edge optical filter (WDM coupler); after photodetection, the electrical signal is observed with an electric spectrum analyzer. Figure 4.23 shows the obtained results. The resonance frequency is approximately 2 KHz.
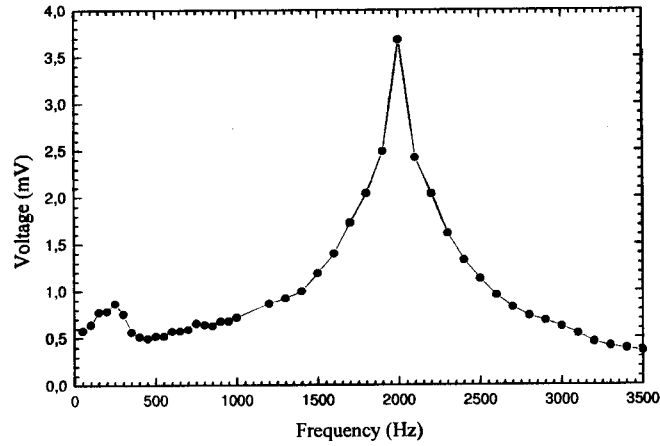
Figure 4.23 – Frequency response of the PZT disk.

4.3.4.3   Principle of Generation of an Electric Heterodyne Carrier

In the proposed interrogation technique, it is necessary to modulate the notch wavelength of the π-shifted grating with the form $\delta\lambda_m \sin(\omega_m t)$. For that a voltage $V_m \sin(\omega_m t)$ is applied to the PZT.

The signal output of the interferometer, after detection and amplification, may be written as

$$V_{out} = V_o + V_a \cos\phi \tag{4.31}$$

where V_o is the mean voltage value of the channeled spectrum of the FFP cavity and ϕ is the phase of the interferometer. The modulation of the π-shifted grating originates a modulation of V_{out} which is equivalent to that originated by an interferometric phase modulation, i.e, all happens as the phase ϕ is given by

$$\phi \equiv \phi(t) = \phi_o + \beta \sin(\omega_m t) \tag{4.32}$$

where

$$\begin{cases} \phi_o = \dfrac{4\pi n L_{FP}}{\lambda_o} \\ \\ \beta = \dfrac{4\pi n L_{FP}}{\lambda_o^2}\, \delta\lambda_m \end{cases} \tag{4.33}$$

Therefore, (4.31) becomes

$$V_{out} = V_o + V_a \cos\!\left[\phi_o + \beta\sin(\omega_m t)\right] \tag{4.34}$$

The information about the measurand that acts on the FFP cavity is in ϕ_o and the purpose is to recover it. Processing this signal in order to eliminate V_o, equation (4.34) can be rewritten as

$$V_{out/norm} = V_a \cos\phi_o\,\cos\!\left[\beta\sin(\omega_m t)\right] - V_a \sin\phi_o\,\sin\!\left[\beta\sin(\omega_m t)\right] \tag{4.35}$$

The spectral content of $V_{out/norm}$ can be better appreciated if the functions $\cos\!\left[\beta\sin(\omega_m t)\right]$ and $\sin\!\left[\beta\sin(\omega_m t)\right]$ are expressed in terms of Bessel functions of order l, where l is an integer

$$\cos\!\left[\beta\sin(\omega_m t)\right] = J_o(\beta) + \sum_{l=1}^{\infty} 2J_{2l}(\beta)\cos(2l\omega_m t) \tag{4.36}$$

$$\sin\!\left[\beta\sin(\omega_m t)\right] = \sum_{l=0}^{\infty} 2J_{2l+1}(\beta)\sin\!\left[(2l+1)\omega_m t\right] \tag{4.37}$$

These equations can be rewritten as

$$\cos\!\left[\beta\sin(\omega_m t)\right] = J_o(\beta) + 2J_2(\beta)\cos(2\omega_m t) + 2J_4(\beta)\cos(4w_m t)\ldots \tag{4.38}$$

$$\sin\!\left[\beta\sin(\omega_m t)\right] = 2J_1(\beta)\sin(\omega_m t) + 2J_3(\beta)\sin(3\omega_m t)\ldots \tag{4.39}$$

and from equation (4.35)

$$V_{out/norm} = V_a J_o(\beta)\cos\phi_o -$$
$$-2V_a J_1(\beta)\sin\phi_o \sin(\omega_m t) +$$
$$+2V_a J_2(\beta)\cos\phi_o \cos(2\omega_m t) -$$
$$-2V_a J_3(\beta)\sin\phi_o \sin(3\omega_m t) + \dots$$

(4.40)

In order to obtain from equation (4.34) a phase-modulated electric carrier, the scheme shown in Figure 4.24 is proposed.
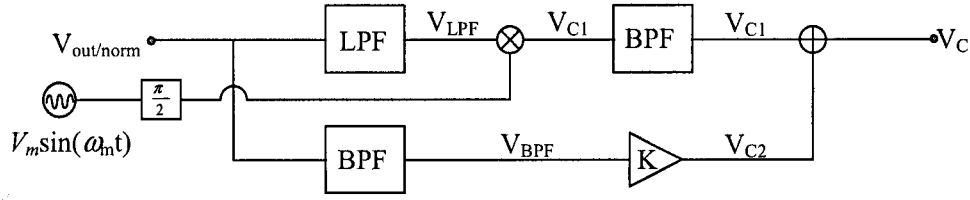
Figure 4.24 – Block diagram of the proposed signal processing scheme used to generate an electric carrier by sinusoidal modulation of the π-shifted grating.

As can be seen, this scheme uses as a second input the same signal that modulates the π-shifted grating, but now with a phase change of $\pi/2$. Considering that the low-pass filter (LPF) has a cutoff frequency below ω_m and the bandpass filters (BPF) are centered at ω_m, then from equation (4.40)

$$V_{LPF} = V_a J_o(\beta)\cos\phi_o$$

(4.41)

and

$$V_{BPF} = -2V_a J_1(\beta)\sin\phi_o \sin(\omega_m t).$$

(4.42)

Therefore, referring to Figure 4.24 and to the electrical sinusoidal waveform that modulated the π-shifted grating with a phase change of $\pi/2$, equation (4.41) becomes

$$V_{C_1} = V_{LPF} \times V_m \cos(\omega_m t) = V_a V_m J_o(\beta)\cos\phi_o \cos(\omega_m t)$$

(4.43)

and V_{BPF} is amplified with gain K such that

$$V_{C_2} = V_{BPF} \times K = -2KV_a J_1(\beta)\sin\phi_o \sin(\omega_m t) \qquad (4.44)$$

By properly setting the gain K of the amplifier such that

$$K = \frac{V_m J_o(\beta)}{2J_1(\beta)} \qquad (4.45)$$

Then the following relation to V_C results:

$$V_C = V_{C_1} + V_{C_2} = V_{OC}\cos(\omega_m t + \phi_o) \qquad (4.46)$$

where $V_{OC} = V_a V_m J_o(\beta) = 2V_a KJ_1(\beta)$.

Clearly, V_C has the form of an electric carrier of angular frequency ω_m and phase ϕ_o which has the information to be recovered. For that, it can be used a lock-in amplifier.

4.3.4.4   Experimental Results and Discussion

The FFP interferometer used in this experiment is the one presented in Figure 4.17. By means of a translation stage, the envelope spectrum of the interferometer is centered with the π-shifted grating. Applying to the PZT a slow ramp voltage up to an amplitude of 50 V, it was observed an interferometric output variation corresponding to a phase variation of 54°, which means an equivalent DC voltage-phase conversion factor of $\approx$ 1°/V. However, the PZT will work at the resonance frequency of 2 KHz. Therefore, from the DC factor and the data shown in Figure 4.23, at this frequency the conversion factor is $\approx$ 8°/V.

The visibility of the interferometric arrangement shown in Figure 4.21 was found to be $\approx$ 24%. This relatively low value is also a consequence of the not negligible spectral width of the π-shifted grating notch ($\approx$ 40 pm) relatively to the spectral fringe periodicity ($\approx$ 170 pm), which results into an integration effect with the decrease of the visibility.

In order to modulate the π-shifted grating, it was applied to the PZT a resonance frequency of 1980 kHz by means of a voltage signal $V_m \sin(\omega_m t)$. To generate a phase change of $\pi/2$, i.e., a voltage signal with the form $V_m \cos(\omega_m t)$, the following circuit was used:
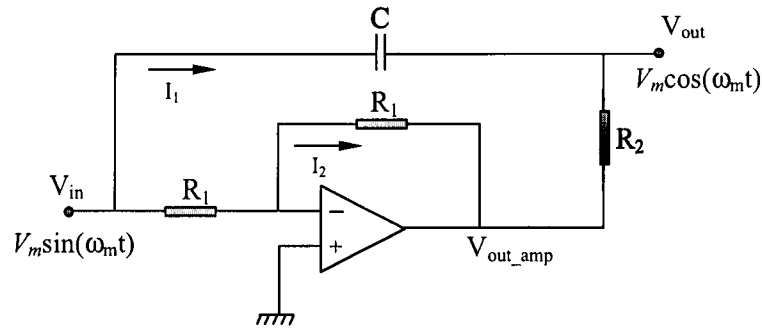
Figure 4.25 – Block diagram of the proposed circuit used to generate a phase change of $\pi/2$ into the electrical sinusoidal waveform that modulates the π-shifted grating.

Using Ohm's Law one can obtain

$$I_1 = \frac{V_{in} - V_{out\_amp}}{R_2 + Z_c} \tag{4.47}$$

and

$$I_2 = \frac{V_{in}}{R_1} = -\frac{V_{out\_amp}}{R_1} \tag{4.48}$$

where

$$Z_c = -\frac{i}{\omega C} \cdot \tag{4.49}$$

From equation (4.48)

$$V_{out\_amp} = -V_{in} \tag{4.50}$$

and since

$$V_{out} = V_{out\_amp} + I_1 R_2 \tag{4.51}$$

the following relation to V_{out} results:

$$V_{out} = V_{in}e^{2i.tg^{-1}\left(\frac{1}{\omega CR_2}\right)}$$ (4.52)

Therefore, the phase change of V_{out} in relation to V_{in} is

$$\theta = 2tg^{-1}\left(\frac{1}{\omega CR_2}\right).$$ (4.53)

Using a capacitor with C = 40 nF, a resistor R_2 = 2 kΩ, and a resonance frequency of 2kHz, the circuit processes at the output a phase change of 90°. In practice, it was used for C a capacitor of 47 nF, and for R_2 a variable resistor with maximum value of 47 kΩ. Figure 4.26 shows the obtained results, where the waveform represented in white is the input voltage signal, V_{in}, with the form $V_m \sin(\omega_m t)$, and the waveform represented in grey is the output voltage signal, V_{out}, of circuit with a phase change of 90°.
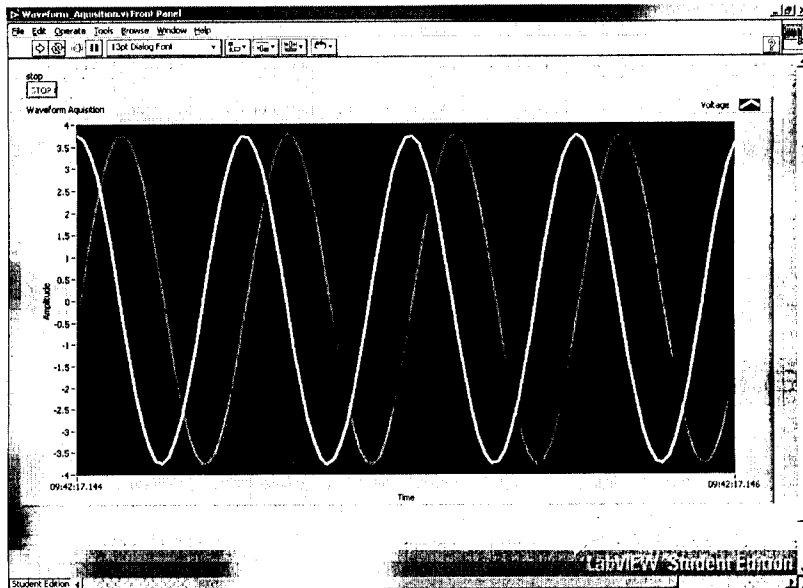
Figure 4.26 – Front panel of the LabView[TM] program used to acquire the input electrical sinusoidal waveform (in white) of the circuit and the output electrical sinusoidal waveform with a phase change of π/2 (in grey).

To implement the signal processing scheme proposed in Figure 4.24, a LabView[TM] based program was developed for this purpose. By means of a DAQ board, the electrical

signals were acquired in real time and converted into digital signals, and processed by LabView™. The results are shown in Figure 4.27.
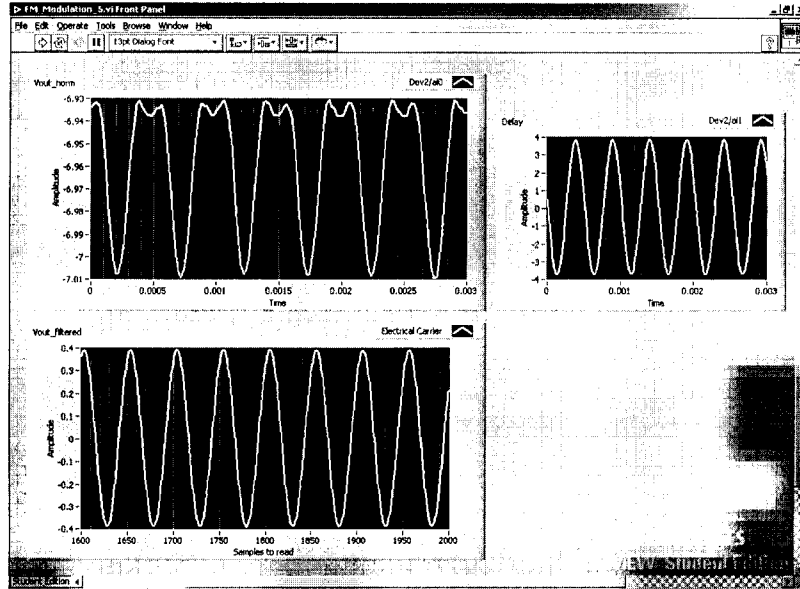
(a)
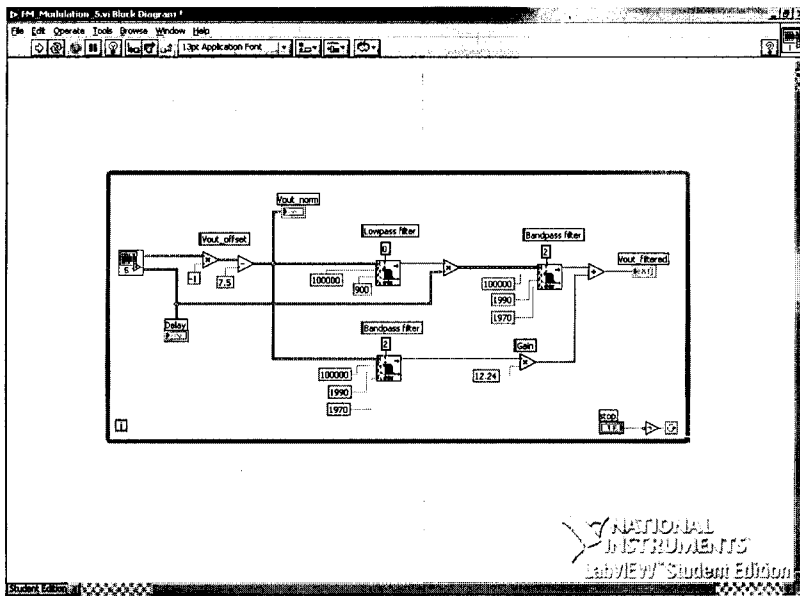
(b)

Figure 4.27 – (a) Front panel and (b) block diagram of the LabView™ program used to acquire the modulated signal output of the interferometer (*Vout_norm*), the output electrical sinusoidal signal with a phase change of π/2 (*Delay*) and the phase-modulated electric carrier (*Vout_filtered*).

The *Vout_norm* graph shows the acquired modulated signal output of the interferometer, the *Delay* graph shows the electrical sinusoidal signal with a phase change of $\pi/2$ at the output of the electronic circuit, and the *Vout_filtered* graph presents the electric carrier after being processed. In the block diagram it is presented the processing scheme proposed in Figure 4.24. The *Vout_norm* and the *Delay* signals come from a secondary program that acquires the signals by means of the DAQ board. The V_o term of equation (4.34) is eliminated in the step *Vout_offset*. In the lowpass filter it is used a cutoff frequency of 900 Hz and in the bandpass filters it is used a low cutoff frequency of 1970 Hz and a high cutoff frequency of 1990 Hz. From equation (4.45), the gain was set to 12.24. Inside of a while loop the program processes the acquired signals in real time until the stop order is used.

When strain is applied to the sensing Fabry-Pérot interferomter, the position of its channeled spectrum relative to the spectral position of the π-shifted grating notch changes, which implies a phase change of the generated electrical carrier. Therefore, the aim was to obtain this phase change versus strain variation. However, the preliminary results obtained came highly corrupted with phase fluctuations, with unclear origin. Due to the timetable required for the dissertation conclusion, there was not enough time to identify this problem and to proceed into the final measurement phase. Understandably, this issue will be the focus of near future work.

5

Short Fibre Tapers

5.1   General Principles of Fibre Tapers

The single mode fibre taper is the basis of many optical fibre devices and has become increasingly important over the last years. Many applications include their use as interferometric devices [80], biosensors [81], fibre dye lasers [82], and for nonlinear research and communications. Tapered fibre devices rely on the interaction of the evanescent field surrounding the fibre waist with the external environment, being an alternative to core-exposed fibres to develop a variety of sensors. The shape of the taper is also of great importance in applications where its deformation has to be rigorously controlled, for example, in directional couples [83, 84], in some sensors based on bending [85, 86] and in beam expanders [87].

Taper components have been modeled by assuming exponential, parabolic, sinusoidal, polynomial or other taper profiles, [88-91]. Here it is assumed the model developed for a taper with exponential profile [92]. The fibre is placed under tension into a particular heat source; the length of the heated region is maintained constant as tapering proceeds and thus forming a taper. Therefore, the taper is a structure comprising a narrow stretched filament – the *taper waist* – between conical tapered sections – the *taper transition* – which are linked to the unstretched fibre. Figure 5.1 shows the general structure of an optical fibre taper.

| Unstretched | Taper | Taper | Taper | Unstretched |
| Fibre | Transition | Waist | Transition | Fibre |
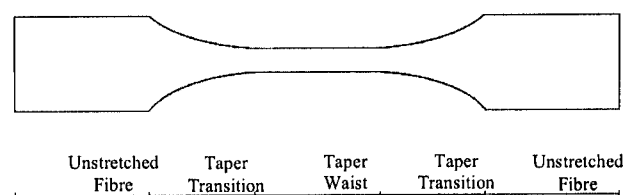
Figure 5.1 – Schematic of an optical fibre taper. [92]

Optically, at the beginning of the taper, the fundamental mode propagates as a core mode. As the fundamental mode enters the taper transition section it begins to spread out into the cladding region until the core-cladding waveguiding structure cannot support the mode. From this point, the mode enters the taper waist as a cladding mode. Here, the cladding and the surrounding medium act as the waveguiding structure. Intuitively, the most sensitive region is the taper waist where the overall diameter is a minimum and hence the evanescent field intensity is most pronounced.

The quantities used to describe the shape of a complete fibre taper are illustrated in Figure 5.2.
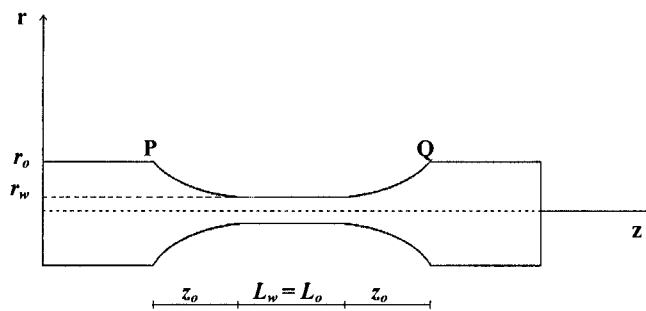
Figure 5.2 – Parameters of an optical fibre taper. [92]

In this simple model it is assumed that a fixed length L_o of fibre is to be uniformly heated and stretched, whereas outside this *hot-zone* the fibre is cold and solid [92]. The taper is formed symmetrically so that the two taper transitions are identical. The radius of the optical fibre without taper is r_o, and the uniform taper waist has length L_w, and radius r_w. Each identical taper transition has a length z_o, and a shape described by a decreasing local radius function $r(z)$, where z is the longitudinal coordinate. The origin of z is at the beginning of each taper transition (points P and Q) and following that notation $r(0) = r_o$ and $r(z_o) = r_w$.

Here it is followed the simplest example of the *constant hot-zone* [92] where $L_w = L_o$. Assuming that the fibre radius follows a decaying exponential profile in the taper sections, it can be written

$$r(z) = r_o \exp\left[-\frac{z}{L_o}\right] \qquad (0 \le z \le z_o) \qquad (5.1)$$

5.2   Fabrication of Short Fibre Tapers

Tapers in optical fibres have been made essentially in two different ways: by etching the fibre cladding [93–95] or by lengthening the fibre by fusion [96–99]. Methods based in fusion range from translating the fibre into a CO_2 laser beam [96], heading a fibre horizontally over a traveling gas burner [97] or by using a fusing-and-pulling treatment with a manual fibre fusion splicer [98, 99]. The short tapers presented in this chapter were fabricated by fusion, where an arc discharge was used while the fibre was placed under tension. Figure 5.3 shows an optical fibre taper.

Figure 5.3 – Optical fibre taper.

The ratio r_w / r_o is approximately 0.65 and corresponds to six arc discharges. Figure 5.4 shows the variation of the fibre radius with the number of arc discharges.
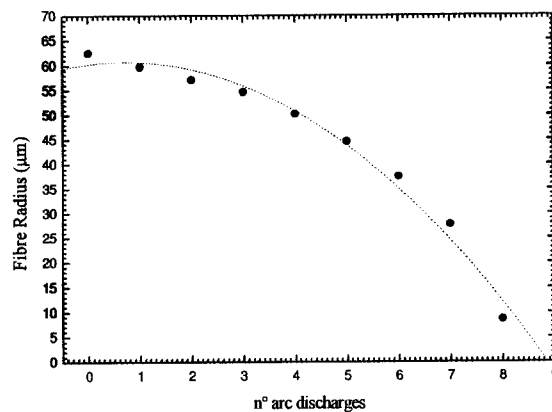
Figure 5.4 – Waist radius variation with number of arc discharges.

Since the fibre is held under tension and is locally heated, the increase of arc discharges will decrease the strength of the fibre leading rapidly to its break. However, this non-linear behavior will depend on the intensity of the arc, the alignment of the fibre and the tension applied.

The losses introduced by the fabrication process are negligible since the tapered fibre transitions satisfy adiabatic criteria [100]. Figure 5.5 shows the result.
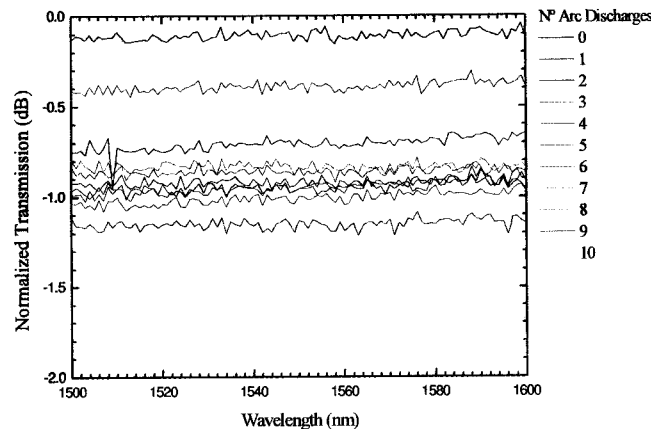
Figure 5.5 – Losses introduced in a taper fabrication process.

One can observe that, between the fourth and the seventh arc discharge, there is a decrease of optical loss. This might be due to the re-coupling of light from the external environment into the core. The last arc discharge originated the entire fusion between the cladding and the core of the fibre and thus forming a very narrow taper. Even for this case the process loss did not exceed 2dB.

5.3 Combination of Fibre Bragg Gratings and Short Tapers

The combination of fibre Bragg gratings with tapers has been widely studied and many tapered structures have been developed for sensing applications. Has mentioned in previous section, tapers in optical fibres are fabricated by etching or by fusion. Etched fibres have a uniform core and thus a constant propagation coefficient that can be modified along the fibre by applying some mechanical stress [101]. Therefore, the main advantage of etched fibres is that they allow fabricating chirped gratings [93–95]. In other hand, in tapers made by fusion the fibre core is tapered as well, and they have non-uniform propagating properties capable to produce non-uniform gratings. In

particular, the combination of two fibre Bragg gratings separated by a short tapered cavity permit to form interesting Fabry-Perot interferometers [99].

An optical fibre with an arc discharge or with a short taper has non-uniform propagating properties due to the fibre geometry changes in that section but also due to the effective index variation. The fundamental propagation mode has a non-uniform effective index $n_{eff}(z)$ because the fibre radius decreases along the taper and, consequently, the grating as a variable Bragg wavelength. For small variations of the effective index along the fibre, the Bragg wavelength along the grating can be expressed in the following form

$$\lambda_B(z) = \lambda_B(0)\left[1 + \frac{\Delta n_{eff}(z)}{n_{eff}(0)}\right] \tag{5.2}$$

where $\lambda_B(0)$ and $n_{eff}(0)$ are, respectively, the Bragg wavelength and the effective index at the beginning of the grating, i.e.,

$$\lambda_B(0) = 2\Lambda n_{eff}(0) \tag{5.3}$$

and $\Delta n_{eff}(z)$ is the index variation along the grating

$$\Delta n_{eff}(z) = n_{eff}(z) - n_{eff}(0), \tag{5.4}$$

Equation (5.2) can be written as

$$\lambda_B(z) = 2\Lambda n_{eff}(z). \tag{5.5}$$

The effective index of the core mode, $n_{eff}(z)$, is given as a function of the propagating wavelength, the geometry of the fibre and the refractive index of the core material [102]. For a weakly guiding step-index fibre, a geometric-optics approximation is generally used to yield the effective indices of the core and the cladding modes [103]. Because a single-mode fibre can support only the LP_{01} mode, the equation for the core mode is

$$\frac{2\pi}{\lambda}D_{core}\left[(n_{core})^2 - (n_{eff})^2\right]^{1/2} - \frac{\pi}{2} = 2\cos^{-1}\left[\frac{(n_{core})^2 - (n_{eff})^2}{(n_{core})^2 - (n_{clad})^2}\right]^{1/2} \tag{5.6}$$

where D_{core} is the diameter of the core, and n_{core} and n_{clad} are the refractive index of the core and cladding materials, respectively. This equation is solved numerically and gives the relation between the core radius and the effective index. Hence, using equation (5.5) the dependence of the Bragg wavelength with the core diameter can be determined. Figure 5.6 shows the dependence of the effective index of the core mode with the diameter of the core.
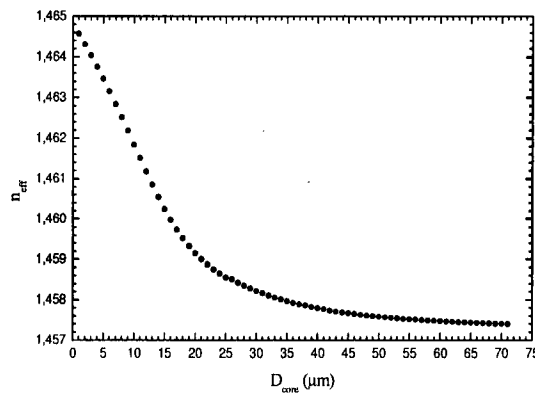
Figure 5.6 – Effective index variation of the core mode with the diameter of the core.

In this section it is presented two optical fibre structures based on the combination of a short taper and a single Bragg grating (TFBG). The purpose is to demonstrate the differences between fabricating a short fused taper in a fibre Bragg grating (TFBG$_1$) and a Bragg grating in a tapered core fibre (TFBG$_2$).

The tapered structures were interrogated by a tunable laser source and the optical spectra were acquired by a LabView[TM] based program developed for this purpose. Each optical signal was converted into an electrical signal by a photodetector and, after amplification, converted into a digital signal in order to be acquired by the software. To research the structures TFBG$_1$ it were used two Bragg gratings, with 10 mm length, written in hydrogen loaded fibre; at the middle of the gratings, in one of them it was induced an arc discharge and in the other one a short fused taper (8 arc discharges). For the TFBG$_2$ structures it was used two branches of optical fibre where, first, it was applied to one of the fibres an arc discharge, while in another fibre was fabricated a short fused taper (8 arc discharges). After being hydrogen loaded, a single Bragg grating was written in these two fibres, noting that the arc discharge and the short fused taper should be at the center of each grating. The optical spectra of the structures TFBG$_1$ and TFBG$_2$ are shown in Figure 5.7(a) and Figure 5.7(b), respectively.
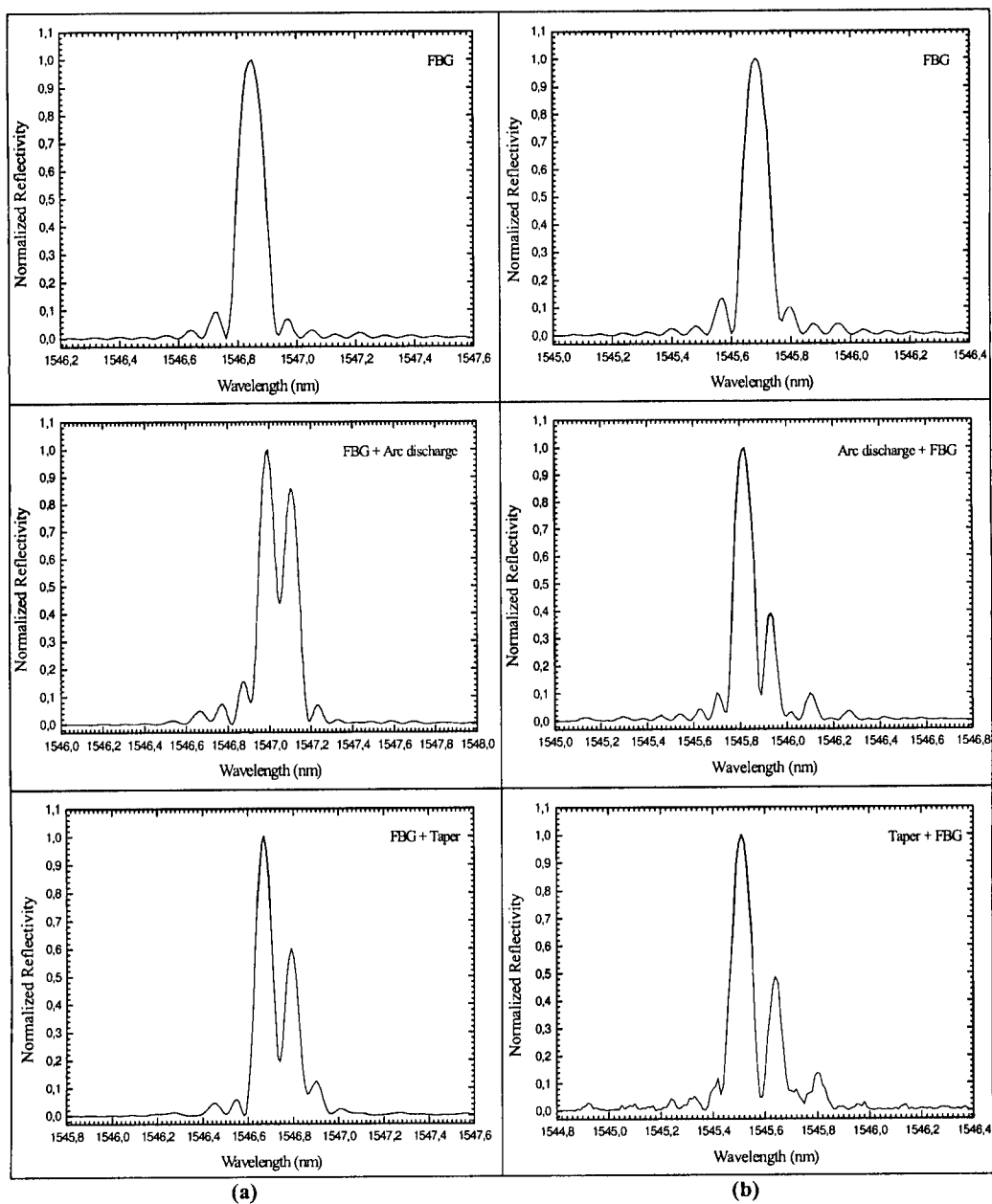
Figure 5.7 – Optical spectra of: (a) a fibre Bragg grating, a fibre Bragg grating with an arc discharge and a fibre Bragg grating with a short fused taper; (b) a fibre Bragg grating, a Bragg grating written in a fibre with an arc discharge and a Bragg grating written in a tapered core fibre.

In the TFBG₁ structure, inducing one arc discharge or a short fused taper will change significantly the average effective index, which explains the small difference for $\{\Delta n_{eff}\ (Taper) - \Delta n_{eff}\ (Arc)\}$, as shown in Table 1. The variations of the effective indices were determined by calculating the effective index (equation 2.26) of the two

wavelength peaks in each spectrum utilizing the Bragg relationship. In both cases (electric discharge and arc), the spectra shown in Figure 5.7(a) indicates that the grating is essentially destroyed in the arc/taper section, generating a true fibre Fabry-Pérot. The mirrors are the two unaffected lengths of the initial grating in each side of the arc/taper section. Because these lengths are smaller than the initial Bragg length, their spectral bandpass signatures are wider, which is confirmed by the experimental results.

In what concerns the $TFBG_2$ structures, the arc discharge and the fabrication of the short fused taper changes not only the effective refractive index in the region, but also eliminates any residual photosensitivity that could exist in the fibre. However, after the fibre undergoes the hydrogen loading process, it is feasible afterwards to write a Bragg grating in that region. What was observed and shown in Figure 5.7(b) is that the grating spectral signature has internal structure, a feature indicative of the presence of interferometric effects. These are certainly related with the variation of the fibre material refractive index under the discharge/taper fabrication procedure. The important difference relatively to the reverse order sequence (grating written first and discharge/taper fabrication afterwards), is that now there is a continuous grating with a constant (in first order) refractive index amplitude modulation on the top of an average refractive index value, that changes in the device central region due to the previous discharge/taper fabrication operation. This progressive change introduces a progressive variation on the grating phase, resulting into a spectral signature typical of a phase-shifted Bragg grating structure.

Another relevant difference is reflected on the largest value for Δn_{eff} *(Taper)* - Δn_{eff} *(Arc)*, which is 0.17 for the $TFBG_2$ structure compared with 0.05 for the $TFBG_1$. The explanation for this will probably be on the different photosensitivity level of the fibre under hidrogenization after exposure to the fibre temperature of the arc discharge.

Gratings	Δn_{eff} (Arc)	Δn_{eff} (Taper)	Δn_{eff} (Taper) - Δn_{eff} (Arc)
$TFBG_1$	1.07×10^{-4}	1.12×10^{-4}	0.05
$TFBG_2$	1.03×10^{-4}	1.2×10^{-4}	0.17

Table 5.1 – Effective index variations for $TFBG_1$ and $TFBG_2$.

In conclusion, fabricating a short fused taper in a fibre Bragg grating ($TFBG_1$) or a Bragg grating in a tapered core fibre ($TFBG_2$) originates fibre structures which are conceptually different. $TFBG_1$ is a Fabry-Perot interferometer because the arc discharge

erases the grating in the taper section; in practice, the structure will be formed by two shorter Bragg gratings separated by a tapered cavity. In TFBG$_2$ the grating is written in the taper section where the effective index is different and thus causing a phase change. Due to that, TFBG$_2$ can be seen as a phase-shifted tapered structure.

5.4 Sensing Characteristics

In previous section it was demonstrated that a Fabry-Perot cavity can be developed by performing a short fused taper in the middle of a fibre Bragg grating. Basically, this tapered structure will act as a two-wave interferometer (see Figure 5.8), formed by two shorter gratings, that are the mirrors, separated by a short tapered cavity. As already seen in section 2.6, the equivalent reflection of a uniform fibre Bragg grating with total length L_T, appears at the middle of the structure $(L_T / 2)$ which corresponds in this case to the position of each mirror and hence where the two waves seem to be reflected. Assuming that each shorter grating has length L_1 and the fused taper has length L_2, then the cavity length is given by $L = L_1 + L_2 = \frac{1}{2}(L_2 + L_T)$.
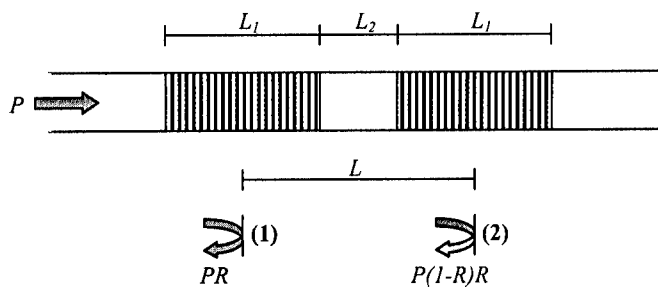
Figure 5.8 – Schematic of a two wave interferometer.

The phase difference between the two waves reflected in the two mirrors is given by

$$\phi_{12} = \frac{4\pi nL}{\lambda} \tag{5.7}$$

where n is the effective index of the cavity, L is the cavity length and λ is the Bragg wavelength. Inside the grating spectral profile, defined by a normalized function $E(\lambda)$,

there is a channel spectrum due to the interferometer, with a fringe spectral periodicity, $\delta\lambda$, given by

$$\phi_{12} = -\frac{4\pi nL}{\lambda^2}\,\delta\lambda; \quad \delta\phi_{12} = 2\pi \Rightarrow |\,\delta\lambda\,| = \frac{\lambda^2}{2nL}. \qquad (5.8)$$

The intensity of the total reflected wave is

$$I_T = I_{12} = E(\lambda)\,PR\left[1 + (1-R)^2\right]\cdot\left[1 + \frac{2(1-R)}{1+(1-R)^2}\cos\phi_{12}\right] \qquad (5.9)$$

where P is the incident optical power and R is the reflectivity of each grating section.

Inducing two short fused tapers equally spaced $(L_T/3)$ in the fibre Bragg grating, will split the grating into three shorter gratings and thus forming two concatenated Fabry-Perot cavities, with the same length L, as it is shown in Figure 5.9.
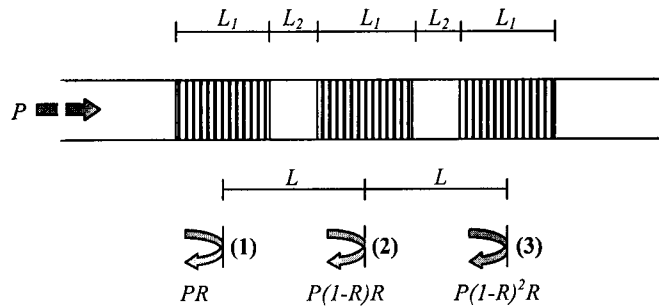
Figure 5.9 – Schematic of two concatenated fibre Bragg gratings based Fabry-Pérot cavities with length $L = \frac{1}{3}(L_2 + L_T)$.

For each pair of mirrors the phase difference between the corresponding reflected waves is given by the following relations

$$\phi_{12} = \phi_{23} = \frac{4\pi nL}{\lambda} \qquad (5.10a)$$

$$\phi_{13} = \frac{8\pi nL}{\lambda} \qquad (5.10b)$$

The interference terms are then the following

$$I_{12} = E(\lambda)PR\left[1+(1-R)^2\right] \cdot \left[1+\frac{2(1-R)}{1+(1-R)^2}\cos\phi_{12}\right]$$ (5.11a)

$$I_{13} = E(\lambda)PR\left[1+(1-R)^4\right] \cdot \left[1+\frac{2(1-R)^2}{1+(1-R)^4}\cos\phi_{13}\right]$$ (5.11b)

$$I_{23} = E(\lambda)PR(1-R)^2\left[1+(1-R)^2\right] \cdot \left[1+\frac{2(1-R)}{1+(1-R)^2}\cos\phi_{23}\right]$$ (5.11c)

resulting into a total reflected optical power given by

$$I_T = I_{12} + I_{13} + I_{23}$$ (5.12)

where P is the incident optical power and R is the reflectivity.

Inducing three short fused tapers equally spaced $(L_T/4)$ in the fibre Bragg grating, will split the grating into four shorter gratings and thus forming three concatenated Fabry-Pérot cavities with the same length.
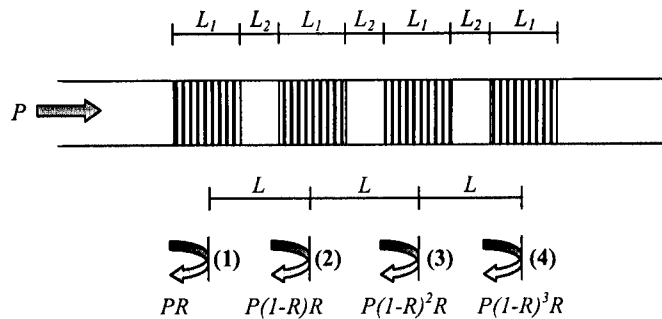
Figure 5.10 – Schematic of three concatenated fibre Bragg grating based Fabry-Pérot cavities with length $L = \frac{1}{4}(L_2 + L_T)$.

For each pair of mirrors the phase difference between the corresponding reflected waves is given by the following relations

$$\phi_{12} = \phi_{23} = \phi_{34} = \frac{4\pi nL}{\lambda} \qquad (5.13a)$$

$$\phi_{13} = \phi_{24} = \frac{8\pi nL}{\lambda} \qquad (5.13b)$$

$$\phi_{14} = \frac{12\pi nL}{\lambda} \qquad (5.13c)$$

The corresponding interference terms are expressed as

$$I_{12} = E(\lambda) PR \left[1 + (1-R)^2\right] \cdot \left[1 + \frac{2(1-R)}{1+(1-R)^2} \cos \phi_{12}\right] \qquad (5.14a)$$

$$I_{13} = E(\lambda) PR \left[1 + (1-R)^4\right] \cdot \left[1 + \frac{2(1-R)^2}{1+(1-R)^4} \cos \phi_{13}\right] \qquad (5.14b)$$

$$I_{23} = E(\lambda) PR (1-R)^2 \left[1 + (1-R)^2\right] \cdot \left[1 + \frac{2(1-R)}{1+(1-R)^2} \cos \phi_{23}\right] \qquad (5.14c)$$

$$I_{14} = E(\lambda) PR \left[1 + (1-R)^6\right] \cdot \left[1 + \frac{2(1-R)^3}{1+(1-R)^6} \cos \phi_{14}\right] \qquad (5.14d)$$

$$I_{24} = E(\lambda) PR (1-R)^2 \left[1 + (1-R)^4\right] \cdot \left[1 + \frac{2(1-R)^2}{1+(1-R)^4} \cos \phi_{24}\right] \qquad (5.14e)$$

$$I_{34} = E(\lambda) PR (1-R)^4 \left[1 + (1-R)^2\right] \cdot \left[1 + \frac{2(1-R)}{1+(1-R)^2} \cos \phi_{34}\right] \qquad (5.14f)$$

resulting for the total reflected optical power

$$I_T = I_{12} + I_{13} + I_{14} + I_{23} + I_{24} + I_{34}. \qquad (5.15)$$

Figure 5.11 shows the spectral responses of these three tapered Fabry-Perot structures (TFP) that were obtained experimentally. Each grating has 10 mm length and the fused tapers have ≈ 400 μm.

(a)

(b)

(c)
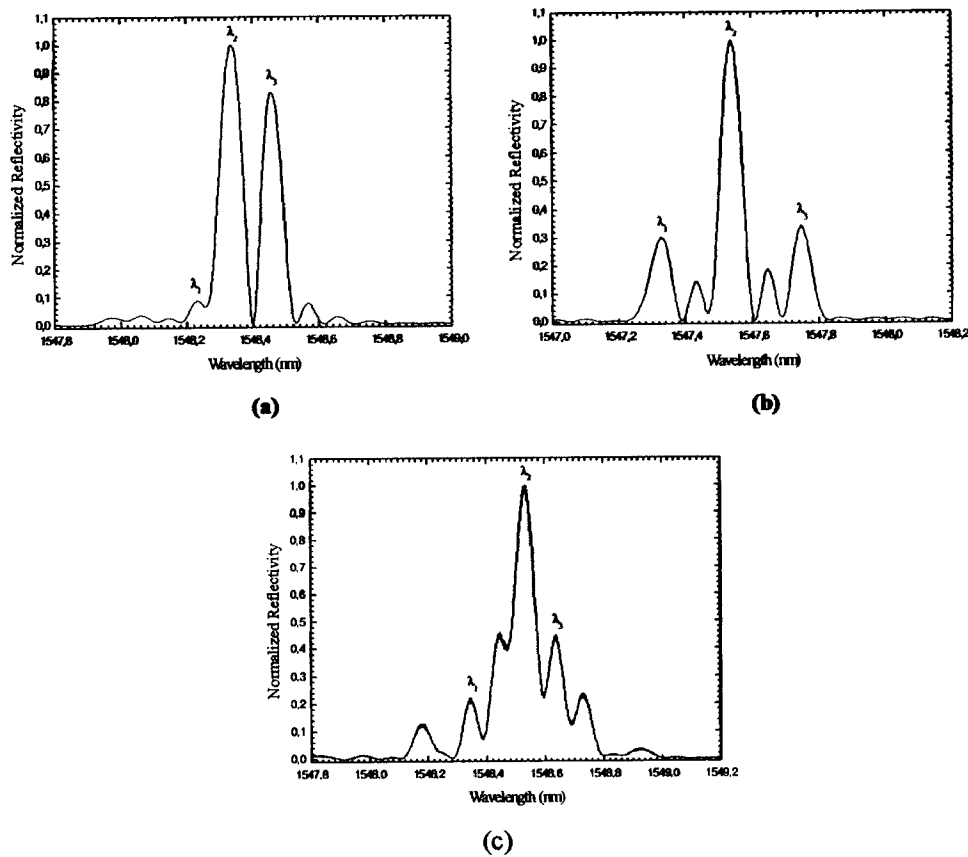
Figure 5.11 – Optical spectrum of (a) a fibre Bragg grating with a fused taper
(TFP₁); (b) a fibre Bragg grating with two short fused tapers (TFP₂); and (c) a
fibre Bragg grating with three short fused tapers (TFP₃).

In Figure 5.11(a) it is represented a TFP structure where one short fused taper was
induced in the middle of a fibre Bragg grating (TFP$_1$); in Figure 5.11(b) two equally
spaced short fused tapers were induced in a fibre Bragg grating (TFP$_2$), while Figure
5.11(c) refers to the case of three equally spaced short fused tapers. Each cavity
presented in the TFP structures generates a channeled spectrum in the reflection band,
and the combination of them results into a rich spectral structure with sharper peaks
relatively to the case of a single cavity (TFP$_1$). The complexity of the (TFP$_3$) spectral
response is due to the multiple interference terms inherent to this structure. The
periodicity of the fringes is 0.12 nm, 0.11 nm and 0.10 nm for TFP$_1$, TFP$_2$ and TFP$_3$,
respectively. The increase of the bandwidth envelope of each TFP is due to the presence
of gratings with shorter lengths. The corresponding values are approximately 0.2 nm,
0.4 nm and 0.6 nm.

These TFP structures were submitted to strain and temperature in order to analyze their behavior to these physical parameters. Figure 5.12 shows the wavelength variation of the TFP structures spectral responses as a function of strain.
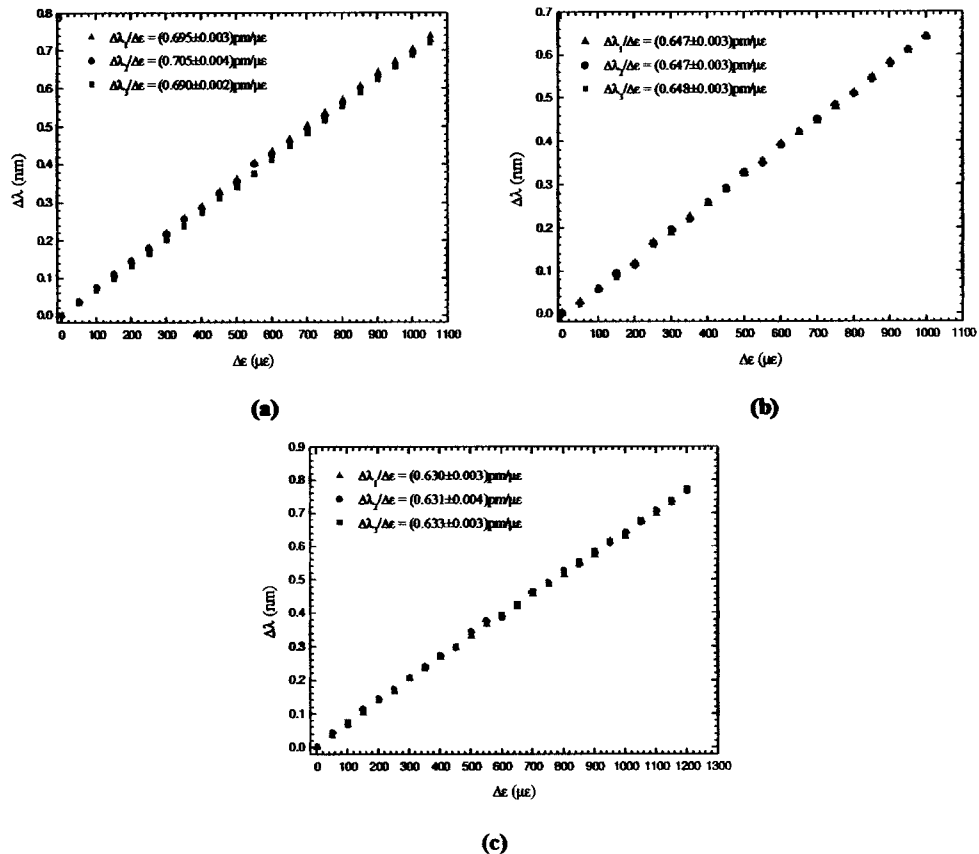
Figure 5.12 – Wavelength shift versus applied strain of the peaks identified as λ_1, λ_2 and λ_3 in Figure 5.10 for: (a) TFP_1, (b) TFP_2 and (c) TFP_3.

It can be observed that the obtained sensitivities are inferior to those associated with a uniform Bragg grating (1 pm/$\mu\epsilon$). The stress induced by strain will be mainly applied in the taper region because it has smaller diameter than the rest of the fibre and, due to that, the Bragg grating will have less sensitivity to this parameter – this aspect will be analyzed later in section 5.5.

As Table 5.2 shows, there is a slightly decrease of the strain sensitivity values with the increase of the number of tapers in each Bragg grating structure. This is due to the large fraction of the fibre length in the sensing structure with reduced diameter.

	$\Delta\lambda/\Delta\varepsilon$ (pm/$\mu\varepsilon$)		
TFP Structure	λ_1	λ_2	λ_3
TFP_1	0.695	0.705	0.690
TFP_2	0.647	0.647	0.648
TFP_3	0.630	0.631	0.633

Table 5.2 – Strain coefficients of the TFP structures.

In other hand, the envelope of each TFP structure moves slower than the corresponding peaks. This turns out from the observation of the peak power changes shown in Figure 5.13 associated with the variation of the optical path of the cavity (the peaks associated with λ_1 and λ_3 are normalized to the λ_2 peak which is attributed the unitary value). The applied strain increases nL, but in order to keep the 2π phase difference between the reflected waves, the wavelength must also increase. By the envelope effect, the spectral peak associated to λ_1 increases and the spectral peak associated to λ_3 decreases. However, the envelope shifts as well. If the fringes and the envelope had a synchronous movement, then no peak power variations would be observed. The reason that λ_1 increases and λ_3 decreases has to be with the fact that the fringes move faster than the envelope. Anyway, its continuous presence is a clear indication of the stated envelope displacement with strain. Indeed, in the case of TFP_1, 1000 $\mu\varepsilon$ corresponds to a wavelength shift of 0.7 nm, which is much higher than the FWHM of the envelope ($\sim$ 0.2 nm). Therefore, if the envelope did not move the fringes would move out of it and soon would not be visible.
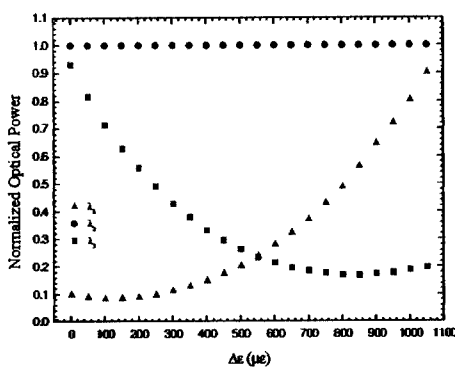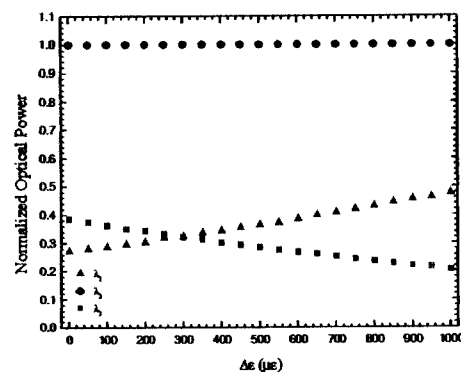
(a)   (b)
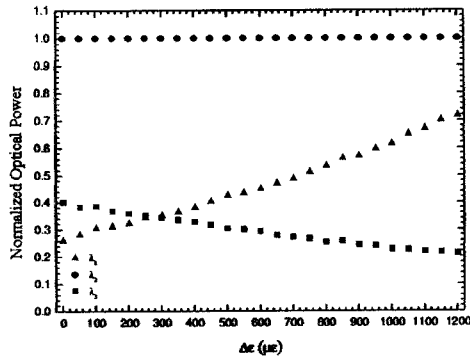
(c)

Figure 5.13 – Amplitude of the peaks identified as λ_1 and λ_3 in Figure 5.10 normalized to the λ_2 peak (which is attributed the unitary value) versus applied strain for: (a) TFP$_1$, (b) TFP$_2$ and (c) TFP$_3$.

In the case of TFP$_2$ and TFP$_3$, on can observe similar results to the ones obtained for TFP$_1$: the spectral peak associated to λ_1 increases and the spectral peak associated to λ_3 decreases. However, there is a linear response that is not observed in TFP$_1$. This might be associated to different locations of the optical peaks relative to the envelope or by finding more linear regions in wavelength due to a larger spectral width of the envelope.

Figure 5.14 shows the wavelength variation of the peaks of the TFP structures spectral response as a function of temperature. It can be observed that the obtained sensitivities are similar to those associated with a uniform Bragg grating. The amplitude of the peak identified as λ_1 in Figure 5.11(a) is not given due to its negligible amplitude in the situation of non applied strain – Figure 5.14(a).
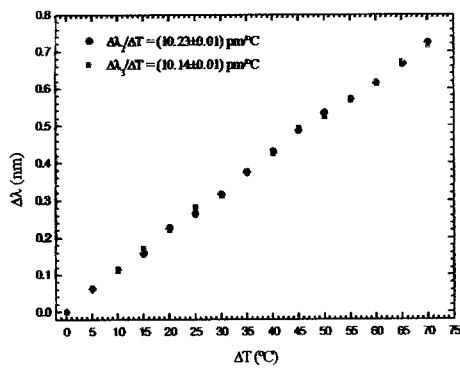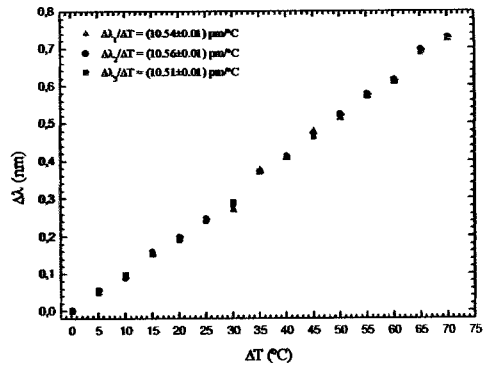
(a)   (b)
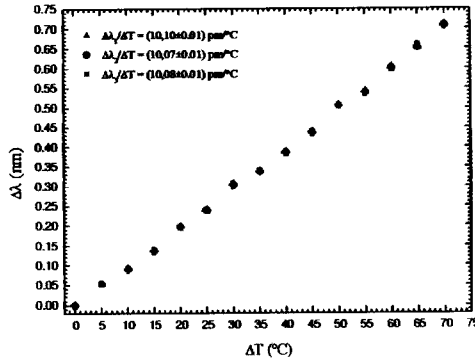
(c)

Figure 5.14 – Wavelength shift versus temperature variation of the peaks identified as λ_1, λ_2 and λ_3 in Figure 5.10 for: (a) TFP$_1$, (b) TFP$_2$ and (c) TFP3.

Table 5.3 presents the values corresponding to the temperature sensitivities of the optical peaks of each TFP structure.

TFP Structure	$\Delta\lambda/\Delta T$ (pm/°C)		
	λ_1	λ_2	λ_3
TFP_1	–	10.23	10.14
TFP_2	10.54	10.56	10.51
TFP_3	10.10	10.07	10.08

Table 5.3 – Temperature coefficients of the TFP structures.

An interesting feature of these TFP structures is that the amplitude of the peaks of their spectral functions does not change with temperature. This can be confirmed from observation of Figure 5.15 (again, the peaks associated with λ_1 and λ_3 are normalized to the λ_2 peak which is attributed the unitary value).
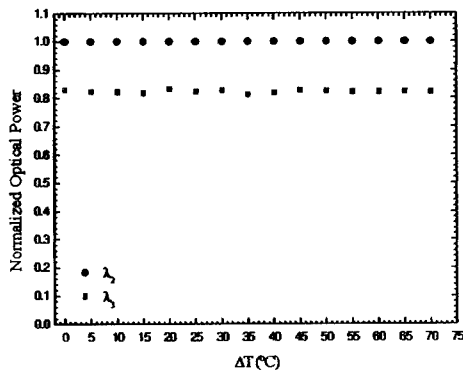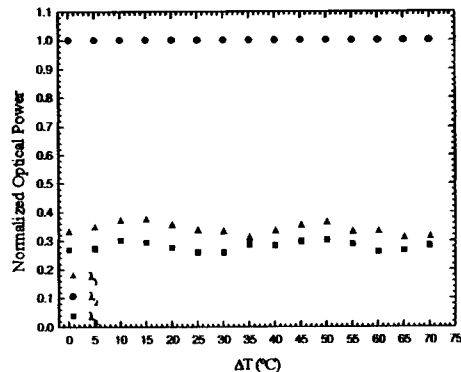
(a)   (b)
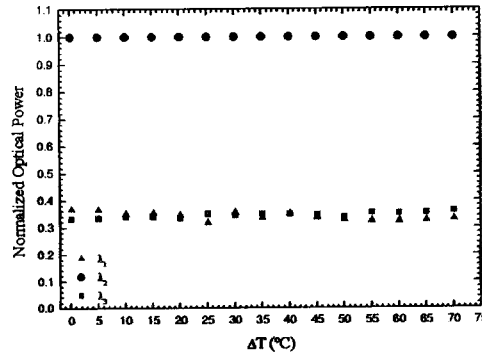
(c)

Figure 5.15 – Amplitude of the peaks identified as λ_1 and λ_3 in Figure 5.10 normalized to the λ_2 peak (which is attributed the unitary value) versus temperature variation for: (a) TFP_1, (b) TFP_2 and (c) TFP_3.

In this case, the envelope of each TFP structure moves synchronously with the corresponding peaks. This can be confirmed through a simple analysis of the relevant equations. Using the Bragg condition (equation 2.26) and the phase term given by equation (5.7), one can obtain the following relations

$$\lambda_B = 2n\Lambda \Rightarrow \partial\lambda_B = \lambda_B \frac{\partial n}{n} \tag{5.16}$$

$$\begin{cases} \partial\phi = \frac{4\pi L}{\lambda}\partial n \\ \partial\phi = -\frac{4\pi n L}{\lambda^2}\partial\lambda \end{cases} \Rightarrow \partial\lambda = \lambda\frac{\partial n}{n} \tag{5.17}$$

These equations show that the displacement of the envelope and the displacement of the internal interferometric fringes, as a function of the refractive index variation, are the same.

One consequence of this result is that, the determination of the amplitude of certain peaks of the spectral transfer function of these structures permits temperature independent strain measurement, a feature which is not exhibited by many sensing heads oriented to measurement of strain. Also, power referencing is easily accessible with these sensing configurations. Additionally, combining the monitoring of the amplitude of those peaks with the wavelength shift of any of them turns out possible the simultaneous measurement of strain and temperature, which adds extra flexibility to the utilization of these TFP structures.

The results presented addressed the sensing characteristics of the structures formed by inducing a short fused taper in a fibre Bragg grating (taper Fabry-Pérot – TFP, $TFBG_1$ in the notation of section 5.3). As indicated in section 5.3, another possibility is feasible, namely the fabrication of a fibre Bragg grating in a tapered core fibre ($TFBG_2$), which also exhibit interesting sensing characteristics. The remaining of this section deals with the sensing characteristics of this type of structure.

Figure 5.16 shows the spectral responses of three tapered fibre Bragg grating structures that were obtained experimentally. Each grating has ≈ 10 mm length and the fused tapers have ≈ 400 µm. Figure 5.16(a) represents the case of a Bragg grating written over a short fibre taper ($TFBG_{2a}$); Figure 5.16(b) is relative to a Bragg grating written over two short fibre tapers ($TFBG_{2b}$), and Figure 5.16(c) shows the spectrum of a Bragg grating written over three short fibre tapers ($TFBG_{2c}$).

(a)

(b)

(c)
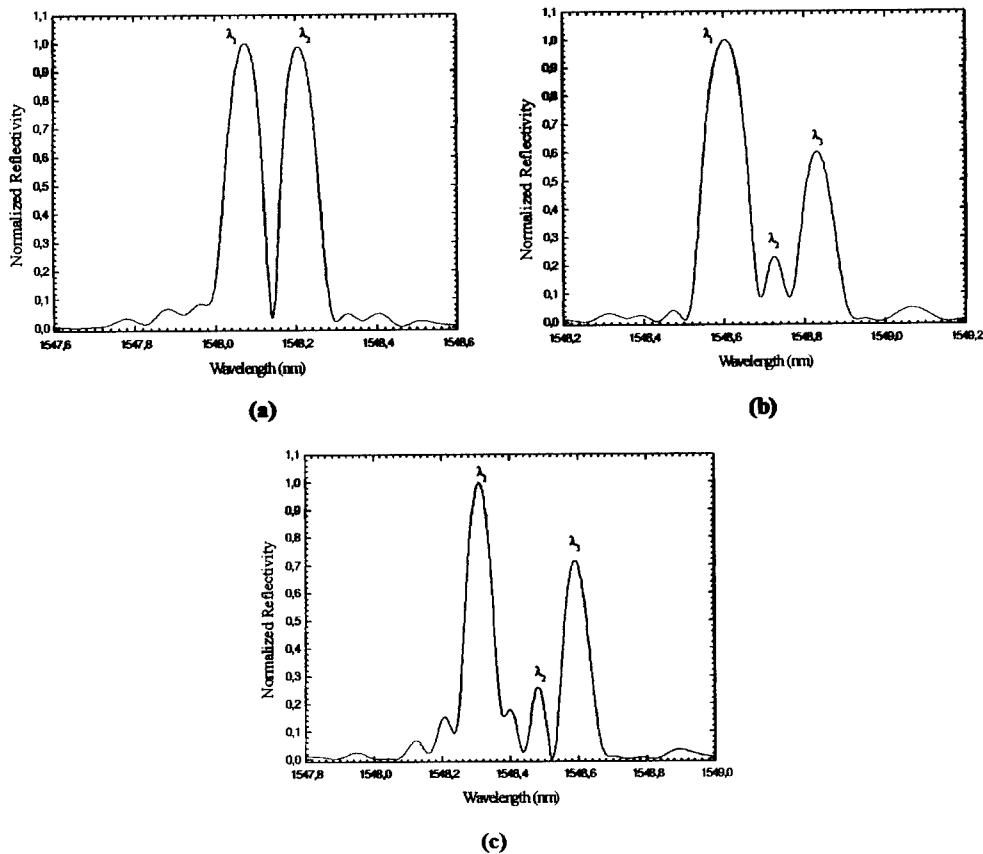
Figure 5.16 – Optical spectrum of: (a) a Bragg grating written over a short fibre taper ($TFBG_{2a}$); (b) a Bragg grating written over two short fibre tapers equally spaced ($TFBG_{2b}$); and (c) a Bragg grating written over three short fibre tapers equally spaced ($TFBG_{2c}$).

These TFBG structures were submitted to strain and temperature in order to analyze their behavior to these physical parameters. Figure 5.17 shows the strain induced wavelength variation of the TFBG$_2$ spectral responses.
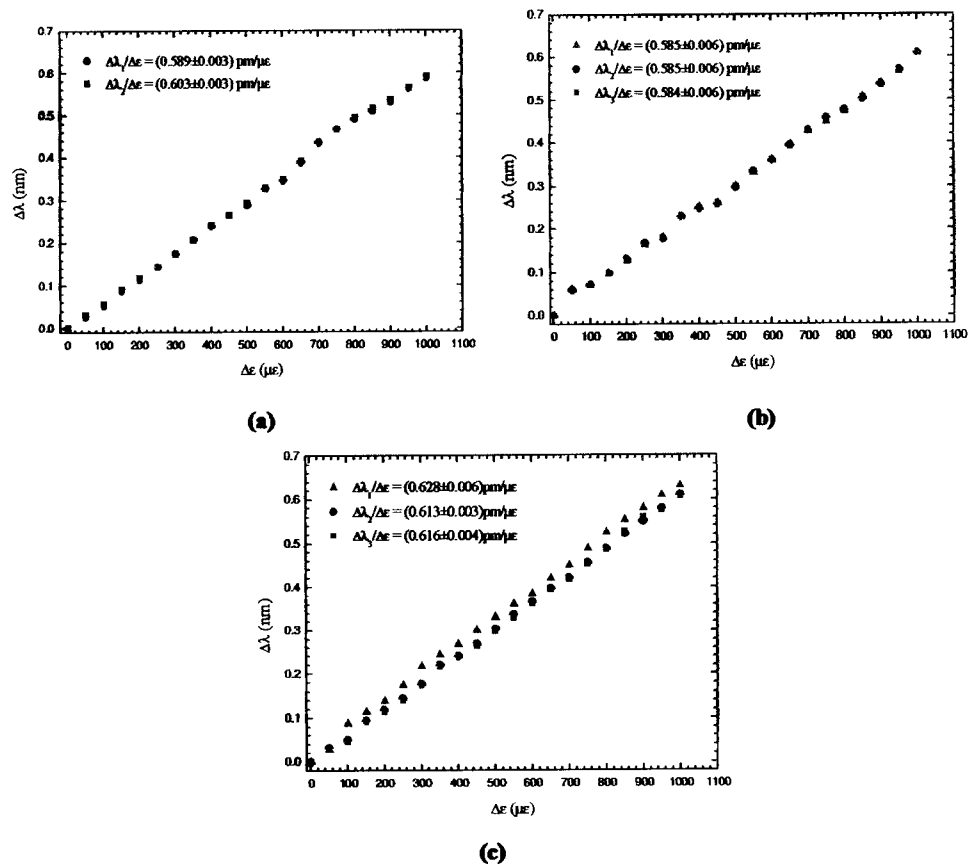
Figure 5.17 – Wavelength shift versus applied strain of the peaks identified as λ_1, λ_2 and λ_3 in Figure 5.15 for: (a) TFBG$_{2a}$, (b) TFBG$_{2b}$, and (c) TFBG$_{2c}$.

It can be observed that the obtained sensitivities are inferior to those associated with a uniform Bragg grating (1 pm/µε). This happens because, as in the case of the TFBG$_1$ structures, the strain induced by the applied stress will be mainly concentrated in the taper region due to its smaller diameter. As shown in Table 5.4, the increase of the number of taper sections along each Bragg grating structure does not affect significantly the wavelength sensitivity to strain of the optical peaks, which is residually slower when compared with the values obtained for the TFBG$_1$ case (Table 5.2).

	$\Delta\lambda/\Delta\varepsilon$ (pm/$\mu\varepsilon$)		
TFP Structure	λ_1	λ_2	λ_3
TFP_1	-	0.589	0.603
TFP_2	0.585	0.585	0.584
TFP_3	0.628	0.613	0.616

Table 5.4 – Strain coefficients of the $TFBG_2$ structures.

In other hand, the envelope of each $TFBG_2$ structure move slower than the corresponding peaks. This result turns out from the changes in the peak power shown in Figure 5.18 caused by a change of the optical path. By the envelope effect, the spectral peak associated to λ_1 increases and the spectral peak associated to λ_3 decreases. However, the envelope shifts as well. The reason that λ_3 increases and λ_2 decreases has to be with the fact that the fringes move faster than the envelope. Again, these conclusions are similar to those obtained for the $TFBG_1$ case.

(a)   (b)

(c)
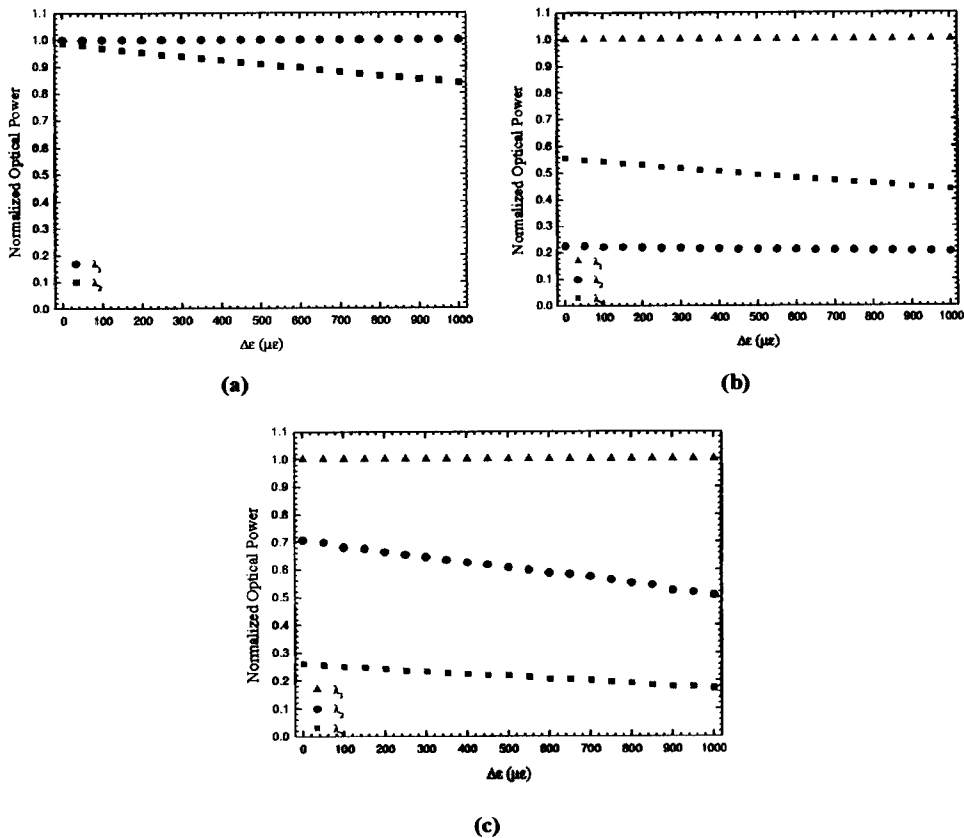
Figure 5.18 – Amplitude of the peaks identified as λ_1, λ_2 and λ_3 in Figure 5.15 versus applied strain for: (a) $TFBG_{2a}$, (b) $TFBG_{2b}$ and (c) $TFBG_{2c}$.

Figure 5.19 shows the wavelength variation of the peaks of the TFBG$_2$ structures spectral response as a function of temperature. It can be observed that the obtained sensitivities are similar to those associated with a uniform Bragg grating. The results are summarized in Table 5.5.

(a)

(b)

(c)
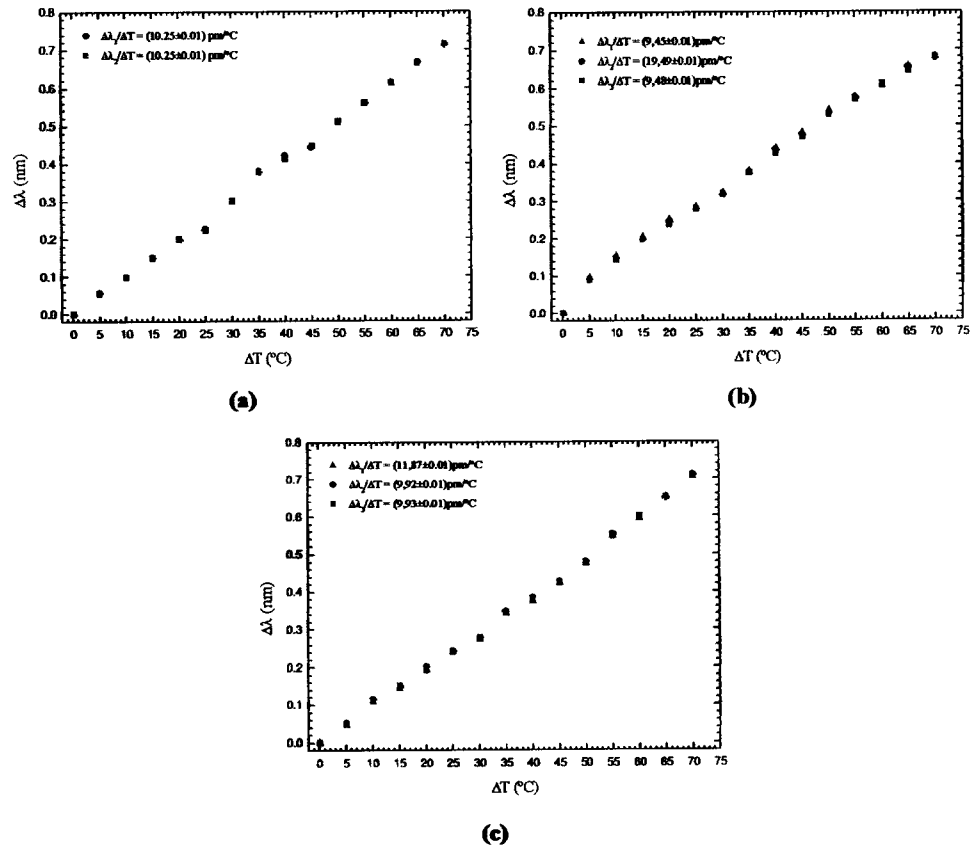
Figure 5.19 – Wavelength shift versus temperature variation of the peaks identified as λ_1, λ_2 and λ_3 in Figure 5.15 for: (a) TFBG$_{2a}$, (b) TFBG$_{2b}$ and (c) TFBG$_{2c}$.

	$\Delta\lambda/\Delta T$ (pm/°C)		
TFP$_2$ Structure	λ_1	λ_2	λ_3
TFP$_{2a}$	----	10.25	10.25
TFP$_{2b}$	9.45	9.49	9.48
TFP$_{2c}$	11.87	9.92	9.93

Table 5.5 – Temperature coefficients of the TFBG$_2$ structures.

Again, the amplitude of the peaks of the TFBG$_2$ structures spectral function does not change with temperature. This can be confirmed from observation of Figure 5.20.
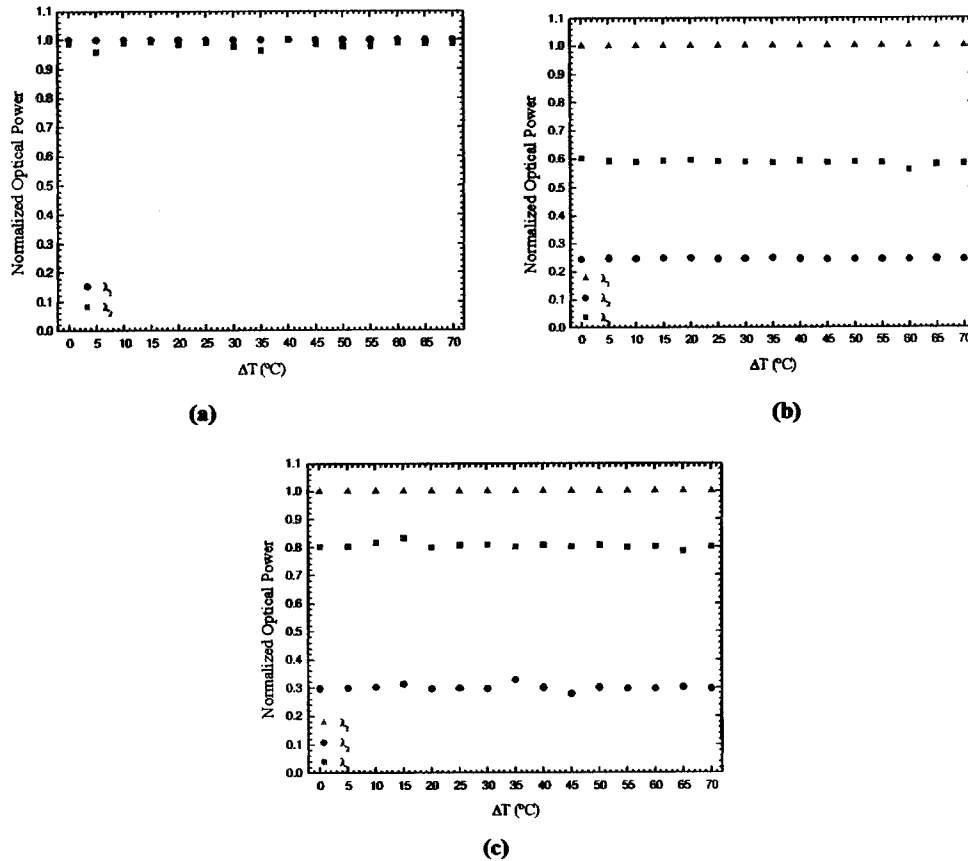
Figure 5.20 – Amplitude of the peaks identified as λ_1, λ_2 and λ_3 in Figure 5.15 versus temperature variation for (a) TFBG$_{2a}$, (b) TFBG$_{2b}$ and (c) TFBG$_{2c}$.

In this case, the envelope of each TFBG$_2$ structure moves synchronously with the corresponding peaks. Therefore, the determination of the amplitude of certain peaks of the spectral transfer function of these structures also allows temperature independent strain measurement.

As indicated in Section 5.3, the structures TFBG$_2$ (Fibre Bragg grating in a tapered core fibre) are conceptually different from the TFBG$_1$ones, which rely on inducing a short fused taper in a fibre Bragg grating. However, the results presented show that the sensing properties of these two types of structures are similar. The reasons behind this fact will be the focus of further research.

5.5 Fibre Strain Sensitivity under the Mechanical Action of Short Tapers

Fibre Bragg gratings show a considerable set of positive features compared with other types of fibre sensors. However, one limitation is common to all of them, namely the cross sensitivity to both strain and temperature, being difficult to make independent measurements of these two parameters [104]. Several authors have proposed and demonstrated different sensing head geometries that change the strain sensitivity [101, 105]. In this section, it is demonstrated that using a single Bragg grating structure in series with a short fused taper, it is possible to control the strain coefficient sensitivity by changing the strain gauge.

Figure 5.21 shows a schematic diagram of the sensing element. The strain gauge of the sensing head is composed by a single FBG sensor in series with a short fused taper. The strain gauge of the sensing head have a total length of $L_{Total} = L_{FBG} + L_{Taper} + L_{Fibre}$.
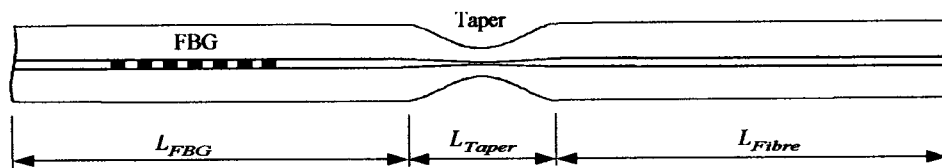
Figure 5.21 – Schematic diagram of the sensing head based on a single Bragg grating in series with a short fused taper.

If a strain ε_{FBG} is applied to the FBG at constant temperature, the central Bragg wavelength will be shifted by the Bragg wavelength variation $(\Delta\lambda_{FBG})$ according to:

$$\Delta\lambda_{FBG} = k_{\varepsilon(FBG)}\varepsilon_{FBG} \qquad (5.18)$$

where $k_{\varepsilon(FBG)}$ is a constant characteristic of the fibre material, which can be easily determined experimentally by analyzing the variation of the Bragg wavelength as a function of strain at constant temperature.

However, if the strain is applied to the entire sensor then an unequal load of stress will appear along each section of the sensor depending on the mechanical resistance. In

particular, the strain loads applied to the Bragg grating and the short fused taper are related according to:

$$\varepsilon_{FBG} EA_{FBG} = \varepsilon_{Taper} EA_{Taper}$$ (5.19)

where E is the Young Modulus of the sensor material, and A_{FBG} and A_{Taper} are the cross-sectional areas in the FBG and in the short fused taper region, respectively. Assuming that the mechanical properties of the material in both cases are the same, the strain applied to the two sensor sections and the claddings diameters will be related according to:

$$\frac{\varepsilon_{FBG}}{\varepsilon_{Taper}} = \frac{d_{Taper}^2}{d_{FBG}^2}$$ (5.20)

where d_{FBG} and d_{Taper} are the claddings diameters of the FBG and taper, respectively. The longitudinal strain of the FBG, the fused taper and piece of fibre are given by:

$$\varepsilon_{FBG} = \frac{\Delta L_{FBG}}{L_{FBG}}, \ \varepsilon_{Taper} = \frac{\Delta L_{Taper}}{L_{Taper}} \ \text{and} \ \varepsilon_{Fibre} = \frac{\Delta L_{Fibre}}{L_{Fibre}}$$ (5.21)

where, as shown in Figure 5.15, L_{FBG}, L_{Taper} and L_{Fibre} are the length of the sensor sections and ΔL_{FBG}, ΔL_{Taper} and ΔL_{Fibre} are the extension under the stress action of the FBG, the fused taper and the fibre, respectively. By definition, the total longitudinal strain of the sensing head is given by:

$$\varepsilon = \frac{\Delta L_{FBG} + \Delta L_{Taper} + \Delta L_{Fibre}}{L_{FBG} + L_{Taper} + L_{Fibre}}$$ (5.22)

Combining equations (5.18)-(5.20) and assuming that the diameter of the fibre is identical to that of the FBG (thus having the same local strain), it is possible to derive the relationship between the strain applied to the sensing structure and the strain experienced in the FBG as:

$$\varepsilon_{(FBG)} = \frac{L_{FBG} + L_{Taper} + L_{Fibre}}{L_{FBG} + L_{Taper}\dfrac{d_{FBG}^2}{d_{Taper}^2} + L_{Fibre}}\varepsilon \qquad (5.23)$$

Substituting equation (5.21) into equation (5.16), the Bragg wavelength shift can be rewritten as:

$$\Delta\lambda_{FBG} = k_{\varepsilon(FBG)}\frac{L_{FBG} + L_{Taper} + L_{Fibre}}{L_{FBG} + L_{Taper}\dfrac{d_{FBG}^2}{d_{Taper}^2} + L_{Fibre}}\varepsilon \qquad (5.24)$$

If the optical fibre with the FBG has N short fused tapers along the fibre, equation (5.22) can be generalized, yielding:

$$\Delta\lambda_{FBG} = k_{\varepsilon(FBG)}\frac{L_{FBG} + \sum_{i=1}^{N}L_{Taper_i} + L_{Fibre}}{L_{FBG} + \sum_{i=1}^{N}L_{Taper_i}\dfrac{d_{FBG}^2}{d_{Taper_i}^2} + L_{Fibre}}\varepsilon \qquad (5.25)$$

These equations permit to obtain the data shown in Figure 5.22, which presents the normalized (relative to the case of no taper) strain coefficient experienced by the FBG versus the total length of the sensing head for different diameter short fused tapers. It can be observed that a large reduction of the short fused taper diameter results in a significantly decrease in the strain sensitivity of the FBG sensor.
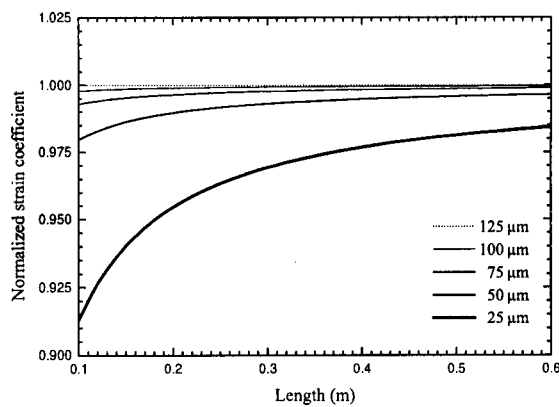
Figure 5.22 – Theoretical results for the normalized strain coefficient experienced by the FBG versus total length of the sensing head, for different diameter of the fused taper.

These results were checked experimentally. A sensing head with the geometry shown in Figure 5.21 was implemented. Three short tapers with different diameters (105 μm, 90 μm and 60 μm) were considered. For each of them, the total length of the sensing head was varied along the values 10 cm, 20 cm, 30 cm and 40 cm. The Bragg wavelength shifts versus the strain applied to the whole structure was monitored, providing the data given in Figure 5.23.

Experimentally, the sensing head (Figure 5.21) was fixed at two points and submitted to strain by using a translation stage. It were used three short tapers with different diameters (105 μm, 90 μm and 60 μm) and, for each sensing head, it was varied the total fixed length (10 cm, 20 cm, 30 cm and 40 cm). Figure 5.23 shows the response of the Bragg wavelength shift as a function of the applied strain.

(a)

(b)

(c)
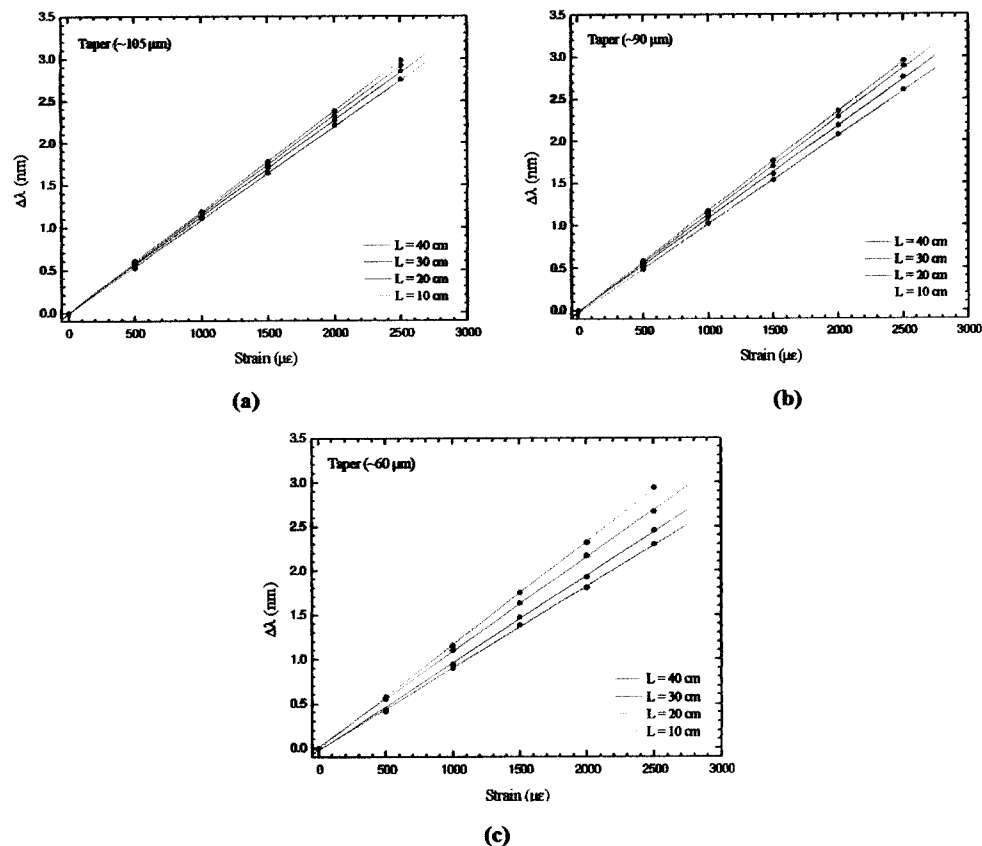
Figure 5.23 – Experimental results of wavelength shift versus applied strain
of the sensing head, for different lengths and different diameter fused tapers.

The strain sensitivity increases with the increase of both length and short taper diameter. For short values of length the strain induced by stress will be mainly applied

in the taper region once it has smaller diameter than the rest of the fibre. Due to that, the Bragg grating will have less sensitivity to strain for smaller values of L. Intuitively, decreasing the taper diameter will increase the stress applied in the taper region and hence the Bragg grating will decrease its sensitivity to strain. Table 5.6 shows the strain coefficients of the sensing head.

	Taper Diameter (μm)			
L (cm)	105	90	60	
10	1.11	1.05	0.92	
20	1.14	1.10	0.99	$\Delta\lambda/\Delta\varepsilon$
30	1.17	1.16	1.07	(pm/με)
40	1.19	1.18	1.17	

Table 5.6 – Strain coefficients versus total length of the sensing head for different diameter fused tapers.

Figure 5.24 shows the experimental results of the Bragg grating strain coefficients as a function of total length of the sensing head for different taper diameters. Comparing with the theoretical results presented in Figure 5.22, one can observe similar behaviors.
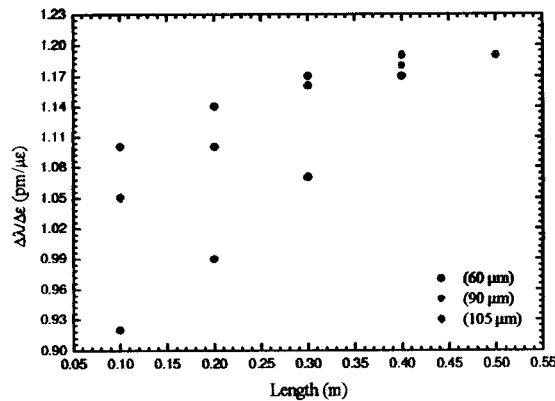
Figure 5.24 – Experimental results of Bragg grating strain coefficient versus total length of the sensing head for different diameter fused tapers.

These results reveal an interesting possibility, which is the tuning of the Bragg grating strain sensitivity by building up a short fibre taper and playing with two

parameters, namely the taper waist diameter and the distance between the fibre fix points (that determines the strain gauge). Therefore, it is feasible to have a fibre Bragg grating with adjustable reduced strain sensitivity, which is an important feature when the aim is to monitor parameters other than the strain. Clearly, this is not only interesting from the conceptual view point, but also important when dealing with specific applications.

6

Optical Filtering in LIDAR Systems

6.1   Introduction

The Earth's climate system is strongly influenced by the amount and distribution of atmospheric water vapour, liquid water and ice, as well as of the so called greenhouse gases (CO_2, CH_4, N_2O, and O_3). For example, water vapour plays a fundamental role in many atmospheric processes such as the atmospheric energy budget, global water cycle, atmospheric chemistry and transport of pollution. Also, it is already known that climate change is caused by complex interactions among many elements such as radiation, clouds, aerosols, precipitation, and atmospheric circulation.

The laser radar, or LIDAR, has played an important role in remote spatial sensing of atmospheric meteorological parameters. LIDAR systems offer a wide range of capabilities for the remote detection and monitoring from space of the atmosphere and its constituents, as well as for the measurement of certain land or sea surface parameters. Therefore, the development of advanced LIDAR systems for space applications is considered a key element for measurement of the atmospheric constituent's distribution around the world.

The European Spatial Agency (ESA) has developed strong technological basis on space LIDAR missions. The ADM-Aeolus mission is based on a Doppler wind LIDAR onboard, a satellite to be launched in 2007. An atmospheric backscatter LIDAR (ATLID) is part of the payload of the EarthCARE mission being considered and differential absorption LIDAR (DIAL) is part of the WALES mission. As part of its activities to prepare for a long-term program in Earth Observation, the Agency is now propoting the *Study on Observation Techniques and Sensors Concepts for the Observation of CO2 from Space*, which has the objective to provide a background for and pave the way towards the definition of a spaceborne LIDAR system(s) to monitor CO_2 and other greenhouse gases. Due to that, a recent project – the ESA-ONE Project, supported by ESA and in charge of INESC Porto – is under way to fulfil that task. The

goal of this R&D project is to demonstrate the feasibility of using ultra-narrow band micro-optic and fibre optic filters for atmospheric CO2 vapour LIDAR measurements. It is important to emphasize that in the context of this project the phase–shifted fibre Bragg grating structure was selected as the filtering device to discriminate the CO_2 emission line at the wavelength around 1600 nm.

In the next sections, besides a short overview of the LIDAR systems background, attention will be focused on the characteristics of some optical fibre filters, on the requirements of the optical filtering system and, finally, on the design and simulations of the proposed optical fibre filter.

6.2   LIDAR General Background

LIDAR (light detection and ranging) is a method that has been used since the 1960's to detect particles or gases in the atmosphere. It is an active remote sensing method, which means that light is sent out actively as a laser pulse instead of using light from the Sun. This method gives more freedom because the system is not dependent on sunlight. The idea of deploying a LIDAR system on an Earth orbiting satellite arises from the need to obtain a high resolution atmospheric profile structure with global coverage. Such a system would benefit directly areas of application ranging from the determination of global warming to the research of greenhouse effects. LIDAR systems have been extensively investigated, resulting in instrument concepts such as ATLID – an atmospheric backscatter LIDAR –, ALADIN – a Doppler wind LIDAR – and WALES – a water vapour differential LIDAR –.

LIDAR systems use a laser to send out short pulses of light into the atmosphere. Some of the radiation is reflected by the atmospheric molecules and aerosols and this back-reflected radiation is collected by a telescope. The radiation is analyzed, and the density of the atmosphere is then determined. Where the density is higher (i.e. closer to the Earth), a stronger backscattered signal is received.

Typical LIDAR systems are based on single wavelength laser emission that scatters on atmospheric molecules and aerosols. There are two main mechanisms of scattering: Rayleigh and Mie. Rayleigh scattering, also known as molecular scattering, is the scattering of light by particles that are small in comparison with the radiation wavelength. Mie scattering, also known as aerosol scattering, is the scattering by

particles that are larger than the radiation wavelength. Since LIDAR is a method that relies on a single wavelength, it renders impossible to trace different atmospheric species.

To measure the density of an atmospheric species such as CO_2, a more advanced LIDAR technique is used. This technique is a special development of LIDAR called absorption LIDAR (DIAL). It is based on the fact that different atoms and molecules absorb different laser wavelengths. The DIAL technique is a selective and sensitive method that exploits specific absorption lines present in the spectral signature of any atoms and molecules. This technique compares the attenuation, through the atmosphere, of two laser pulses with slightly different wavelengths. One pulse is emitted with a wavelength set to match a particular absorption line of the particle of interest, while the second one is emitted on a spectral window that experiences very low absorption. By looking at the ratio of these return signals as a function of range, the density profile of the species can be derived.

6.3   Optical Filtering

A key element of any LIDAR instrument is the optical filtering system that is used to spectrally filter the incoming light on the receiver telescope. For LIDAR applications, including wind and aerosol measurements, spectral filtering is used to separate the narrow aerosol Mie backscattered signal from the molecular Rayleigh backscattered signal. For LIDAR applications using the DIAL method, such the intended in this project to measure CO_2 concentrations, spectral filtering is necessary in order to separate the return signals from the multiple laser pulses. In addition, narrowband filtering is essential in reducing the effect of background radiation on the observed signal-to-noise ratio that might otherwise overwhelm the backscattered LIDAR signal. Hence, the optical bandwidth of the receiver plays here a crucial role in the reduction of the background noise. By reducing the optical bandwidth of the receiver, the noise signal can be substantially reduced, thus improving the measurement signal-to-noise ratio, especially during daylight. This is important because building a higher energy laser or a larger telescope to improve the signal-to-noise ratio in space is very costly.

To ensure high-quality system performance, the optical filters must combine extremely narrow pass-band response with wide spectral background rejection. Filters

that are used today have typical full-width at half maximum (FWHM) of 300 pm, when using multilayer thin-films, but this could be reduced to some tens of picometers by using an optical fibre Bragg grating filter, as reported in [106] and planed also to be done in ESA-ONE project.

There are many approaches to achieve optical filtering with potentially high spectral selectivity. All of them rely on the same concept, i.e., the generation of a large number of coherent waves with similar amplitudes that are allowed to interfere. Due to the high number of waves, the condition for constructive interference has a tight tolerance in wavelength, which translates into a narrow spectral window where the degree of constructive interference is significant.

There are standard geometries to achieve multiple interferences. The oldest one, and probably the most important, is the Fabry-Perot interferometer, which has multiple realizations, from the classical scheme implemented with bulk optics, up to recent thin film structures. Another geometry that has brought considerable flexibility is the fibre ring resonator, which will also be considered in this section. The third one that will be addressed in this section is the fibre Bragg grating structure, a technological development of the nineties which permitted high flexibility and remarkable filtering performance. It is this structure that will be analyzed with more detail, in view of its selection for the project narrow filter implementation.

6.3.1   Filtering Based on Fabry-Perot Interferometers

Space DIAL LIDAR systems require very narrow, rugged, high transmission and tunable receiver optical filters in order to separate the return signals from the multiple laser pulses as well to reduce the background radiation. Among all tunable filters, Fabry-Perot interferometer (FPI) is one of the most common used structures. Based on multiple beams interference effects, the Fabry-Perot cavity consists of two parallel partially reflective lowloss mirrors separated by a uniform gap (see section 4.2). The key performance parameters of a high-resolution filter based on the Fabry-Perot interferometer are the transmission and narrow bandwidth together with large free spectral range (spectral separation of transmission fringes). The free spectral range of a Fabry-Perot cavity is driven from equation (4.16) and is given by

$$\Delta f = \frac{c}{2nd} \qquad (6.1)$$

where c is the speed of light, n is the refractive index of the cavity medium and d is the cavity length. If the transmission linewidth is δf, then the bandwidth and free spectral range of a Fabry-Perot cavity are related by its *finesse*

$$F = \frac{\Delta f}{\delta f} \qquad (6.2)$$

which is a measure of the degree of interference between light rays reflected between the two mirrors. A small bandwidth and large free spectral range imply a large *finesse*. The overall *finesse* is dependent on several contributions as already been demonstrated in section 4.2 (equations 4.8 to 4.14). Fabry-Perot filters for DIAL LIDAR systems have been developed [107] with a free spectral range of 4 nm and a bandwidth of 25 pm for a *finesse* of 160. It also combines a tuneable range of 9 nm with a transmission greater than 50%. Therefore, the importance of these parameters optimization is driven by the need of high performance tuneable, narrowband filters that match the key requirements for filtering applications in DIAL LIDAR systems.

6.3.2   Filtering Based on Fibre Ring Resonators

Optical ring resonators have numerous applications in industrial sensing [108, 109], signal processing [110–113], in communication [114], in laser systems [115–119], in interferometry [120, 121], etc. For many years this device has been routinely used as a circuit component in microwave engineering. The main difference between the optical and microwave versions is the size relative to the operating wavelength, in essence the mode number N. In most optical rings, the mode number is very large. Only recently, with the help of extreme miniaturization has this mode number been reduced to be in the order of 100 in photonics. In this area, the optical ring resonator is most often used as a building bloc in a filter [122–124], a delay line [125–127], a channel dropping/combining [128–132] or a dispersion compensation system consisting of several resonators and other optical components such as waveguides, couplers,

etc.[133–136]. However, they also find application in sensor multiplexing [109, 137], electrooptic modulators [138] and in nonlinear signal processing [139–144].

These structures can be fabricated using bulk optical elements (mirrors and beam splitters), fibre optic components or integrated optics technology. This section will be focused only on the ring resonator implemented with optical fibre, being addressed some of its general properties and their importance in filtering applications.

6.3.2.1   General Properties of Optical Fibre Ring Resonators

An optical ring resonator consists of a reentrant waveguide whose perimeter can be in the order of meters for a bulk optical or fibre optic device, or in the order of millimeters for an integrated device. The ring supports circulating waves that resonate at a guide wavelength λ_{wg} for which $N\lambda_{wg} = L$, where N, an integer, is the mode number and L is the circumference of the resonator. This relationship indicates that the resonances are spaced periodically on the frequency scale, much like those of a comb filter. The separation between consecutive resonances, the so-called free spectral range (FSR), is the inverse of the time delay of the signal in the ring and is, therefore, inversely proportional to the length of the perimeter.

To be of use the resonator must be connected to the external circuitry. This is accomplished through one or two couplers, creating in the process a two-port or a four-port device. Regarding to a single-mode optical fibre ring connected to one coupler, it can be formed a simple variant of the fibre Fabry-Perot interferometer (FFPI), as it is shown schematically in Figure 6.1.
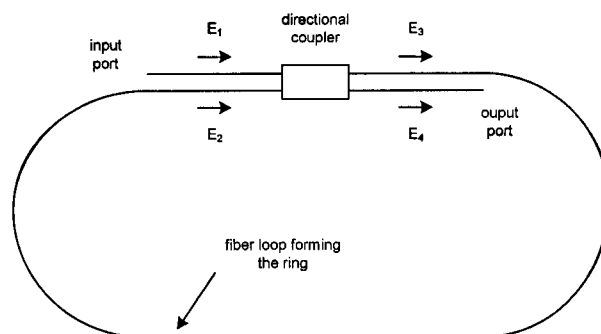
Figure 6.1 – Schematic of an all-single-mode fibre resonator. [145]

With a simple analysis of this figure it is possible to obtain the resonator *finesse* in terms of fibre and directional coupler parameters [145]. Input light of amplitude E_1 entering the coupler will be amplitude divided into two components: E_3 enters the ring and E_4 is directly coupled to the output port (4). Light recirculating in the ring will interfere with these signals.

From conservation of energy

$$|E_3|^2 + |E_4|^2 = (1-\gamma)(|E_1|^2 + |E_2|^2),$$ (6.1)

where γ is the coupler intensity loss and

$$E_3 = (1-\gamma)^{1/2} \left[(1-\gamma)^{1/2} E_1 + i\sqrt{k} E_2 \right]$$ (6.2)

and

$$E_4 = (1-\gamma)^{1/2} \left[i\sqrt{k} E_1 + (1-\gamma)^{1/2} E_2 \right],$$ (6.3)

where κ is the intensity coupling coefficient. Here the coupler is assumed to act as a conventional beam splitter in that the light coupled from one fibre to the other is phase shifted by $\pi/2$. Therefore,

$$E_2 = E_3 e^{-\alpha L} e^{-i\beta L}$$ (6.4)

where L is the length of the ring, α is the amplitude attenuation coefficient of the fibre and $\beta = \dfrac{n\omega}{c}$, being n the refractive index.

Clearly there will be a resonance condition for this interferometer, and this will occur when the increase in phase of the beam in the ring equals $(2\pi m - \pi/2)$ i.e. $\beta L = 2\pi m - \pi/2$ $(m = 1, 2, ...)$; the fraction of E_2 which now couples back into the ring will be in phase with the fraction of E_1 which couples into the ring. When this condition is obeyed no light will appear at the output port (rather like the back reflected output from the Fabry-Perot interferometer at resonance) and one can show that for $|E_4 / E_1|^2 = 0$

$$\kappa = \left(1 - \gamma\right)e^{-2\alpha L}.$$

(6.5)

The transfer function of the output can be written as

$$\left|\frac{E_4}{E_1}\right|^2 = \frac{(1-\gamma)\kappa^2}{(1-\gamma)^2 - 4\kappa\sin^2\left(\frac{\beta L}{2} - \frac{\pi}{4}\right)}$$

(6.6)

and is plotted in Figure 6.2 as a function of βL, and is seen to be similar to the variation of the back reflected light as a function of δ (optical phase difference) in the conventional FPI.
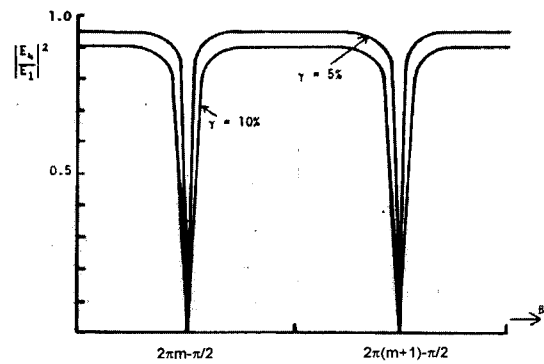
Figure 6.2 – Transfer function of ring resonator as a function of βL. [145]

The ring resonator clearly has potential for optical filtering applications, being possible to attain remarkably high spectral selectivity.

6.3.2.2   Applications of Optical Fibre Ring Resonators

As seen in previous section, single-mode optical fibre can be used to make a high-finesse optical resonator by forming a short piece of fibre into a closed ring to constitute a low-loss cavity. In the earlier days, it was possible to achieve a *finesse* of 80 by using a directional coupler and a strand of single-mode optical fibre bonded into two slotted quartz blocks at a distance L apart [145]. Using an all-fibre ring resonator with high-finesse it was also possible to obtain a multi-pass fibre optic interferometric filter with high sensitivity to periodic phase shifts induced in the fibre ring [146]. The low round trip loss of fewer than 5% gave a finesse of 70 and an input fibre to output fibre

transmission of 97%. An all-fibre terminal-reflected ring resonator was also proposed as a highly sensitive interferometric sensor [147]. The concept was very similar to the fibre Fabry-Perot interferometer in multiple beam interference, but with the advantage that only one strand of fibre was needed to construct the fibre sensing system. The fibre ring resonator includes an evanescent-field directional coupler fabricated with highly birefringent single-mode fibre, since the output fluctuations caused by the polarization-dependent optical interference can be suppressed by the excellent ability of the fibre to maintain polarization. Emphasis was given to the fact that this all-fibre sensing system can be doubly sensitized only over the fibre ring by reflecting the throughput light at the terminal. Also in sensing applications, an optical fibre phase modulator with enhanced modulation efficiency was fabricated [148]. A length of single-mode optical fibre is attached to a piezoelectric plate, formed into a free loop, and reattached to the plate. Applying an alternating voltage to the piezoelectric plate causes it to expand and contract, producing a modulating strain in the optical fibre. The induced longitudinal strain travels in opposite directions around the fibre loop, creating a standing wave. This configuration reduces the dependence on the PZT and, in addition, the modulator offers an enhancement of the modulation depth and flexibility in frequency of operation. Fibre ring resonators have also applications as optical filters in spectrum analyzers with high resolution [149]. The fabrication of a high-finesse structure allows its utilization in the measurement of discrete-frequency components and laser linewidths with an optical resolution of 20 kHz. In many applications it is needed a structure that is insensitive to polarization. A fibre optic ring resonator configuration based on a reflective mode of operation was reported were a Faraday rotator mirror for birefringence compensation was used. An output resonant-dip transfer function that is independent of the input polarization to the system is obtained, which is shown to produce a stable scale factor of the system [150].

Many different configurations of single-mode optical fibre ring or loop resonators connected to one, two, or three 2x2 fibre couplers have been proposed and studied. It has also been reported the demonstration of a single-mode optical fibre double- loop resonator with equal recirculating loop lengths and two identical or nonidentical 2x2 fibre couplers [151].

The ring resonator has four essential physical characteristics that can be exploited in photonic applications. Its notch filter amplitude characteristics near critical coupling, its flat amplitude characteristics far from critical coupling, its group delay characteristics

that can cause a long entrapment of the signal, and finally the magnification of the signal amplitude circulating in the ring which is associated with energy storage. These characteristics are controlled by the optical length of the ring, the coupling strength and the loss (or gain) incurred per turn [152]. Standard methods of optical filter synthesis can be used to exploit these characteristics for the design of composite frequency filters and dispersion compensators that are made up of series or parallel coupled ring resonators [153].

The relative ease with which gain can be introduced into the ring relieves limitations imposed by waveguide loss; it is instrumental in achieving sharp selectivity, high Q, and large finesse. Applications such as filtering, modulation, sensing and measurement are possible depending on the practical control of parameters such as the perimeter of the ring (L), the intensity coupling coefficient (κ) and the amplitude attenuation coefficient (α).

Current trends in fabrication technology evolving toward miniaturization, the increased use of polymers and utilization of whispering gallery mode resonators in their various forms will ensure that ring resonators remain an important component of modern photonics.

6.3.3   Filtering Based on Fibre Bragg Gratings

The key requirements for ultra-narrow filters for LIDAR applications are a bandwidth lower than 40 pm, a tunable range over 6 nm and a transmission higher than 50%. Such tight requirements can be achieved in optical fibre devices with ultraviolet photosensitivity fabrication techniques either through long-uniform FBGs, π-shift Bragg gratings or Bragg grating Fabry-Perot filters. However, the definition of these periodic microstructures demands a very fine control of the writing conditions.

The characteristics of the spectral response of fibre Bragg gratings – i.e., reflectivity and spectral width – are limited by the maximum refractive index change Δn that is possible to photoinduce in the fibre core and by the maximum extension of the Bragg grating, L. The range of design parameters available to the fibre Bragg grating technology is even though much wider than the ones accessible to other techniques of manufacturing diffractive components compatible with optical fibres. This superiority arises mainly from the possibility of manufacturing very long fibre Bragg gratings with

great flexibility on the local definition of the period and amplitude of the refractive index modulation.

In the design of a uniform fibre Bragg grating, the integrated coupling constant (κL) proportional to the refractive index change and to the length of the FBG is of great importance, since it is directly correlated with the maximum attainable reflectivity and the minimum spectral width. The same peak reflectivity value can be obtained by conjugating high refractive index changes with small grating length or vice versa. This as already been demonstrated with the simulation results shown in section 2.5. It is possible to attain the same maximum reflectivity through longer Bragg gratings with low refractive index changes, being in this case the spectral response narrower. Such grating is, in principle, easier to manufacture since it requires lower refractive index changes; however, the uniform refractive index change must be kept uniform over a long fibre optic segment, which also places very tight constrains on the manufacturing process. In other hand, fibre Bragg gratings operate intrinsically in reflection thus requiring a further component in order to ensure proper transmission filtering. Such a component can be a fibre coupled three-port circulator that allows not only to obtain proper spectral filtering, but also to effectively eliminate background radiation by using anti-reflection coating at the fibre end (see section 2.3.1). Another approach is to use a FBG based Fabry-Perot or a π-shift Bragg grating; these devices are obtained by introducing a phase shift on the refractive index spatial modulation profile [49]. Although in this case the narrow transmission band is readily available to perform the optical filtering operation, it is further necessary to combine this device with a broadband thin-film rejection filter to eliminate the background radiation.

6.4   Project Optical Filtering Requirements

Previous research performed at NASA demonstrated the feasibility of using narrowband fibre optic Bragg grating filters for atmospheric water vapour DIAL measurements [106, 154, 155]. In Europe, the mission ESA WALES (*Water Vapour Lidar Experiment in Space*), oriented to the study of water vapour distribution in the lower atmosphere, has framed most of the activity developed over the past years on space DIAL LIDAR systems. Critical in these systems is the optical filtering sub-system, to separate the return signals from the background radiation that might, otherwise, overwhelm the

back-scattered LIDAR signal. The optical filtering technology adopted in that mission was based on a capacitance stabilized Fabry-Perot bulk interferometer, for the high resolution tunable filter, combined with a high transmission broadband interference filter for out-of-band background rejection [107]. The main specifications demanded for these filters are indicated in Figure 6.3.

The main objective of the ESA-ONE project is the design, fabrication and characterization of a high resolution tunable optical fibre filter to implement a DIAL LIDAR system for CO_2 detection. To improve the signal-to-noise ratio, the background radiation must be strongly rejected outside a spectral window centered on the selected CO_2 emission line ~1600 nm. Therefore, the optical filtering sub-system of the DIAL LIDAR system is the combination of two filters, one for background rejection, which can be a thin film interference filter, and a second to implement the spectral narrowband and tunable functionalities required by the DIAL technique. This section addresses the several issues that must be considered to have a high performance narrowband tunable filter based on fibre optic Bragg grating technology. A phase-shifted structure will be considered. For this type of filter the relevant parameters are defined in Figure 6.4.

An essential step is the specification of the target values for these parameters. The document *Requirements Definition for Future DIAL Instruments* [156] is not definitive about the specifications required for the optical filtering sub-system, independently of the particular technology employed for its implementation. Actually, in this document it is emphasized the advantages of using heterodyne detection, where the interference signal of the receiver echo with a local oscillator is detected. The down-converted RF frequency carrier represents the optical signal in amplitude and phase, from where can be recovered the information about the gas column. Because this signal has a frequency well above the frequency corresponding to the slow variations of the radiation background, it is stated *"...background light is of little concern to heterodyne measurements owing to its narrow bandwidth.".* This may be true but bounded to the need to avoid the saturation of the photodetection block due to the essentially DC radiation background. This means that the broadband filter for background rejection is still an obvious requirement.

BroadBand Filter

T_{BB}

1
A_{BB}

$\lambda_0 = 935.5$nm
$\delta\lambda_{BB} < 2$nm
$A_{BB} > 0.8$
$R_{BB} > 50$dB

R_{BB}

$\delta\lambda_{BB}$

λ_0　λ

(a)

High Resolution Filter

$\Delta\lambda_{tuning}$

T_{FP}

1
A_{FP}

$\Delta\lambda_{FSR}$

$\lambda_0 = 935.5$nm
$\delta\lambda_{FP} < 40$pm
$A_{FP} > 0.5$
$\Delta\lambda_{FSR} = 6$nm
$\Delta\lambda_{tuning} = 6$nm

$\delta\lambda_{FSR}$

λ_0　λ

(b)
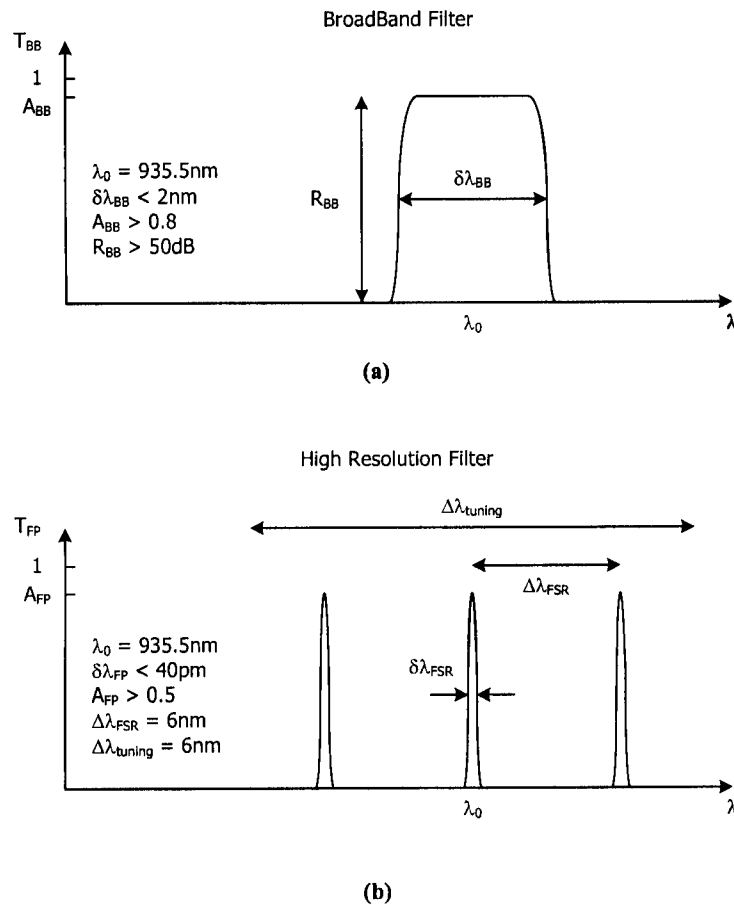
Figure 6.3 – Filter requirements for the ESA WALES mission: (a) background rejection filter (interference filter); (b) high resolution filter (bulk Fabry-Perot).[107]

On the other hand, concerning the narrowband filtering functionality it is written in the cited document:

Narrowband filters for suppression of spectrally broad lidar echos are required. Filter technologies based on interference filters, Fabry-Perot, or birefringent filters show a degree of maturity that suggests their successful application to compensate for detrimental spectral properties of the laser transmitter. Filters combinations of the above mentioned filter concepts have shown to achieve resolving powers of the order of > 100.000 and to simultaneously provide decent acceptance angles. These filters gain their heritage from solar astronomy where similar requirements are demanded. Nevertheless, the prospect to relax the stringent requirements put on the spectral purity of the lidar transmitter depends on both, the passband of the filter(s) and the detailed spectral behaviour of the laser. Therefore, this issue needs further analysis based on

appropriate models of the spectral shape of the emitted radiation for the different transmitter concepts.
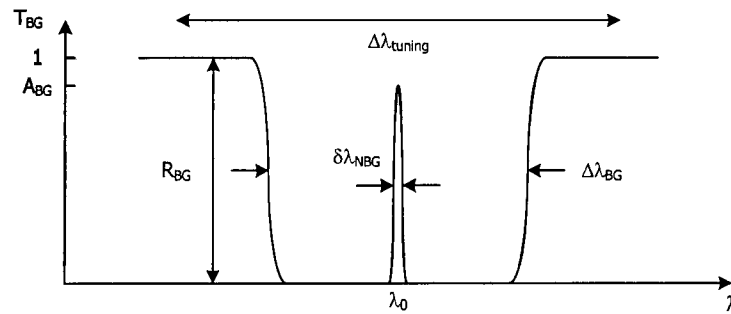
Figure 6.4 – Spectral structure and relevant parameters of a phase-shifted fibre Bragg grating optical filter.[102]

In this context it is not possible in the present stage to fix definitely the optical filter parameters required for future DIAL instruments. Due to that, the option was to follow the specifications expressed for the WALES mission – i.e., admitting the need of a broadband filter with the same specifications as those given in Figure 6.3(a); for the high resolution filter it was followed closely the specifications for the Fabry-Perot filter given in Figure 6.3(b) –. Therefore, the fibre Bragg grating based optical filter must fulfill the characteristics presented in the following table:

λ_0	$\sim 1600 nm$
$\delta\lambda_{NBG}$	$< 40 pm$
$\Delta\lambda_{BG}$	$> 2nm$
A_{BG}	> 0.8
R	$20 dB$

Table 6.1 – Specifications required for the phase-shifted fibre Bragg grating.

The parameters $\Delta\lambda_{FSR}$ for the Fabry-Perot filter (free spectral range) and $\Delta\lambda_{BG}$ for the fibre Bragg grating are not directly comparable. The reason to choose $\Delta\lambda_{BG} > 2nm$ has to be with the defined passband for the broadband filter.

6.5 Filter Design and Simulations

The fibre Bragg grating filter will be based on a phase-shifted structure. Figure 6.5, shows the transmission spectral function of a π-shifted grating with constant period of the refractive index modulation, for three different values of the phase shift. These results permit to draw the following conclusion: the width of the rejection band, which decreases for larger values of $L_1 + L_2$, is far below the required minimum value of 2 nm for the type of filter under concern in the ESA-ONE project.
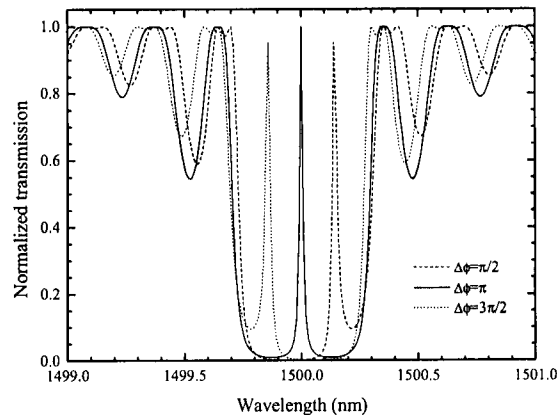
Figure 6.5 – Spectral transmission of a phase-shifted Bragg grating for three values of $\Delta\phi$, for $\Delta n = 5\times10^{-4}$ and $L_1 = L_2 = 2.5$mm.

Therefore, in order to have a larger width for the rejection band chirped phase-shifted Bragg gratings shall be considered, reserving the positive effects of a larger depth refractive index modulation, which is easily accessible during the fabrication through control of the UV exposure time, as an extra degree of freedom for final tuning of the grating spectral response.

To evaluate the effect of the several grating parameters on the characteristics of its spectral transfer function, the commercial software *Fibre Optic Grating Simulator* from *Apollo Photonics* was used. Figure 6.6 gives simulation results for the reflection transfer function of π-shifted Bragg gratings with length $L = 20$ mm and $L = 30$ mm, considering different values of the chirp rate, φ (the transmission spectral function is the complimentary one; the central wavelength of $\lambda_0 = 1546 nm$ was chosen only by convenience).

L = 20 mm	L = 30 mm
$\varphi = 0.1nm/cm$	$\varphi = 0.1nm/cm$
$\varphi = 0.2nm/cm$	$\varphi = 0.2nm/cm$
$\varphi = 0.3nm/cm$	$\varphi = 0.3nm/cm$
$\varphi = 0.4nm/cm$	$\varphi = 0.4nm/cm$
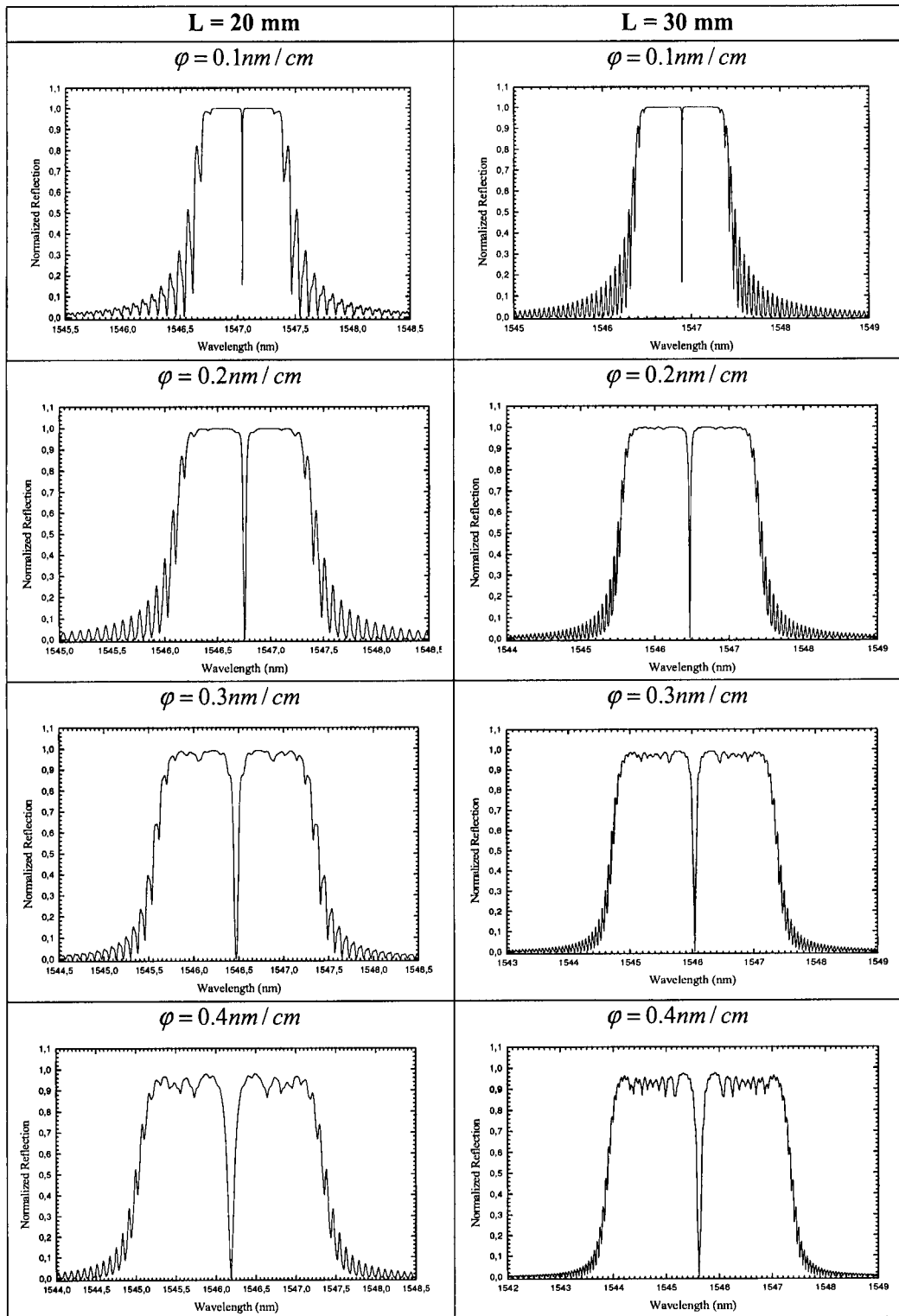
Figure 6.6 – Reflection transfer function of p-shifted Bragg gratings with lengths of 20 mm and 30 mm, for different chirp rates ($\Delta n = 0.0004$).

These results indicate that when the chirp rate increases, increases also the width of the reflection band and of the notch at the middle of the reflection band. On the other hand, for a fixed chirp rate when the length of the grating increases, increases also the width of the reflection band and decreases the width of the central notch. These results are summarized in Table 6.2.

chirp rate (nm/cm)	L = 20mm		L = 30mm	
	reflection band (FWHM) (nm)	notch (FWHM) (pm)	reflection band (FWHM) (nm)	notch (FWHM) (pm)
0.1	0.84	3	1.0	1.94
0.2	1.28	28.8	1.9	23.4
0.3	1.8	56.7	2.7	52.4
0.4	2.3	124	3.5	104.6

Table 6.2 – Width of the reflection band and of the central notch for the cases shown in Figure 6.6 ($\Delta n = 0.0004$).

Comparing the contents of Table 6.1 and Table 6.2, it can be observed that the situation of a π-shifted Bragg grating with L = 30 mm and $\varphi = 0.25 nm/cm$ fulfils the established requirements – i.e., width of the reflection band >2 nm; width of the central notch <40 pm.

When the amplitude of the modulation index increases, it is expectable smaller amplitudes for the oscillations of the transfer function, from one side, and also a larger width for the reflection band and a narrower width for the central notch. The simulation confirms these trends, as can be checked from Figure 6.7 and Table 6.3. It must be mention that the software was not able to resolve the central notch, being therefore not possible to estimate its width. For illustration purpose only the central transmission line was artificially added.

The most relevant conclusion associated with the case $\Delta n = 0.001$ comparatively to the case $\Delta n = 0.0004$, is that now it is enough to have a grating length of L = 20 mm combined with a chirp rate of $\varphi = 0.4 nm/cm$ to fulfill the filter requirements. This is relevant if it is taken into account that the price of chirp phase masks for chirp grating fabrication increases substantially with its length.

L = 20 mm	L = 30 mm
$\varphi = 0.1 nm / cm$	$\varphi = 0.1 nm / cm$
$\varphi = 0.4 nm / cm$	$\varphi = 0.4 nm / cm$
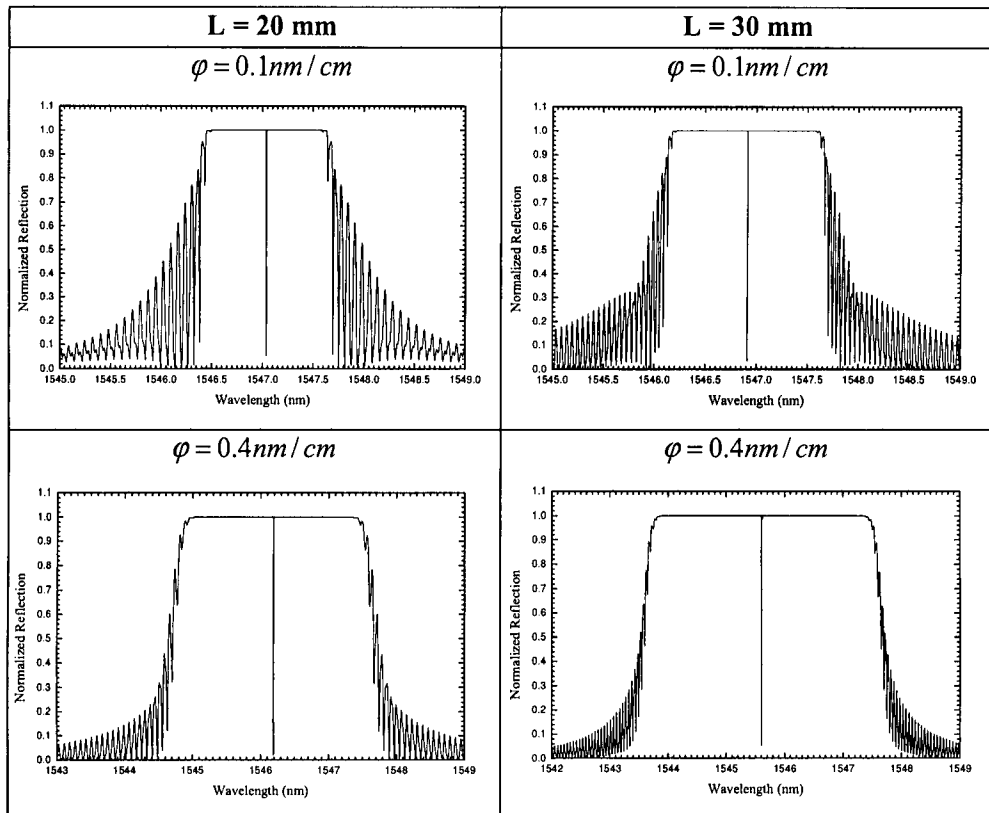
Figure 6.7 – Reflection transfer function of π-shifted Bragg gratings with

lengths of 20 mm and 30 mm, for two different chirp rates ($\Delta n = 0.001$).

chirp rate (nm/cm)	L = 20mm		L = 30mm	
	Reflection Band (FWHM) (nm)	Notch (FWHM) (pm)	Reflection Band (FWHM) (nm)	Notch (FWHM) (pm)
0.1	1.3 nm	----	1.6 nm	----
0.4	2.9 nm	----	4.1 nm	----

Table 6.3 – Width of the reflection band for the cases shown in **Figure 6.7**

($\Delta n = 0.001$).

6.6   Future Developments

Manufacturing a uniform phase shift fibre Bragg grating to match the specifications of the project is a very demanding task, since for achieving a narrowband transmission < 40 pm over a >2 nm bandwidth imposes a very small extension of the modulation of the refractive index and a very high refractive index modulation depth.

The proposed approach to overcome this limitation is based on chirped phase shift fibre Bragg gratings. This is an innovative device that was simulated here to evaluate its application towards the fulfillment of the technical specifications of the project. It was demonstrated that the situation of a π-shifted Bragg grating with $L = 20$ mm and $\varphi = 0.4 nm / cm$ fulfils the established requirements.

It must be emphasized that these are preliminary simulations that soon will be correlated with experimental data that will be obtained in the context of the project, which outlined part of this MSc dissertation.

7

Conclusions

Fibre Bragg gratings are the common ground line behind the topics addressed in this MSc dissertation. Indeed, the developed work was based on the utilisation of these fibre structures for sensing and filtering applications.

In chapter 2 it was presented the technology of Bragg gratings in optical fibres. The general properties of Bragg gratings as well as the coupled mode theory were described. Simulation results support the feasibility of using fibre Bragg gratings to develop narrow bandpass filters with characteristics adequate for sensing and in-fibre filtering applications. To evaluate the effect of the several grating parameters on the characteristics of its spectral transfer function, the commercial software *Fibre Optical Grating Simulator* from *Apollo Photonics* was used. From simulation results it was shown that is possible to attain maximum reflectivity with narrow spectral response through long Bragg gratings (> 30 mm length) with low refractive index changes. Such gratings are, in principle, easier to manufacture since it requires lower refractive index changes; however, the uniform refractive index change must be kept uniform over a long fibre optic segment, which also places very tight constrains on the manufacturing process. Some sensing properties are also reviewed, where typical sensitivity values of $(1.06 \pm 0.01) pm / \mu\varepsilon$ and $(9.71 \pm 0.09) pm /^{o} C$ for strain and temperature, respectively, were obtained.

Chapter 3 presented a different approach for sensing and filtering applications: *the phase-shifted Bragg grating*. These devices are obtained by introducing a phase shift on the refractive index spatial modulation profile. It was shown that the sensing characteristics of these structures, namely to strain and temperature, are similar to those associated with a uniform fibre Bragg grating. The simulation results showed that is possible to gather the conditions to make from fibre Bragg gratings good optical filters. For high values of the modulation index (>10^{-3}), the bandwidth of the transmission peak become very narrow and the width of the rejection band increases. Also, the

introduction of chirp in phase-shifted fibre Bragg gratings will increase the rejection band, which combined with a sharp transmission peak can perform interesting spectroscopy functions.

In Chapter 4 it was presented the technology of grating based fibre Fabry-Perot interferometers for dynamic strain sensing. Theoretical aspects of Fabry-Perot interferometers (FPI) and the properties of different types of FPI based on fibre Bragg gratings were described. Two sensing configurations were proposed as applications as strain sensing structures. The first configuration used a tunable laser to address the phase of the FFP interferometer. When submitted to strain, the FFP showed a linear behavior where a strain phase sensitivity of $7.46 \pm 0.07°/\mu\varepsilon$ was obtained. The second one used a π-shifted grating to address the phase of the interferometer. This structure working in transmission has the same functionality as the tunable laser. It acts as an narrow tunable filter when submitted to strain. The phase dependence with strain was also linear, with a sensitivity of $(2.19 \pm 0.02)°/\mu\varepsilon$. The difference in sensitivity values has to be with the fact that the cavity length of the second configuration is smaller by a factor of ≈ 3. Finally, it was proposed an interrogation technique for an FFP interferometer that is based on the dynamic modulation of the spectrum of light arriving from the FFP cavity by the spectral transfer function of a π-shifted FBG. The implementation of the demodulation scheme requires that a dynamic carrier signal be produced through the modulation of the phase-shifted grating. This was achieved by modulating the π-shifted structure with a sinusoidal wave by means of a piezoelectric disk. The modulation scheme was implemented by means of a LabView^{TM} based program developed for this purpose. Preliminary results have been shown of the experimental modulated interferometric signal as well as of the phase-modulated electric carrier.

In Chapter 5 it was presented fibre optic structures based on short fibre tapers. These structures have shown to be useful optical fibre structures for a variety of grating-based sensing applications. It was demonstrated that the combination of short fibre tapers with Bragg gratings enables new sensing structures with properties dependent on the fabrication process. a short fused taper in a fibre Bragg grating and a Bragg grating in a tapered core fibre (TFBG$_2$).

Performing a short fused taper in the middle of a fibre Bragg grating originates a structure named $TFBG_1$; fabrication of a Bragg grating in a tapered core fibre gives rise to another structure ($TFBG_2$). $TFBG_1$ is a Fabry-Perot interferometer because the arc discharge erases the grating in the taper section; in practice, the structure will be formed by two shorter Bragg gratings separated by a tapered cavity. In $TFBG_2$ the grating is written in the taper section where the effective index is different and thus causing a phase change. Due to that, $TFBG_2$ can be seen as a phase-shifted tapered structure. The sensing characteristics of these two types of structures are similar; the determination of certain peaks of the spectral transfer function of these structures allows temperature independent strain measurement, a feature which is not exhibited by many sensing heads oriented to measure strain. Finally, theoretical aspects and experimental results of fibre strain sensitivity under the mechanical action of short tapers were presented. It was demonstrated that using a single Bragg grating structure in series with a short fused taper, it is possible to control the strain coefficient sensitivity by changing the strain gauge. It was demonstrated that the strain sensitivity increases with the increase of both length and short taper diameter. The results showed that is feasible to have a fibre Bragg grating with adjustable reduced strain sensitivity, which is an important feature when the aim is to monitor parameters other than the strain.

Chapter 6 dealt with the general aspects of optical filtering in LIDAR systems. In particular, it focused the attention to the requirements of an optical filtering subsystem to be implemented in a LIDAR system. For the proposed optical fibre filter a phase-shifted structure was considered. The goal was to combine a large rejection band with an ultra-narrow transmission peak. Simulation results showed that it is sufficient to have a grating length of L = 20 mm combined with a chirp rate of $\varphi = 0.4 nm / cm$ to fulfill the filter requirements.

Fibre Bragg grating-based sensing has proven to be a very promising research area and new developments can be expected to continue in the near future. In particular, π-phase shifted devices and fibre Fabry-Perot interferometers based on Bragg gratings offer the potential to provide novel and interesting sensing, filtering and signal processing techniques.

One obvious topic for (near) future work is to finish the work around the dynamic interrogation of fibre Bragg grating based Fabry-Pérot interferometers using a wavelength modulated π-shifted fibre Bragg grating. The description and preliminary results given in Chapter 4 are a clear indication of the potential of this technique. In particular, it is envisaged the development of a LabView^{TM} based program that simulates a lock-in amplifier to read the carrier phase. With this it is possible to obtain a full digital signal processing approach that will minimize problems with noise and fluctuations, and in other hand will ensure accuracy in measurements.

Another obvious topic for future work is in the field of fibre optical filtering for LIDAR systems. Within the context of the European Space Agency project, the next step is to fabricate and characterize a Bragg grating based optical fibre phase-shifted structure that combines a large rejection band with an ultra-narrow transmission peak, gathering therefore the filter requirements that were obtained by simulation results. This development will permit to validate the adequacy of this fibre filtering approach, and to assess its advantages and drawbacks relatively to the standard solution which relies on bulk Fabry-Pérots.

This work also revealed the interesting sensing structures that result from the combination of fibre Bragg gratings with short fused tapers. One interesting development would be to considerer the utilization of these structures for refractive index measurement through evanescent field coupling. Eventually, this interaction could be enhanced combining these structures with nearby dielectric microspheres, which are well known devices for highly selective environment detection through gallery modes interaction.

In line with developments performed along this MSc dissertation, other topics for R&D in optical sensing with fibre gratings could be outlined. However, as happens quite often, as soon as the research process is under way it is highly probable that unexpected and fascinating possibilities will appear around the journey. Therefore, this is the best guarantee and motivation for future work in the subject.

References

[1] J. M. López-Higuera (Editor), *Handbook of Optical Fibre Sensing Technology.* New York: John Wiley, 2002.

[2] B. Culshaw, "Optical Fiber Sensor Technologies: Opportunities and-Perhaps-Pitfalls", *J. Lightwave Technol.*, vol. 22, no. 1, pp. 39–50, 2004.

[3] Dakin and B. Culshaw (Editors), *Optical Fibre Sensors: Applications, Analysis and Future Trends.* Boston: Artech House, 1997.

[4] A. Othonos, K. Kalli, *Fiber Bragg Gratings.* Boston: Artech House, 1999.

[5] A. D. Kersey, M. A. Davis, H. J. Patrick, M. LeBlanc, K. P. Koo, C. G. Askins, M. A. Putnam and E. J. Frieble, "Fibre Grating Sensors", *J. Lightwave Technol.*, vol. 15, no. 8, pp. 1442-1463, 1997.

[6] G. P. Agrawal, *Fiber-Optic Communication Systems.* New York: John Wiley, 2002.

[7] C. L. Hagen, J. R. Schmidt, and S. T. Sanders, "Spectroscopic sensing via dual-clad optical fiber", *IEEE Sensors Journal*, vol. 6, no. 5, pp. 1227–1231, 2006.

[8] K. O. Hill, Y. Fujii, D. C. Johnson, and B. S. Kawasaki, "Photosensitivity in optical fibre waveguides: application to reflection filter fabrication", *Appl. Phys. Lett.*, vol. 32, no. 10, pp. 647–649, 1978.

[9] B. S. Kawasaki, K. O. Hill, D. C. Johnson, and Y. Fujii, "Narrow-band Bragg reflectors in optical fibres", *Opt. Lett.*, vol. 3, no. 2, pp. 66–68, 1978.

[10] D. K. W. Lam and B. K. Garside, "Characterization of single-mode optical fibre filters", *Appl. Opt.*, vol. 20, no. 3, pp. 440–445, 1981.

[11] M. Parent, J. Bures, S. Lacroix, and J. Lapierre, "Propriétés de polarisation des réflecteurs de Bragg induits par photosensibilité dans les fibres optiques monomodes", *Appl. Opt.*, vol. 24, no. 3, pp. 354–357, 1985.

[12] G. Meltz, W. W. Morey, and W. H. Glenn, "Formation of Bragg gratings in optical fibres by transverse holographic method", *Opt. Lett.*, vol. 14, no. 15, pp. 823–825, 1989.

[13] A. Othonos and Kyriacos Kalli, "Fibre Bragg Gratings – Fundamentals and Applications in Telecommunications and Sensing", Bostnon: Artech House, 1999.

[14] C. Palmer, *Diffraction Grating Handbook.* Richardson Grating Laboratory, Rochester, New York, 2002.

[15] E. G. Loewen and E. Popov, *Diffraction Gratings and Applications.* Marcel Dekker, New York, 1997.

[16] S. T. Peng, H. L. Bertoni, and T. Tamir, "Analysis of periodic thin-film structures with rectangular profiles", *Opt. Commun.*, vol. 10, pp. 91–94, 1974.

[17] K. Knop, "Rigorous diffraction theory for transmission phase scattering by blazed dielectric gratings", *J. Opt. Soc. Am.*, vol. 68, pp. 1206–1210, 1978.

[18] T. Tamir, and S. T. Peng, "Analysis and design of grating couplers", *Appl. Phys.*, vol. 14, pp. 235–254, 1977.

[19] A. R. Neureuther and K. Zaki, "Numerical methods for the analysis of scattering from nonplanar and periodic structures", *Alta Freq.*, vol. 38, pp. 282–285, 1969.

[20] K. C. Chang, V. Shah, and T. Tamir, "Scattering and guiding of waves by dielectric gratings with arbitrary profiles", *J. Opt. Soc. Am.*, vol. 71, pp. 811–818, 1981.

[21] E. Hecht, *Óptica*. Lisboa: Fundação Calouste Gulbenkian, 1991.

[22] F. M. Araújo, *Redes de Bragg em Fibra Óptica*, Ph. D. dissertation, University of Porto, Porto, 1999.

[23] B. Malo, S. Thériault, D. C. Johnson, F. Bilodeau, J. Albert, and K. O. Hill, "Apodised in-fibre Bragg grating reflectors photoimprinted using a phase mask", *Electron. Lett.*, vol. 31, no. 3, pp. 223–225, **1995**.

[24] J. Albert, K. O. Hill, B. Malo, S. Thériault, F. Bilodeau, D. C. Johnson, and L. E. Erickson, "Apodisation of the spectral response of fibre Bragg gratings using a phase mask with variable diffraction efficiency", *Electron. Lett.*, vol. 31, no. 3, pp. 222–223, 1995.

[25] M. J. Cole, W. H. Loh, R. I. Laming, M. N. Zervas, and S. Barcelos, "Technique for enhanced flexibility in producing fibre gratings with uniform phase mask", *Electron. Lett.*, vol. 31, no. 17, pp. 1488–1490, 1995.

[26] W. H. Loh, M. J. Cole, M. N. Zervas, S. Barcelos, and R. I. Laming, "Complex grating structures with uniform phase masks based on the moving fibre-scanning beam technique", *Opt. Lett.*, vol. 20, no. 20, pp. 2051–2053, 1995.

[27] M. Born and E. Wolf, *Principles of Optics*, New York: Pergamon, 1987.

[28] A. Yariv, "Coupled-mode theory for guided-wave optics", *IEEE J. Quantum Electron.*, vol. 9, no. 9, pp. 919–933, 1973.

[29] H. Kogelnik, "Theory of optical waveguides", in *Guided-Wave Optoelectronics*, T. Tamir, Ed. New York: Springer-Verlag, 1990.

[30] G. P. Agrawal, *Nonlinear Fibre Optic*, 2nd ed. San Diego: Academic Press, 1995.

[31] D. Marcuse, *Theory of Dielectric Optical Waveguides*. New York: Academic, 1991.

[32] P. St J. Russel, J. L. Archambault, and L. Reekie, "Fibre Gratings", *Phys World,* vol. 6, no. 10, pp. 41–46, 1993.

[33] K. Raman, *Fiber Bragg Gratings*. Optics and Photonics Series. London: Academic, 1999.

[34] H.-P. Nolting and R. Marz, "Results of benchmark tests for different numerical BPM algorithms", *J. Lightwave Technol.*, vol. 13, no. 2, pp. 216–224, 1995.

[35] W. P. Wang, and C. L. Xu, "Simulation of three-dimensional optical waveguides by a full-vector beam propagation method", *IEEE J. Quantum Electron.*, vol. 29, no. 10, pp. 2639–2649, 1993.

[36] Hongling Rao, Rob Scarmozzino, and Richard M. Osgood, Jr., "A bidirectional beam propagation method for multiple dielectric interfaces", *IEEE Photonics Technol. Lett.*, vol. 11, no. 7, pp. 830–832, 1999.

[37] A. Sudbo, "Numerically stable formulation of the transverse resonance method for vector mode-field calculations in dielectric waveguides", *IEEE Photonics Technol. Lett.*, vol. 5, no. 3, pp. 342–344, 1993.

[38] A. Melloni, M. Floridi, F. Morichetti, and M. Martinelli, "Equivalent circuit of Bragg gratings and its application to Fabry-Pérot cavities", *J. Opt. Soc. Am. A*, vol. 20, no. 2, pp. 273–281, 2003.

[39] M. Yamada and K. Sakuda, "Analysis of almost-periodic distributed feedback slab waveguides via a fundamental matrix approach", *Appl. Opt.*, vol. 26, no. 16, pp. 3474–3478, 1987.

[40] H. Haus, "Mirrors and interferometers" in *Waves and Fields in Optoelectronics*, New Jersey: Englewood Cliffs, 1984.

[41] H. Kogelnik, "Filter response of nonuniform almost-periodic structures", *Bell Sys. Tech. J.*, vol. 55, pp. 109–126, 1976.

[42] R. C. Alferness, C. H. Joyner, M. D. Divino, M. J. R. Martyak, and L. L. Buhl, "Narrowband grating resonator filters in InGaAsP/InP waveguides", *Appl. Phys. Lett.*, vol. 49, no. 3, pp. 125–127, 1986.

[43] K. Utaka, S. Akiba, K. Skai, and Y. Matsushima, "λ/4-Shifted InGaAsP/InP DFB Lasers," *IEEE J. Quantum Electron.*, vol. 22, no. 7, pp. 1042–1051, 1986.

[44] G. P. Agrawal and S. Radic, "Phase-shifted fibre Bragg gratings and their application for wavelength demultiplexing", *IEEE Photon. Technol. Lett.*, vol. 6, no. 8, pp. 995–997, 1994.

[45] J. Canning and M. G. Sceats, "π-phase-shifted fibre periodic distributed structures in optical fibres by UV post-processing," *Electron. Lett.*, vol. 30, no. 16, pp. 1344–1345, 1994.

[46] M. Janos and J. Canning, "Permanent and transient resonances thermally induced in optical fibre Bragg gratings", *Electron. Lett.*, vol. 31 no. 1, pp. 1007–1009, 1995.

[47] D. Uttamchandani and A. Othonos, "Phase shifted Bragg gratings formed in optical fibres by post-fabrication thermal processing", *Opt. Commun.*, vol. 127, no. 4, pp. 200–204, 1996.

[48] S. Li, K. T. Chan, J. Meng, and W. Zhou, "Adjustable multi-channel fibre bandpass filters based on uniform fibre Bragg gratings", *Electron. Lett.*, vol. 34, no. 15, pp. 1517–1519, 1998.

[49] R. Kashyap, P. F. Mckee, and D. Armes, "UV written reflection grating structures in photosensitive optical fibres using phase-shifted phase masks", *Electron. Lett.*, vol. 3, no. 23, pp. 1977–1978, 1994.

[50] L. Poladian, B. Ashton, W. E. Padden, A. Michie, and C. Marra, "Characterization of phase-shifts in gratings fabricated by over-dithering and simple displacement", *Opt. Fibre Technol.*, vol. 9, no. 4, pp. 173–188, 2003.

[51] C. Martinez and P. Ferdinand, "Phase-shifted fibre Bragg gratings photowriting using UV phase plate in modified Lloyd mirror configuration," *Electron. Lett.*, vol. 34, no. 17, pp. 1687–1688, 1998.

[52] J. Canning, H.-J. Deyerl, and M. Kristensen, "Precision phase-shifting applied to fibre Bragg gratings", *Opt.Commun.*, vol. 244, no. 1, pp. 187–191, 2005.

[53] C. Heinisch, S. Lichtenberg, V. Petrov, J. Petter, and T. Tschudi, "Phase-shift keying of an optical Bragg cell filter", *Opt.Commun.*, vol. 253, no. 4, pp. 320–331, 2005.

[54] J. B. Jensen, N. Plougmann, H.-J. Deyerel, P. Varming, J. Hubner, and M. Kristensen, "Polarization control method for ultraviolet writing of advanced Bragg gratings," *Opt. Lett.*, vol. 27, no. 12, pp. 1004–1006, 2002.

[55] F. Bakhti and P. Sansonetti, "Wide bandwidth low loss and highly rejective doubly phase-shifted UV-written fibre bandpass filter", *Electron. Lett.*, vol. 32, no. 6, pp. 581–582, 1996.

[56] F. Bakhti and P. Sansonetti, "Design and realization of multiple quarter-wave phase-shifts UV-written bandpass filters in optical fibres," *J. Lightwave Technol.*, vol. 15, no. 8, pp. 1433–1437, 1997.

[57] C. Martinez and P. Ferdinand "Analysis of phase-shifted fibre Bragg gratings written with phase plates", *Appl. Opt.*, vol. 38, no. 15, pp. 3223–3228, 1999.

[58] F. L. Pedrotti, and L. S. Pedrotti, *Introduction to Optics*. Ohio: Prentice Hall, 1993.

[59] W.R. Skinner, P.B. Hays, V.J.Abreu, "Optimisation of a Triple Étalon Interferometer", Appl. Opt., 26, 2817-2827, 1987.

[60] Marcus Dahlem, *Interrogação Passiva de Cavidades de Fabry-Perot de Baixa Finesse Usando Redes de Bragg em Fibra*, Licenciatura dissertation, University of Porto, Porto, 2000.

[61] R. Kist and W. Sohler, "Fibre-optic spectrum analyzer," *J. Lightwave Technol.*, vol. LT-1, pp. 105–109, 1983.

[62] A. D. Kersey, D. A. Jackson, and M. Corke, "A simple fibre Fabry-Perot sensor," *Opt. Commun.*, vol. 45, no. 2, pp. 71–74, 1983.

[63] S. Kim, J. Lee, D. Lee, and I. Kwon, "A study on the development of transmission-type extrinsic Fabry-Perot interferometric optical fiber sensor," *J. Lightwave Technol.*, vol. 17, no. 10, pp. 1869–1874, 1999.

[64] O. Hadeler, E. Ronnekleiv, M. Ibsen, and R. I. Laming, "Polarimetric distributed feedback fibre laser sensor for simultaneous strain and temperature measurements," *Appl. Opt.*, vol. 38, no. 10, pp. 1953–1958, 1999.

[65] C. E. Lee and H. F. Taylor, "Interferometric optical fiber sensors using internal mirrors," *Electron. Lett.*, vol. 24, no. 4, pp. 193–194, 1988.

[66] J. Sirks, T. A. Berkoff, R. T. Jones, H. Singh, A. D. Kersey, E. J. Friebele, and M. A. Putnam, "In-Line Fiber Etalon (ILFE) Fiber-Optic Strain Sensors," *J. Lightwave Technol.*, vol. 13, no. 7, pp. 1256–1263, 1995.

[67] S. C: KAdu, D. J. Booth, D. D. GArchev, S. F. Collins, "Intrinsic fibre Fabry-Perot sensors based on co-located Bragg gratings," *Opt. Commun.*, vol. 142, no.10 , pp. 189–192, 1997.

[68] S. V. Miridonov, M. G. Shlyagin, D. Tentori, "Twin-grating fiber optic sensor demodulation," *Opt. Commun.*, vol. 191, no. 5, pp. 253–262, 2001.

[69] A. D. Kersey, T. A. Berkoff, and W. W. Morey, "High resolution fiber grating based sensor with interferometric wavelength shift detection," *Electron. Lett.*, vol. 28, no. 3, pp. 236–238, 1992.

[70] M. G. Shlyagin, P. L. Swart, S. V. Miridonov, A. A. Chtcherbakov, I. M. Borbon, and V. V. Spirin, "Static strain measurement with sub-micro-strain resolution and large dynamic range using a twin-Bragg-grating Fabry-Perot sensor," *Opt. Eng.*, vol. 41, no. 8, pp. 1809–1814, 2002.

[71] Y. J. Rao, M. R: Cooper, D. A. Jackson, C. N. Pannell, and L. Reekie, "Absolute strain measurement using an in-fibre-Bragg-grating –based Fabry-Perot sensor," *Electron. Lett.*, vol. 36, no. 8, pp. 708–709, 2000.

[72] K. A. Murphy, M. F. Gunther, A. M. Vengsarkar, and R. O. Claus, "Quadrature phase-shifted extrinsic Fabry–Pérot optical fiber sensors," Opt. Lett., vol. 16, pp. 273–275, 1991.

[73] J. L. Santos and D. A. Jackson, "Passive demodulation of miniature fiber-optic-based interferometric sensors using a time-multiplexing technique," Opt. Lett., vol. 16, pp. 1210–1212, 1991.

[74] O. B. Wright, "Stabilised dual-wavelength fiber interferometer for vibration measurement," Opt. Lett., vol. 16, pp. 56–58, 1991.

[75] A. Ezbiri and R. P. Tatam, "Passive signal processing for a miniature Fabry–Pérot interferometric sensor with a multimode laser diode source," Opt. Lett., vol. 20, pp. 1818–1820, 1995.

[76] Y. Lo and J. S. Sirkis, "Passive signal processing of in-line fiber etalon sensors for high strain-rate loading," J. Lightwave Technol., vol. 15, pp. 1578–1586, 1997.

[77] Y. R. Rao, D. A. Jackson, R. Jones, and C. Shannon, "Development of fiber-optic-based Fizeau pressure sensors with temperature compensation and signal recovery by coherence reading," J. Lightwave Technol., vol. 12, pp. 1685–1695, 1994.

[78] César Jáuregui Misas, Francisco Manuel Moita Araújo, L. A. Ferreira, José L. Santos, and Jose Miguel López-Higuera, "Interrogation of Low-Finesse Fabry–Pérot Cavities Based on Modulation of the Transfer Function of a Wavelength Division Multiplexer," J. Lightwave Technol., vol. 19, no.5, pp. 673–681, 2001.

[79] A. Dandridge, A. Tveten, T. Giallorenzi, "Homodyne demodulation scheme for fiber optic sensors using phase generated carrier," IEEE J. Quantum Electron., vol. 18, no. 10, pp. 1647–1653, 1982.

[80] F. Gonthier, S. Lacroix, X. Daxhelet, R. J. Black, and J. Bures, ""Broadband all-fiber filters for wavelength-division-multiplexing application", Appl. Phys. Lett., vol. 54, no. 14, pp. 1290–1292, 1989.

[81] A. J. C. Tub, F. P. Payne, R. B. Millington, and C. R. Lowe, "Single-mode optical fibre surface plasma wave chemical sensor", Sens. Actuators B, vol. 41, no. 1-3, pp. 71–79, 1997.

[82] G. J. Pendock, H. S. MacKenzie, and F. P. Payne, "Dye lasers using tapered optical fibers", Appl. Opt., vol. 32, no. 27, pp. 5236–5242, 1993.

[83] B. S. Kawasaki. K. O. Hill, and R. G. Lamont, "Biconical-taper single mode fiber coupler", Opt. Lett., vol. 6, no. 7, pp. 327–328, 1981.

[84] T. A. Birks, "Twist-induced tuning in tapered fiber couplers", Appl. Opt., vol. 28, no. 19, pp. 4226–4233, 1989.

[85] C. Caspar and E. J. Bachus, "Fibre-optic micro-ring-resonator with 2 mm diameter", Electron. Lett., vol. 25, pp. 1506–1508, 1989.

[86] L. C. Bobb, P. M. Shankar, and H. D. Krumboltz, "Bending effects in biconically tapered single-mode fibers", J. Lightwave Technol., vol. 8, no. 7, pp. 1084–1090, 1990.

[87] K. P. Jedrzejewski, F. Martinez, J. D. Minelly, C. D. Hussey, and F. P. Payne, "Tapered-beam expander for single-mode optical-fibre gap devices", Electron. Lett., vol. 22, pp. 105–106, 1986.

[88] W. J. Stewart and J. D. Love, "Design limitation on tapers and couplers in single mode fibres", in Proc. ECOC'85, pp. 559-562, 1985.

[89] J. D. Love and W. M. Henry, "Quantifying loss minimisation in single-mode fibre tapers", Electron. Lett., vol. 22, pp. 912–914, 1986.

[90] J. Bures, S. Lacroix, and J. Lapierre, "Analyse d'un coupleur bidirectionnel a fibres optiques monomodes fusionnees", Appl. Opt., vol. 22, no. 12, pp. 1918–1922, 1983.

[91] W. K. Burns, M. Abebe, and C. A. Villarruel, "Parabolic model for shape of fiber taper", Appl. Opt., vol. 24, no. 17, pp. 2753–2755, 1985.

[92] T. A. Birks and Y. W. Li, "The shape of fiber tapers", J. Lightwave Technol., vol. 10, no. 4, pp. 432–438, 1992.

[93] M. A. Putnam, G. M. Williams, and E. J. Friebele, "Fabrication of tapered strain-gradient chirped fibre Bragg gratings", Electron. Lett., vol. 31, no. 4, pp. 309–310, 1995.

[94] L. Dong, J. L. Cruz, L. Reekie, and J. A. Tucknott, "Fabrication of chirped fibre gratings using etched tapers", *Electron. Lett.*, vol. 31, no. 11, pp. 908–909, 1995.

[95] Z. Wei, H. Li, W. Zheng, and Y. Zhang, "Fabrication of tunable nonlinearly chirped fiber gratings using fiber Bragg grating", *Opt. Commun.*, vol. 187, pp. 369–371, 2001.

[96] L. Quetel, L. Rivoallan, M. Morvan, M. Monerie, E. Delevaque, J. Y. Guilloux, and J. F. Bayon, "Chromatic Dispersion Compensation by Apodised Bragg Gratings within Controlled Tapered Fibers", *Opt. Fib. Technol.*, vol. 3, pp. 267–271, 1997.

[97] R. P. Kenny, T. A. Birks, and K. P. Pakley, "Control of optical fibre taper shape", *Electron. Lett.*, vol. 27, no. 18, pp. 1654–1656, 1991.

[98] J. Mora, J. Villatoro, A. Díez, J. L. Cruz, and M. V. Andrés, "Tunable chirp in Bragg gratings written in tapered core fibers",*Opt. Commun.*, vol. 210, pp. 51–55, 2002.

[99] W. Du, X. Tao, and H. Tam, "Temperature independent strain measurement with a fiber grating tapered cavity sensor", *IEEE Photon. Technol. Lett.*, vol. 11, no. 5, pp. 596–598, 1999.

[100] J. D. Love, W. M. Henry, W. J. Stewart, R. J. Black, S. Lacroix, and F. Gonthier, "Tapered single-mode fibres and devices. Part 1: Adiabaticity criteria", *Proc. IEEE*, vol. 138, no. 5, pp. 343–353, 1991.

[101] O. Frazão, M. Melo, P. V. S. Marques, and J. L. Santos, "Chirped Bragg grating fabricated in fused fibre taper for strain-temperature discrimination", *Meas. Sci. Technol.*, vol. 16, pp. 984–988, 2005

[102] F. D. Nunes, C. A. S. Melo, and H. F. S. Filho, "Theoretical study of coaxial fibers", *Appl. Opt.*, vol. 35, no. 3, pp. 388–399, 1996.

[103] M. J. Adams, *An Introduction to Optical Waveguides*. New York: Wiley, 1981.

[104] S. W. James, M. L. Dockney, and R. P. Tatam, "Simultaneous independent temperature and strain measurement using in-fibre Bragg grating sensors," *Electron. Lett.*, vol. 32, no. 12, pp. 1133–1134, 1996.

[105]S. T. Oh, W. T. Han, U. C. Paek, and Y. Chung, "Discrimination of temperature and strain with a single FBG based on the birefringence effect," Opt. Express, vol. 12, no. 4, 724–729, 2004

[106] I. Stenholm and R. J. DeYoung, "Ultra narrowband optical filters for water vapour differential absorption LIDAR (DIAL) atmospheric measurements", NASA, 2001.

[107] R. A. Bond, M. Foster, V. K. Thompson, D. Rees, J. P. do Carmo, "High-resolution optical filtering technology", 22nd Internation Laser Radar Conference (ILRC 2004), Matera, Italy.

[108] E. Udd, Ed., *Fibre Optic Sensors*. New York: Wiley, 1991.

[109] F. Farahi, N. Takahashi, J. D. C. Jones, and D. A. Jackson, "Multiplexed fibre-optic sensors using ring interferometers", *J. Modern Opt.*, vol. 36, no. 3, pp. 337–348, 1989.

[110] B. Moslehi, M. Tur, J. W. Goodman, and H. J. Shaw, "Fibre optic lattice signal processing", *Proc. IEEE*, vol. 72, no. 7, pp. 909–930, 1984.

[111] K. P. Jackson, S. A. Newton, B. Moslehi, M. Tur, C. C. Cutler, J. W. Goodman, and H. J. Shaw, "Optical fibre delay-line signal processing", *IEEE Trans. Microwave Theory Tech.*, vol. 33, no. 3, pp. 193–210, 1985.

[112] E. M. Dowling and D. L. MacFarlane, "Lightwave lattice filters for optically multiplexed communication systems", *J. Lightwave Technol.*, vol. 12, no. 3, pp. 471–486, 1994.

[113] J. Capmany and J. Cascón, "Discrete time fibre-optic signal processors using optical amplifiers", *J. Lightwave Technol.*, vol. 12, no. 1, pp. 106–117, 1994.

[114] C. K. Madsen and J. H. Zhao, *Optical Filter Design and Analysis: A Signal Processing Approach*. New York: Wiley, 1999.

[115] N. Hodgson and H. Weber, *Optical Resonators*. Berlin, Germany: Springer-Verlag, 1997.

[116] D. C. Hutchings, F. A. P. Tooley, and D. A. Russell, "Unidirectional operation of a ring laser using an absorbing Fabry-Perot filter", *Opt. Lett.*, vol. 12, no. 5, pp. 322–324, 1987.

[117] B. Liu, A. Shakouri, and J. E. Bowers, "Passive microring resonator coupled lasers", *Appl. Phys. Lett.*, vol. 79, no. 22, pp. 3561–3563, 2001.

[118] B. Liu, A. Shakouri, and J. E. Bowers, "Wide tunable ring resonator coupled lasers", *IEEE Photon. Technol. Lett.*, vol. 14, no. 5, pp. 600–602, 2002.

[119] S. Tai, K. Kyuma, K. Hamanaka, and T. Nakayama, "Applications of fibre optic ring resonators using laser diodes", *Optica Acta*, vol. 33, no. 12, pp. 1539–1551, 1986.

[120] P. Hariharan, *Optical Interferometry*, 2nd ed. New York: Academic, 2003.

[121] A. Küng, J. Budin, L. Thévenaz, and Ph. A. Robert, "Optical fibre ring resonator characterization by optical time-domain reflectometry", *Opt. Lett.*, vol. 22, no. 2, pp. 90–92, 1997.

[122] J. Capmany and M. A. Muriel, "Double-cavity fibre structures as all optical timing extraction circuits for gigabit networks", *Fibre Integrated Opt.*, vol. 12, pp. 247–255, 1993.

[123] A. Melloni, "Synthesis of a parallel-coupled ring-resonator filter", *Opt. Lett.*, vol. 26, no. 12, pp. 917–919, 2001.

[124] A. Melloni and M. Martinelli, "Synthesis of direct-coupled-resonators bandpass filters for WDM systems", *J. Lightwave Technol.*, vol. 20, no. 2, pp. 296–303, 2002.

[125] S. Kim and B. Lee, "Recirculating fibre delay-line filter with a fibre Bragg grating", *Appl. Opt.*, vol. 37, no. 23, pp. 5469–5471, 1998.

[126] K. Jinguji, "Synthesis of coherent two-port optical delay-line circuit with ring waveguides", *J. Lightwave Technol.*, vol. 14, no. 8, pp. 1882–1898, 1996.

[127] G. Lenz, B. J. Eggleton, C. K. Madsen, and R. E. Slusher, "Optical delay lines based on optical filters", *IEEE J. Quantum Electron.*, vol. 37, no. 4, pp. 525–532, 2001.

[128] J. Haavisto and G. A. Pajer, "Resonance effects in low-loss ring waveguides", *Opt. Lett.*, vol. 5, no. 12, pp. 510–512, 1980.

[129] S. Suzuki, K. Shuto, and Y. Hibino, "Integrated-optic ring resonators with two stacked layers of silica waveguide on Si", *IEEE Photonics Technol. Lett.*, vol. 4, no. 11, pp. 1256–1258, 1992.

[130] B. E. Little, S. T. Chu, H. A. Haus, J. Foresi, and J. P. Laine, "Microring resonator channel dropping filters", *J. Lightwave Technol.*, vol. 15, no. 6, pp. 998–1005, 1997.

[131] B. E. Little, J. S. Foresi, G. Steinmeyer, E. R. Thoen, S. T. Chu, H. A. Haus, E. P. Ippen, L. C. Kimerling, and W. Greene, "Ultra-compact Si-SiO microring resonator optical channel dropping filters", *IEEE Photon. Technol. Lett.*, vol. 10, no. 4, pp. 549–551, 1998.

[132] D. Rafizadeh, J. P. Zhang, S. C. Hagness, A. Taflove, K. A. Stair, and S. T. Ho, "Waveguide-coupled AlGaAs/GaAs microcavity ring and disk resonators with high finesse and 21.6 nm free spectral range", *Opt. Lett.*, vol. 22, no. 16, pp. 1244–1246, 1997.

[133] C. K. Madsen, G. Lenz, A. J. Bruce, M. A. Capuzzo, L. T. Gomez, T. N. Nielsen, and I. Brener, "Multistage dispersion compensator using ring resonators", *Opt. Lett.*, vol. 24, no. 22, pp. 1555–1557, 1999.

[134] C. K. Madsen, G. Lenz, A. J. Bruce, M. A. Capuzzo, L. T. Gomez, and R. E. Scotti, "Integrated all-pass filters for tunable dispersion and dispersion slope compensation", *IEEE Photon. Technol. Lett.*, vol. 11, no. 12, pp. 1623–1625, 1999.

[135] C. K. Madsen and G. Lenz, "Optical all-pass filters for phase response design with applications for dispersion compensation", *IEEE Photon. Technol. Lett.*, vol. 10, no. 7, pp. 994–996, 1998.

[136] G. Lenz and C. K. Madsen, "General optical all-pass filter structures for dispersion control in WDM systems", *J. Lightwave Technol.*, vol. 17, no. 7, pp. 1248–1254, 1999.

[137] J. P. Dakin, Ed., *The Distributed Fibre Optic Sensing Handbook*, Berlin, Germany: Springer-Verlag, 1990.

[138] I.-L. Gheorma and R. M. Osgood Jr., "Fundamental limitations of optical resonator based high-speed EO modulators", *IEEE Photon. Technol. Lett.*, vol. 14, no. 6, pp. 795–797, 2002.

[139] P. P. Absil, J. V. Hryniewicz, B. E. Little, P. S. Cho, R. A. Wilson, L. G. Joneckis, and P. T. Ho, "Wavelength conversion in GaAs micro-ring resonators", *Opt. Lett.*, vol. 25, no. 8, pp. 554–556, 2000.

[140] F. C. Blom, D. R. van Dijk, H. J. W. M. Hoekstra, A. Driessen, and Th. J. A. Popma, "Experimental study of integrated-optics microcavity resonators: Toward an all-optical switching device", *Appl. Phys. Lett.*, vol. 71, no. 6, pp. 747–749, 1997.

[141] J. E. Heebner and R.W. Boyd, "Enhanced all-optical switching by use of a nonlinear fibre ring resonator", *Opt. Lett.*, vol. 24, no. 12, pp. 847–849, 1999.

[142] G. F. Levy, "Analysis of the steady-state and switch-on characteristics of a nonlinear fibre optic ring resonator", *J. Modern Opt.*, vol. 41, no. 9, pp. 1803–1811, 1994.

[143] K. Ogusu, H. Shigekuni, and Y. Yokoya, "Dynamic transmission properties of a nonlinear fibre ring resonator", *Opt. Lett.*, vol. 20, no. 22, pp. 2288–2290, 1995.

[144] K. Ogusu, "Dynamic behavior of reflection optical bistability in a nonlinear fibre ring resonator", *IEEE J. Quantum Electron.*, vol. 32, no. 9, pp. 1537–1543, 1996.

[145] L. F. Stokes, M. Chodorow, and H. J. Shaw, "All-single-mode fibre resonator", *Opt. Lett.*, vol. 7, no. 6, pp. 288–290, 1982.

[146] L. F. Stokes, M. Chodorow, and H. J. Shaw, "Sensitive all-single-mode-fibre resonant ring interferometer", *J. Lightwave Technol.*, vol. 1, no. 1, pp. 110–115, 1983.

[147] Y. Ohtsuka and Y. Imai, "Performance analysis of a terminal-reflected fibre ring-resonant sensor", *Optica Acta*, vol. 33, no. 112, pp. 1529–1537, 1986.

[148] M. N. Zervas and I. P. Giles, "Optical-fibre phase modulator with enhanced modulation efficiency", *Opt. Lett.*, vol. 13, no. 5, pp. 404–406, 1988.

[149] K. Kali and D. A. Jackson, "Ring resonator optical spectrum analyzer with 20-kHz resolution", *Opt. Lett.*, vol. 17, no. 15, pp. 1090-1092, 1992.

[150] M. A. Davis, K. H. Wanser, and A. D. Kersey, "Reflective fibre ring resonator with polarization-independent operation", *Opt. Lett.*, vol. 18, no. 9, pp. 750–752, 1993.

[151] Y. H. Ja and X. Dai, "Optical double-loop fibre resonator with two identical or nonidentical 2x2 fibre couplers", *Opt. Eng.*, vol. 34, no. 11, pp. 3265–3270, 1995.

[152] G. Griffel, "Synthesis of optical filters using ring resonator arrays", *IEEE Photon. Technol. Lett.*, vol. 12, no. 7, pp. 810–812, 2000.

[153] O. Schwelb, "Transmission, group delay, and dispersion in single-ring optical resonators and add/drop filters – A tutorial overview", *J. Lightwave Technol.*, vol. 22, no. 5, pp. 1380–1394, 2004.

[154] L.B. Vann, R. J. DeYoung, S. Mihailov, "Ultra-narrow band fibre optic Bragg grating filters for atmospheric water vapour measurements", 22nd International Lidar Radar Conference (ILRC 2004), Matera, Italy.

[155] Y. Shibata, C. Nagasawa, M. Abo, "Design and analysis of an optical fibre filter for incoherent wind lidar" 22nd Internation Laser Radar Conference (ILRC 2004), Matera, Italy.

[156] "Requirements Definition for Future DIAL Instruments", ESA Reference IMT-CSO/FF/fe/03.887, July 14 (2005).